

X-ray Properties of Narrow-line Seyfert 1 Galaxies

DISSERTATION

der Fakultät für Physik der Ludwig-Maximilians-Universität München
zur Erlangung des Grades
Doktor der Naturwissenschaften
Dr. rer. nat.

vorgelegt von

Luigi C. Gallo
aus Calgary, Kanada

München, den 3. November 2004

1. Gutachter: Prof. Dr. Joachim Trümper
 2. Gutachter: Dr. Hans Böhringer
- Tag der Mündlichen Prüfung: den 9. Dec 2004

Summary

The X-ray properties of five Narrow-line Seyfert 1 galaxies (NLS1) are analysed and presented in this dissertation. The data were collected with *XMM-Newton*, and to date, are of the highest quality ever obtained. Themes which have evolved and appear fundamental in understanding NLS1 are: near- or super-Eddington accretion by a “small” supermassive black hole, partial covering, and reflection. Most of the objects presented in this dissertation can adopt these principles.

The main results of this work are as follow.

- Two observations of 1H 0707–495 and one observation of IRAS 13224–3809 show sharp, spectral drops above ~ 7 keV (Chapters 2 and 4). The sharpness of the features, and absence of iron fluorescent emission and $K\beta$ UTA absorption, challenge the possibility that the drops originate from photonionisation. If partial covering from a neutral absorber is adopted then outflows on the order of $0.05 - 0.15 c$ are required. On the other hand, if the sharp drops are associated with the blue wings of relativistically broadened Fe $K\alpha$ lines (Chapters 2 and 5) then the interpretation requires light bending close to the black hole to explain the large equivalent widths and variability properties. Both interpretations require an iron overabundance ($\sim 3 - 10$ times solar), suggesting that supersolar metallicities may simply be characteristic of NLS1, probably due to strong starburst activity close to the nucleus.
- The general variability properties of NLS1 remain elusive, but advances have been made. All of the Seyferts and quasars discussed here showed rapid and extreme variability at some point during the observations. IRAS 13224–3809 exhibited some of the most remarkable variability (Chapter 3). Lags between the hard and soft energy bands were detected, suggesting that fluctuations at low energies instigated variability at higher energies. However, closer inspection revealed that the lags alternate: sometimes the hard band follows, while at other times it leads. Spectral variability was determined to be correlated with flux variations, but more interestingly was the finding that the spectral variability also lagged flux variations, resulting in flux-induced spectral variability.
- For over ~ 120 ks (spread over two observations), 1H 0707–495 persistently displayed flux variations by at least a factor of four. During the first observation, when 1H 0707–495 was in its lowest flux state ever recorded, there was no significant spectral variability. The second observation, when the source was in a higher flux state, revealed strong spectral variability. Flux and spectral fluctuation were never found to be significantly correlated (Chapter 4).
- The quasar, PHL 1092, exhibited some of the most striking variability considering its high luminosity (Chapter 7). Indeed, an estimate of its radiative efficiency was in excess of that expected from a Schwarzschild black hole. Interestingly, the variability appeared to be entirely concentrated in the soft-excess, with the power-law component appearing quiescent.

- The closest example of *class behaviour* seen in the variability of the group was displayed by the two quasars I Zw 1 and NAB 0205+024 (Chapters 6 and 8, respectively). Both objects exhibited a hard X-ray flare which was concentrated at energies higher than $\sim 2\text{keV}$ and accompanied by spectral variability. A scenario in which the hard X-ray flare originates in the accretion disc corona, and then irradiates the disc itself seem most applicable here.
- I Zw 1 has been defined as the prototype NLS1 based on its optical properties. In the X-rays it appears anything but prototypical. Significant low-energy intrinsic absorption, a weak soft-excess, and evidence for multiple iron emission lines suggest that other processes are at work (Chapter 6).
- PHL 1092 exhibited deviations from a power-law fit in the 2 – 10 keV band (Chapter 7). The difference could be interpreted as an emission line enhanced by light bending close to a Kerr black hole. The complex variability could also be understood in terms of light bending; however, partial covering could not be definitively dismissed due to the modest-quality data.
- NAB 0205+024 portrayed a broad emission feature at $\sim 5.8\text{keV}$ which was inconsistent with expected emission from elements in that spectral region. The feature could be described as neutral iron emitted from a narrow annulus on the disc (Chapter 8). The presence of the hard X-ray flare, steep power-law slope, and redshifted iron line provide circumstantial support for the “thundercloud model” proposed by Merloni & Fabian (2001).

Most of the work discussed in this dissertation has already been published in refereed journals.

Chapter 2: Parts of this chapter are published as: *XMM-Newton spectral properties of the Narrow-Line Seyfert 1 galaxy IRAS 13224-3809*, Boller Th., Tanaka Y., Fabian A., Brandt W. N., Gallo L., Anabuki N., Haba Y., Vaughan S., 2003, MNRAS, 343, 89. The observation was obtained as part of the *XMM-Newton* Guaranteed Time Programme allocated to certain institutes. The authors involved in that initial programme were given preferred listing.

Chapter 3: *The X-ray variability of the Narrow-Line Seyfert 1 galaxy IRAS 13224-3809*, Gallo L. C., Boller Th., Tanaka Y., Fabian A., Brandt W. N., Welsh W. F., Anabuki N., Haba Y., 2004, MNRAS, 347, 269.

Chapter 4: *Long-term spectral changes in the partial-covering candidate NLS1 1H 0707-495*, Gallo L. C., Tanaka Y., Boller Th., Fabian A. C., Vaughan S., Brandt W. N., 2004, MNRAS, 353, 1064.

Chapter 5: Parts of this chapter are published as: *X-ray reflection in the NLS1 1H 0707-495*, Fabian A. C., Miniutti G., Gallo L., Boller Th., Tanaka Y., Vaughan

S., Ross R., 2004, MNRAS, 353, 1071.

Chapter 6: *I Zw 1 observed with XMM-Newton: Low-energy spectral complexity, iron lines, and hard X-ray flares*, Gallo L. C., Boller Th., Brandt W. N., Fabian A. C., Vaughan S., 2004, A&A, 417, 29.

Chapter 7: *An intense soft-excess and evidence for light bending in the luminous narrow-line quasar PHL 1092*, Gallo L. C., Boller Th., Brandt W. N., Fabian A. C., Grupe D., 2004, MNRAS, 352, 744.

Chapter 8: *The narrow-line quasar NAB 0205+024 observed with XMM-Newton*, Gallo L. C., Boller Th., Brandt W. N., Fabian A. C., Vaughan S., 2004, MNRAS, 355, 330.

Zusammenfassung

In dieser Dissertation werden die Röntgeneigenschaften von 5 schmallinigen Seyfert 1 Galaxien (NLS1s) analysiert. Die Beobachtungen wurden mit XMM-Newton durchgeführt und erlauben damit die genauesten Untersuchungen von NLS1s im Röntgenbereich. Das physikalische Verständnis von NLS1s wird grundlegend erweitert im Vergleich zu früheren Beobachtungen. Die physikalischen Prozesse, die für das Verständnis von NLS1s maßgeblich erscheinen, sind: Akkretionsraten am oder teilweise über dem Eddington-Limit, kleine Massen des Schwarzen Loches, teilweise Verdeckung der Akkretionsscheibe durch hochdichte Materie, reflexionsdominierte Röntgenspektren, das Auftreten von extrem relativistischen Effekten in der Nähe des Schwarzen Loches (light bending) sowie magnetische Rekonnexion und Temperaturinhomogenitäten in der Akkretionsscheibe zur Erklärung der Röntgenvariabilität.

Die Ergebnisse dieser Arbeiten können wie folgt zusammengefasst werden:

- Zum ersten mal wurden spektrale Helligkeitsabfälle im Energiebereich über 7 keV nachgewiesen ohne den Nachweis einer schmalen Fe $K\alpha$ Linie. Der Helligkeitsabfall erfolgt in einem Energieintervall von etwa 200 eV, was der Energieauflösung von XMM-Newton entspricht (Kapitel 2 und 4). Die Schärfe des Abfalls, die Abwesenheit der Fe $K\alpha$ Linie sowie der $K\beta$ Multiplettabsorptionslinien, weisen auf photoelektrische Absorption durch hochdichte neutrale Materie in der unmittelbaren Umgebung der Akkretionsscheibe hin. Die gemessenen spektralen Helligkeitsabfälle bei 7.5 und 8.2 keV erfordern Ausflussgeschwindigkeiten von 0.05 und 0.15 Prozent der Lichtgeschwindigkeit. Die spektralen Helligkeitsabfälle können ebenso durch relativistisch verbreiterte Fe $K\alpha$ Linien mit extremen Äquivalentbreiten erklärt werden (Kapitel 2 und 5). In diesem Szenario treten extrem relativistische Effekte (light bending) auf. Sowohl das Absorptionsmodell, wie auch das relativistische Linienmodell erfordern eine Fe Überhäufigkeit, die etwa 3 bis 10-fach über der solaren Eisenhäufigkeit liegt. Dies ist ein starker Hinweis auf hohe Sternentstehungsraten, wie sie in den Frühphasen der Entwicklung von aktiven Galaxien erwartet werden. Bezogen auf Galaxienentwicklung, sind NLS1s aktive Galaxien in der Frühphase ihrer Entwicklung mit kleinen Massen des Schwarzen Loches, hohen Akkretionsraten und starker Sternentstehungsaktivität.
- Die untersuchten NLS1s zeigen extreme und schnelle Röntgenvariabilität im Vergleich mit breitlinigen Seyfert 1 Galaxien. IRAS 13224–3809 weist die interessanteste Variabilität auf. Die Variabilität im weichen (< 2 keV) und harten (> 2 keV) Röntgenbereich ist zeitlich versetzt. Zum ersten mal wurde nachgewiesen, dass die Variabilität im weichen und harten Band alterniert. Dies erlaubt Aussagen über die Natur der zeitlichen Flußänderungen in aktiven Galaxien (Kapitel 3).
- Die schmallinige NLS1 Galaxie 1H 0707–495 wurde zweimal mit XMM-Newton beobachtet. Während der ersten Beobachtung befindet sich das Objekt in einem

Helligkeitsminimum und es wird keine signifikante spektrale Veränderlichkeit gemessen. In der zweiten Beobachtung ist die Leuchtkraft um einen Faktor 10 größer und starke spektrale Veränderlichkeit wird beobachtet. Dieser Zusammenhang zwischen Helligkeit und spektraler Veränderlichkeit kann sowohl durch das Modell der partiellen Absorption, als auch durch das relativistische Linienmodell erklärt werden (Kapitel 4).

- PHL 1092 zeigt bemerkenswerte Röntgenvariabilität gemessen an seiner hohen Leuchtkraft (Kapitel 7). Das radiative Effektivitätslimit überschreitet den Wert für ein nichtrotierendes Schwarzes Loch und impliziert damit den Nachweis eines rotierenden Schwarzen Loches (Kerr black hole). Variabilität wird nur im weichen Energiebereich, aber nicht im harten Energiebereich gemessen, ein Hinweis auf Temperaturinhomogenitäten in der Akkretionsscheibe als dominanter physikalischer Prozess.
- I Zw 1, der sogenannte Prototyp von NLS1s, und NAB 0202+024 zeigen im Gegensatz zu PHL 1092 Strahlungsausbrüche im harten Röntgenbereich verbunden mit spektraler Variabilität. Magnetische Rekonnexion und Bestrahlung der Akkretionsscheibe scheint in diesen Objekten der dominante Prozess zu sein.
- NAB 0205+024 zeigt breite Emissionslinien bei etwa 5.8 keV. Die wahrscheinlichste Erklärung ist eine rotverschobene Fe $K\alpha$ Linie. Das Auftreten von Strahlungsausbrüchen im harten Röntgenbereich, steile Potenzgesetzkontinua und rotverschobene Fe $K\alpha$ Emissionslinien unterstützen das von Merloni und Fabian (2001) vorgeschlagene “thundercloud” Model zur Erklärung der Röntgenvariabilität (Kapitel 8).

Acknowledgments

Many thanks to my advisors, Thomas Boller and Joachim Trümper, for giving me the opportunity to work on such a fascinating topic.

I am very grateful to Günther Hasinger for providing such an amazing environment to conduct scientific research and for allowing me to present my work at numerous meetings over the past three years.

I have had the privilege of working with some great collaborators, people I consider to be among the best in the business. I would like to thank Yasuo Tanaka, Andy Fabian, and Niel Brandt for their patience and enthusiasm over the years. In particular, I am grateful to Yasuo Tanaka for taking on a large role in my growth as a scientist, and for always having time for a chat.

Over the years I certainly took advantage of the expertise at MPE. Many thanks to Frank Haberl, Michael Freyberg, Vadim Burwitz, and Dirk Grupe for imparting their wisdom and advice. Much appreciation to Harald Baumgartner for always answering my cries of *“I need more disk space”* and *“I crashed my computer”*.

Utterly grateful to those who read and commented on parts of this manuscript: Angela Dewar, Charlene Gallo, Dirk Grupe, and Frank Haberl.

Thanks to friends who have made leaving the office, even if only for a coffee, pleasurable: Wolfgang Irber, Anette Hausmann, Elisa Costantini, and Elisa Ferrero.

I can not express how much my family means to me or how much support they have given me. I am especially grateful for my parents, Giuseppe and Lucia, and my sister Angela, who have always been there for me regardless of the distance in between.

It is unbelievable how much Charlene has personally sacrificed to be with me during this *“little phd thing”*. Over these three years I have learned more about her than I have about astronomy. I have witnessed how strong a person she is, how perfect a mother she is, and how much she truly loves me. I consider myself complete with her in my life.

Contents

List of Figures	xiv
List of Tables	xv
1 Introduction	1
1.1 Active Galactic Nuclei: an observational perspective	1
1.1.1 Signs of activity	1
1.1.2 The two basic types of AGN	3
1.1.3 The general picture	4
1.2 The belly of the beast	5
1.2.1 The X-ray spectrum of type-1 AGN	5
1.2.2 Accretion discs	8
1.2.3 Accretion disc coronae	10
1.3 An introduction to Narrow-line Seyfert 1	11
1.3.1 Opening remarks	11
1.3.2 An overview of NLS1	13
1.4 Partial covering	15
1.4.1 Historical evolution	16
1.4.2 A picture of partial covering	16
1.5 Reflection and light bending	19
1.5.1 The reflection spectrum	19
1.5.2 Fe $K\alpha$ emission	20
1.5.3 Light bending considerations	22
1.6 XMM-Newton	25
1.6.1 The observatory	25
1.6.2 EPIC calibration and background	25
1.7 Spectral fitting	29
1.8 Outline of this dissertation	30
2 Spectral properties of IRAS 13224–3809	32
2.1 Introduction	32
2.2 X-ray observations and data analysis	33
2.3 X-ray spectroscopy	33
2.3.1 Mean spectral properties	34
2.3.2 Flux-dependent spectral properties	38

2.4	Discussion	39
3	The X-ray variability of IRAS 13224–3809	41
3.1	Introduction	41
3.2	The UV observation	41
3.3	The X-ray light curves	42
3.3.1	Flux variability	42
3.4	Detection of significant and rapid spectral variability	48
3.4.1	Flux correlated spectral variability	49
3.4.2	A possible lag between flux variations and spectral variations . .	51
3.5	Discussion	52
3.5.1	General findings	52
3.5.2	Reprocessing scenario	53
3.5.3	Future tests for the partial covering and disc-line models	53
4	Long-term spectral changes in 1H 0707–495	55
4.1	Introduction	55
4.2	Observations and data reduction	56
4.3	The AO2 spectral and timing analysis	56
4.3.1	Spectral analysis	56
4.3.2	Timing analysis	59
4.4	Discussion	61
4.4.1	A shifting edge and relativistic outflows	61
4.4.2	The low-energy spectrum	63
4.4.3	Short-term spectral variability	65
4.4.4	Comments on previous X-ray observations of 1H 0707–495 . . .	65
4.5	Conclusions	66
5	X-ray reflection in 1H 0707–495	67
5.1	Introduction	67
5.2	An emission line in the spectrum of 1H 0707–495?	67
5.3	Reflection dominated spectra	68
5.4	Comparison between the GT and AO2 observations	70
5.4.1	Source variability	71
5.5	Discussion	72
6	The prototype narrow-line quasar I Zw 1	74
6.1	Introduction	74
6.2	Observation and data reduction	75
6.3	UV analysis	75
6.4	X-ray spectral analysis	76
6.4.1	Fe K emission	77
6.4.2	The broad-band spectrum	80
6.5	Timing analysis	84
6.5.1	The broad-band light curve	84

6.5.2	The hard X-ray flare and flux-induced spectral variability	86
6.5.3	The nature of the spectral variability	88
6.6	Summary	90
6.6.1	The low-energy spectrum	91
6.6.2	The hard X-ray flare	91
7	PHL 1092 observed with <i>XMM-Newton</i>	92
7.1	Introduction	92
7.2	Observation and data reduction	92
7.3	X-ray spectral analysis	94
7.3.1	The broad-band spectrum	95
7.3.2	Evidence for a reflection component	97
7.3.3	The true soft-excess and the need for high-energy curvature	98
7.4	Variability properties	101
7.4.1	Extreme X-ray variability	101
7.4.2	Simultaneous UV variability	102
7.4.3	Spectral variability	103
7.5	Discussion	105
7.5.1	General findings	105
7.5.2	The ~ 1.4 keV absorption feature	105
7.5.3	The rapid flux variability	106
7.5.4	Light bending model	106
7.5.5	Alternatives to light bending	107
7.6	Conclusions	107
8	NAB 0205+024 observed with <i>XMM-Newton</i>	109
8.1	Introduction	109
8.2	Observations and data reduction	110
8.3	Spectral analysis	111
8.3.1	The broad-band X-ray continuum	111
8.3.2	The RGS data	112
8.3.3	A high-energy feature	114
8.4	Timing Analysis	117
8.4.1	X-ray and optical light curves	117
8.4.2	Spectral variability	118
8.5	Discussion and Conclusions	119
8.5.1	General Findings	119
8.5.2	The nature of the high-energy emission line	120
8.5.3	A comparison to MCG-6-30-15 and I Zw 1	120
8.6	Conclusions	121
9	Open issues, prospects, and concluding remarks	122
9.1	General findings	122
9.2	Partial covering and reflection: open issues	123
9.3	Current investigations	126

9.4 Prospective	127
Bibliography	131

List of Figures

1.1	A type-1 AGN X-ray spectrum	7
1.2	Accretion disc coronae	11
1.3	The optical spectra of Seyfert galaxies	12
1.4	Examples of partial covering	18
1.5	Reflection of an incident power-law spectrum by cold gas	19
1.6	The profile of the Fe $K\alpha$ disc-line	21
1.7	Observed Fe $K\alpha$ emission lines	22
1.8	The light bending scenario	24
1.9	EPIC instrumental features	26
1.10	The EPIC calibration and 3 – 10 keV photon indices	27
1.11	The EPIC pn background spectrum	28
2.1	Residuals from a power-law fit to IRAS 13224–3809	34
2.2	Sharp spectral drop in IRAS 13224–3809	35
2.3	Unfolded partial covering model for IRAS 13224–3809	35
2.4	Fe L absorption in IRAS 13224–3809	37
2.5	Relativistic line interpretation for IRAS 13224–3809	38
2.6	High- and low-flux state spectra of IRAS 13224–3809	39
3.1	Light curves of IRAS 13224–3809	42
3.2	The EPF for IRAS 13224–3809	44
3.3	Light curve cross correlation functions for IRAS 13224–3809	46
3.4	Alternating lag in IRAS 13224–3809	47
3.5	Hardness ratio variability curve for IRAS 13224–3809	48
3.6	Normalised light curves of IRAS 13224–3809	49
3.7	The rms spectrum of IRAS 13224–3809	50
3.8	Hardness ratios correlated with count rates for IRAS 13224–3809	50
3.9	Hardness ratio and light curve cross correlation for IRAS 13224–3809	52
4.1	The AO2 and GT spectra of 1H 0707–495	57
4.2	The AO2 partial covering spectral fit	59
4.3	The GT and AO2 broad-band light curve of 1H 0707–495	61
4.4	The GT and AO2 rms spectrum of 1H 0707–495	61
4.5	The shifting edge in 1H 0707–495	62
4.6	Low-energy spectral complexity in 1H 0707–495	64

5.1	Indication of an emission line in the spectrum of 1H 0707–495	68
5.2	Ionised reflection plus power-law fitted to 1H 0707–495	69
5.3	The blurred ionised reflection model for 1H 0707–495	69
5.4	The unblurred best-fitting reflection model for 1H 0707–495	70
5.5	The AO2 difference spectrum of 1H 0707–495	71
6.1	Power-law fit to the EPIC spectra of I Zw 1	77
6.2	Fe $K\alpha$ emission in I Zw 1	79
6.3	Low-energy residuals in I Zw 1	81
6.4	I Zw 1 broad-band EPIC pn fit residuals	84
6.5	Broad-band light curve of I Zw 1	85
6.6	The rms spectrum of I Zw 1	86
6.7	Normalised hard and soft light curves of I Zw 1	87
6.8	Hardness ratio variability curve of I Zw 1	88
6.9	Ratio spectrum of I Zw 1	89
6.10	Difference spectrum of I Zw 1	90
7.1	Source and background spectra of PHL 1092	94
7.2	High-energy power-law fitted to the broad-band spectrum of PHL 1092	95
7.3	Absorption feature in PHL 1092	96
7.4	Continuum model of PHL 1092	97
7.5	The unfolded model of PHL 1092	100
7.6	Indication of spectral curvature in PHL 1092	101
7.7	GT and AO2 light curves of PHL 1092	102
7.8	Ratio spectrum of PHL 1092	104
8.1	Power-law fit to the EPIC spectra of NAB 0205+024	112
8.2	Continuum model for NAB 0205+024	114
8.3	Redshifted emission line in NAB 0205+024	115
8.4	X-ray and optical light curves of NAB 0205+024	117
8.5	The rms spectra of NAB 0205+024	118
8.6	Normalised light curves and hardness ratio of NAB 0205+024	119
9.1	<i>XEUS</i> simulations of the AO2 observation of 1H 0707–495	129
9.2	<i>XMM-Newton</i> simulations of 1H 0707–495 in various flux states	130

List of Tables

3.1	Flux states in IRAS 13224–3809	51
4.1	Spectral fitting to 1H 0707–495	60
6.1	Spectral fitting to I Zw 1	83
7.1	Source and background counts for PHL 1092	93
7.2	Broad-band spectral fits to PHL 1092	99
7.3	Long-term UV variability in PHL 1092	103
8.1	X-ray continuum models of NAB 0205+024	113
8.2	Spectral fitting to NAB 0205+024	116

Chapter 1

Introduction

The central region of many galaxies harbor an enigmatic phenomenon known as an active galactic nucleus. Capable of out-shining the entire host galaxy by many orders of magnitude, some active galactic nuclei (AGN) generate luminosities as high as 10^{47} erg s⁻¹ from within a volume of space comparable in size to our solar system. This copious energy production is manifested in all frequency bands from radio to γ -rays, and cannot be attributed to the integrated thermal emission from stars. The favoured explanation is that the energy is produced by the transformation of matter into radiation via accretion by a supermassive ($M = 10^6 - 10^9 M_{\odot}$) black hole (Rees 1984). If this assertion is correct, then to appreciate AGN we need to engage some of the most exotic physics known: strong-field relativistic gravity, accretion dynamics, and plasma physics.

The emphasis of the research presented in this dissertation is on the physical processes in the inner-most regions of *Narrow-line Seyfert 1* galaxies (NLS1). NLS1 form a special branch of the AGN phenomenon. They are believed to be young AGN and possibly accreting matter close to or in excess of the upper-most limit determined by their mass. In this introduction I will briefly describe the physics and astronomy background which appears most relevant to the work presented in this dissertation. This description is not intended to be comprehensive. Broader reviews of the topics discussed here can be found in, for example, Rees (1984; black holes in AGN), Peterson (1997; an observational perspective of AGN), Krolik (1999; theoretical consideration of AGN), Frank, King & Raine (1992) and Kato, Fukue & Mineshige (1998; accretion processes in astrophysics), Rybicki & Lightman (1979; radiative processes in astrophysics), Fabian et al. 2000 and Reynolds & Nowak (2003; reflection and fluorescent iron lines), and the conference proceeding edited by Boller et al. (2000; NLS1).

1.1 Active Galactic Nuclei: an observational perspective

1.1.1 Signs of activity

Evidence that supermassive black holes reside at the centres of AGN is well-established from studies of gas and dust kinematics (e.g. Harms et al. 1994; Ferrarese, Ford & Jaffe

1996; Macchetto et al. 1997), water masers (e.g. Watson & Wallin 1994; Miyoshi et al. 1995), reverberation mapping (e.g. Peterson et al. 1998; 2004), and X-ray emission line diagnostics (e.g. Fabian et al. 1989). Moreover, studies of stellar kinematics (e.g. Kormendy & Richstone 1995; Magorrian et al. 1998; Ferrarese & Merritt 2000), favour the presence of a supermassive black hole in most normal, non-active galaxies, as well. The most incontrovertible argument supporting the manifestation of supermassive black holes in nature comes from the centre of our very own Milky Way (e.g. Genzel et al. 1997; Ghez et al. 1998).

While there is strong evidence supporting the existence of supermassive black holes at the centres of all galaxies it remains uncertain as to why some galaxies are *active* and others are not. At this point I will review some of the classical indicators of nuclear activity in galaxies. In general, AGN will exhibit at least one, but probably a combination of these traits.

Non-thermal continuum emission

Whereas the spectral energy distribution (SED) of normal galaxies is dominated by the thermal emission of stars, the very broad SED of AGN can be crudely approximated as a power-law of the form $F_\nu \propto \nu^{-\alpha}$, where F_ν is the flux per frequency interval (ν), and α is the power-law index (spectral index). Different values of the spectral index are measured in various spectral regions, but in general α lies between 0 and 1. An approximately equal amount of energy per decade of frequency is emitted from the far-infrared to the X-ray regimes.

Broad and high-ionisation emission lines

Literally hundreds of emission lines are emitted in the optical and ultraviolet (UV) spectra of some AGN. Thousands, if we include the individual components that make up the Fe II multiplets. The production of strong high-ionisation lines such as O VI, C IV, and Ly α requires ionising potentials far greater than are available in the stellar environments of normal galaxies. Considering this fact, Baldwin, Phillips & Terlevich (1981) and Veilleux & Osterbrock (1987) developed diagnostic diagrams based on the flux ratios of certain high-ionisation lines to lower ionisation lines. Specifically, they considered the ratios [O III] λ 5007/H β , [N II] λ 6583/H α , and [S II] λ 6716, 6731/H α . AGN and normal galaxies occupy distinctly different regions on the diagnostic diagrams, with AGN normally possessing higher values.

Some high-ionisation emission lines can be produced in star-forming regions; however, they tend to be quite narrow, whereas AGN emission lines are broad. If the line widths are attributed to virial motions of matter around a massive object, then the full-width at half-maximum (*FWHM*) of the AGN lines suggest velocities of 500 – 15000 km s⁻¹.

Continuum and/or emission line variability

In almost all energy bands, AGN show variability in the continuum and line fluxes on time scales ranging from a few hundred seconds (the smallest scales which can be probed with significance) to years. Line profile asymmetries, in which the narrow and broad component of a line are offset with respect to each other, are also observed and determined to be time variable.

Variability studies are of great importance as they reveal information about the geometry of the emitting region (from intensity variations), and dynamics of the emitting regions (from profile variations). In the X-ray regime, variability time scales are of a few hundred seconds. Assuming isotropic emission, the X-ray time scales imply that the emitting region is approximately the size of the Earth's orbit around the Sun.

Jets and outflows

A small fraction ($\lesssim 10\%$) of AGN are considered radio-loud ($R > 10$), where *loudness* (R) is defined by the flux ratio at 4.85 GHz and 4400 Å (Kellermann et al. 1989). Some radio-loud AGN exhibit highly columnized jet-like structures and giant lobes which extend on kiloparsec (kpc) scales from the centre of the host galaxy. These structures are presumably due to nuclear material expelled from the supermassive black hole vicinity at significant fractions of the speed of light. On smaller size scales, jets have also been observed in the optical and X-ray bands.

Increasingly common are observations of UV/optical emission lines with blueshifted broad absorption troughs (similar to P Cygni profiles associated with expanding shells in some stellar spectra) in radio-quiet AGN (e.g. Weymann et al. 1991). These broad absorption lines are thought to originate in bulk outflows, not columnized jets, and possibly from an accretion disc wind (e.g. Murray & Chiang 1997).

1.1.2 The two basic types of AGN

In essence, AGN can be separated into two broad categories: Unabsorbed AGN (type-1) and absorbed AGN (type-2). Type-1 AGN normally refer to quasars and Seyfert 1 galaxies. The distinction between quasar and Seyfert 1 is based on optical magnitude (Schmidt and Green 1983), where quasars are the more luminous of the two. However, studies of type-1 AGN show that they all have common properties which form a continuous sequence from low- to high-luminosity making the separation between the two classes rather arbitrary. Until recently, the type-2 AGN class comprised only of Seyfert 2 galaxies; however quasar analogues (absorbed AGN with high intrinsic luminosities) have now been detected with confidence (e.g. Norman et al. 2002; Szokoly et al. 2004).

The first formal distinction between type-1 and type-2 objects was provided by Khachikian & Weedman (1974), and was based on the optical spectral properties of Seyfert galaxies. Both types of galaxies possess narrow ($FWHM \approx 500-1000 \text{ km s}^{-1}$) emission lines arising from permitted transitions (e.g. the Balmer series) and forbidden transitions [i.e. from low density ($10^3 - 10^6 \text{ cm}^{-3}$) material]. However, in Seyfert 1s

the permitted lines have an additional broad ($FWHM > 1000 \text{ km s}^{-1}$) component superposed on the narrow cores. Considering only virial arguments, the broad permitted lines are formed in a ‘broad-line region’ (BLR) which is physically closer to the black hole ($\sim 0.1 \text{ pc}$) than the narrow lines which originate in the ‘narrow-line region’ (NLR; $\sim 100 \text{ pc}$).

The milestone in unifying type-1 and type-2 objects was achieved when broad-emission lines were detected in the polarised spectrum of the Seyfert 2 galaxy NGC 1068 (Antonucci & Miller 1985). The interpretation was that the region emitting the broad-emission lines was obscured, and could only be seen in scattered light. This and subsequent observations led to a *unified model* for radio-quiet AGN (Antonucci 1993), in which type-1 and type-2 objects are intrinsically the same phenomenon observed through varying degrees of line-of-sight absorption.

1.1.3 The general picture

Accretion of material by a supermassive black hole is the most likely model for the central engine of AGN. Other models have been suggested, but they either fail to account for various AGN characteristics or are physically unrealistic. The extreme luminosities found in AGN require an efficient method of energy production. Nuclear fusion, for example, is not sufficient, as the low efficiency of the process ($\approx 0.1\%$) would require preposterous amounts of mass. However, the efficiency of converting gravitational potential energy into radiation via accretion can be as high as 30% in the case of a rotating black hole (Thorne 1974). The strongest observational evidence in favour of an accretion disc and supermassive black hole in AGN is the relativistically broadened Fe $K\alpha$ emission line observed in the X-ray spectrum of MCG–6-30-15 (e.g. Tanaka et al. 1995). This feature will be discussed at length in Section 1.5.

The BLR remains unresolved in even the nearest AGN. Reverberation mapping studies show that the distance to the BLR (R_{BLR}) in Seyfert galaxies is on-average 20 – 30 light-days from the ionising source (e.g. Netzer 1990; Peterson et al. 1998; Kollatschny 2003). However, the size of the BLR scales with luminosity, and R_{BLR} may be up to ten times larger in quasars. Specifically, Kaspi et al. (2000) found that $R_{BLR} \propto L^{0.7}$, where L is the rest frame 5100 Å luminosity. The detection of Fe II from the BLR indicates temperatures $< 4 \times 10^4 \text{ K}$, and densities $> 10^6 \text{ cm}^{-3}$ (Wampler & Oke 1967). The absence of forbidden lines originating from this region, in particular the absence of [O III] $\lambda 4363$, places an even higher density limit of $> 10^8 \text{ cm}^{-3}$. Moreover, Ferland et al. (1992) argue that the strong emission lines of Ly α and C IV are probably produced in environments with even higher densities of $\approx 10^{11} \text{ cm}^{-3}$. The temperatures and velocities in the BLR suggest some kind of organised flow (e.g. a system of discrete clouds), but the actual kinematics of the region (e.g. inflow, outflow, or virial) remain unknown as emission line profiles only weakly constrain the various possibilities (Peterson & Horne 2004).

In some nearby Seyferts the NLR can be resolved (e.g. Macchetto et al. 1994), making it possible to directly map out the physical and kinematic distribution of the region. Emission from the NLR appears extended and isotropic, resulting in negligible

orientation-dependent effects on the narrow-lines. In contrast, the BLR is probably not isotropic (e.g. Ferland et al. 1992), resulting in a range of line widths depending on the line-of-sight orientation. The presence of high-ionisation lines, such as [O III] $\lambda\lambda$ 4959, 5007, and in some cases even the iron ‘coronal’ lines (e.g. [Fe VII] λ 6087 and [Fe X] λ 6375), emphasises the need for a strong, ionising continuum as found in AGN. The distance to the NLR from the central source (R_{NLR}) is on the scale of kiloparsecs. Bennert et al. (2002) argue that R_{NLR} scales with the luminosity of [O III] λ 5007 (or H β) as $R_{NLR} \propto L^{0.5}$. Dopita et al. (2002) and Groves et al. (2004) provide some theoretical foundation for this dependency. A study of 29 quasars by Netzer et al. (2004) suggests the relation must break-down for some high-luminosity, high-redshift objects. They conclude that the NLR in high-luminosity objects must be physically different than the typical NLR seen in nearby objects, and perhaps altered by recent episodes of violent star-formation.

The fundamental component in most AGN unifying schemes is the dense, absorbing torus which covers a significant fraction of the sky seen from the central black hole. Optical/near-infrared reverberation studies place the inner radius of the torus well outside the BLR (e.g. Oknyanskij et al. 1999, 2004; Minezaki et al. 2004). Type-1 and type-2 AGN are then determined by the observers line-of-sight along the torus axis. Type-1 AGN are viewed along the torus axis (unobscured), whereas the view of type-2 objects is compromised by the optically thick medium. Type-2 AGN outnumber type-1s by a factor of 4–9, which places some constraint on the solid angle subtended by the torus. Support in favour of the obscuring torus scenario, and evidence that the unified model may be correct (at least to first order), is the large intrinsic column densities and strong (narrow) iron K lines seen in the X-ray spectra of most Seyfert 2s (e.g. Krolik & Kallman 1987; Awaki & Koyama 1993).

1.2 The belly of the beast

The production of X-rays requires very high temperatures or extreme environments. In addition, the rapid variability seen in the X-ray light curves of many AGN suggests that the emitting region is highly compact, and only light-minutes in size. Therefore, X-rays are most certainly emitted from the inner-most region of AGN, the *belly of the beast*.

1.2.1 The X-ray spectrum of type-1 AGN

The average neutral column density (N_H) above the Galactic plane is only a few times 10^{20} cm^{-2} . However, even this modest amount is sufficient to absorb low-energy X-rays ($E \lesssim 0.5 \text{ keV}$). Thus, the X-ray spectrum of every extragalactic source is absorbed by an amount of at least:

$$a(E) = e^{N_H \sigma_E}$$

where σ_E is the photoelectric absorption cross-section. Some type-1 AGN show additional absorption which can be intrinsic to the AGN and/or host galaxy. The intrinsic

absorption can be variable on various time scales (e.g. Abrassart & Czerny 2000).

To first order the intrinsic AGN spectrum ($M(E)$) can be described by a power-law,

$$M(E) = FE^{-\Gamma}$$

with a flux density of F (normally taken at 1 keV), and photon index¹ Γ . For broad-line Seyfert 1 galaxies the 2 – 10 keV photon index is between 1.7 – 1.8 with very little scatter (e.g. Mushotzky et al. 1980; Mushotzky 1984; Turner & Pounds 1989).

High-quality data, in addition to observations above 10 keV, demonstrate that the Seyfert 1 spectrum deviates from a strict power-law form. Firstly, most objects show a 6.4 keV emission feature (e.g. Pounds et al. 1990). The energy is consistent with neutral iron $K\alpha$ emission which arises from illuminating optically thick material with a power-law continuum. However, the strengths of the observed lines are not correlated with the line-of-sight absorption. Moreover, Inoue (1990) argues that the column densities of the line-of-sight intrinsic absorbers are not sufficient to produce such strong Fe $K\alpha$ emission lines ($EW \approx 50 - 300$ eV); thus suggesting that the absorber is not directly visible. *ASCA* observations evince that in some cases the Fe $K\alpha$ line profiles are consistent with emission from matter moving at relativistic velocities in a disc-like configuration (e.g. Tanaka et al. 1995). Secondly, spectral hardening is observed above ~ 8 keV (Pounds et al. 1990). The hardening can also be understood in terms of emission from optically thick material covering a large solid angle as seen from the primary X-ray sources. Again, the dense material could be illuminated by a power-law continuum, with $\Gamma \approx 2$. In this scenario, Compton scattered X-rays emerge producing what is called the reflection spectrum. The absence of significant absorption from metals above 7.1 keV results in the increased intensity of the reflection spectrum. The intensity of this Compton reflection peaks at ~ 30 keV, at which point Compton down-scattering and the reduction in the electron scattering cross-section lead to diminishing of the reflected flux, and the re-emergence of the power-law continuum (Lightman & White 1988). When taking the reflection components into consideration the intrinsic power-law photon index appears closer to $\Gamma \approx 2$. The constraint on the location of the absorber (i.e. out of the line-of-sight), and the Fe $K\alpha$ line profiles suggest that the reflector is the accretion disc.

At some point the power-law must have a cutoff. For the few Seyfert that were detected with the Compton Gamma Ray Observatory, Zdziarski et al. (1995) found that the power-law had a high-energy cutoff below 500 keV. *BeppoSAX* observations of Seyfert 1s over 0.1 – 300 keV confirmed that the power-law does indeed have an exponential cutoff (Perola et al. 2002). The exact energy varies from source-to-source, but typical values are in the range between $70 \lesssim E_{cut} \lesssim 300$ keV. Therefore, a more general form of the power-law spectrum in Seyfert 1s is:

$$M(E) = FE^{-\Gamma} e^{-E/E_{cut}}.$$

In the early 1980s, *EXOSAT* extended the visible X-ray window down to 0.05 keV, and for the first time it was noted that about half of all Seyferts exhibited excess

¹The photon index (Γ) is more commonly used in X-ray astronomy than the spectral index (α). The two are simply related by $\Gamma = \alpha + 1$.

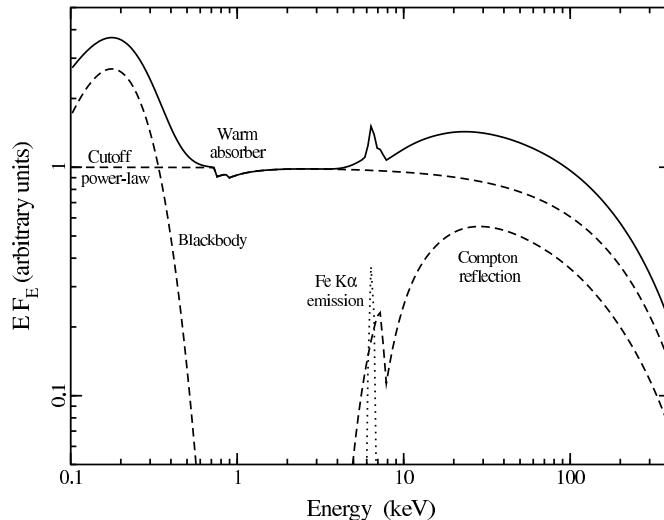


Figure 1.1: A schematic representation of the intrinsic type-1 AGN spectrum between 0.1 – 400 keV. The primary continuum is the power-law component with a photon index of $\Gamma = 2$ and a cutoff energy $E_{cut} = 200$ keV. The soft-excess below ~ 0.7 keV is shown as a blackbody with a temperature of $kT = 45$ eV. Two edges are shown at energies consistent with O VII and O VIII, portraying a warm absorber. The Compton ‘hump’ emerging at $E \gtrsim 8$ keV, and the Fe K α emission line at 6.4 keV, arise naturally from reflection of the power-law continuum off an optically thick medium. The dashed lines represent the individual components, and the solid line is the combined spectrum. The effects of mild intrinsic cold absorption have been neglected.

emission at energies $E \lesssim 1$ keV, the so-called *soft-excess* (e.g. Arnaud et al. 1985). Subsequent *ROSAT* observations by Walter & Fink (1993) suggested that the fraction of AGN with soft-excesses was much higher, perhaps closer to $\sim 90\%$. Although there were significant variations between sources, Piro, Matt & Ricci (1997) demonstrated that the soft-excess could be described as blackbody emission. The typical temperatures were then between 10 – 120 eV. The origin of the soft-excess is still controversial, but there is evidence (e.g. Walter & Fink 1993) that connects it to the ‘big-blue bump’ (Shields 1978) seen in the UV spectra of AGN, which is believed to be thermal emission from the accretion disc (e.g. Grupe et al. 1998).

The three main sources of continuum emission in the X-ray spectrum of AGN are the ‘primary’ power-law, the reflection component, and the soft-excess component. A schematic representation of the X-ray spectrum of an type-1 AGN is shown in Fig. 1.1.

Imprinted on the continuum X-ray spectrum are still more features. The strongest are those associated with an optically thin ionised gas in the line-of-sight. The so-called *warm absorber*, was first proposed by Halpern (1984) to explain the unusual *Einstein* spectrum of MR 2251-178. The term is somewhat inadequate as there is ample evidence that emission originates from this medium as well as absorption (e.g. Netzer 1993; Kaspi et al. 2002; Behar et al. 2003; Pounds et al. 2004). The strongest features

are the absorption edges from O VII and O VIII at 0.739 keV and 0.871 keV, respectively; however, sensitive high-resolution studies with the spectrometers on *Chandra* and *XMM-Newton* have revealed hundreds of absorption and emission lines from various species, including unresolved transition array (UTA) features due to iron absorption (e.g. Kaspi et al. 2002; Behar et al. 2003). Most of the lines appear blue shifted, indicating that the gas is outflowing, most likely as a line-driven wind (e.g. Proga, Stone & Kallman 2000; King & Pounds 2003). The high ionisation state of the gas requires exposure to the extreme radiation achieved in AGN, but the exact location of the ionised gas is still unknown (e.g. Krolik & Kriss 1995).

1.2.2 Accretion discs

Perhaps the most efficient mechanism to produce the enormous luminosities seen in AGN, without requiring unreasonable amounts of mass, is by the transformation of gravitational potential energy into radiation via accretion. When matter enters the gravitational potential well of the black hole it likely does so with some angular momentum. In this case, it is expected that the inflowing gas will form an accretion disc.

If the disc is optically thick and geometrically thin (compared to its radius), then it can be treated under standard (thin) accretion disc theory (Shakura & Sunyaev 1973; see Novikov & Thorne 1973 and Kato et al. 1998 for a relativistic treatment of the standard disc theory). Material in the disc moves inward by losing energy and angular momentum through some form of viscosity. The angular momentum is transported through the disc to larger radii, while the excess energy heats the gas and is radiated. The process is executed with some efficiency, η . A black hole of mass M , accreting matter at a rate \dot{M} , will radiate with a luminosity of:

$$L = \dot{M}\eta c^2. \quad (1.1)$$

As the radiation escapes it will exert an outward force on the accreting gas at larger radii. If the system is to remain in equilibrium then at some distance (r), the outward radiation pressure must be balanced by the gravitational attraction:

$$\frac{GMm_p}{r^2} = \frac{L\sigma_T}{4\pi r^2 c}. \quad (1.2)$$

For simplicity, accretion of a pure hydrogen gas is assumed such that m_p is the proton mass. The Thomson cross-section (σ_T) for electron scattering is also assumed. So it follows from Equation 1.2 that at some critical luminosity (the Eddington luminosity):

$$L_{Edd} = \frac{4\pi cGMm_p}{\sigma_T} = 1.26 \times 10^{38} \frac{M}{M_\odot} \text{ erg s}^{-1}, \quad (1.3)$$

the accretion will cease.²

²In the strictest sense, the Eddington limit only holds true for spherical accretion. However, it can serve as a reasonable first order approximation for disc-like flows.

Ultimately, the efficiency of the process is governed by how close material comes to the black hole before plunging into it. The innermost radius at which a circular orbit is stable (r_{ms}) for an equatorial disc is given by Bardeen (1973) as:

$$r_{ms} = M(3 + Z_2 - [(3 - Z_1)(3 + Z_1 + 2Z_2)]^{\frac{1}{2}}), \quad (1.4)$$

where $Z_1 = 1 + (1 - a^2)^{\frac{1}{3}}[(1 + a)^{\frac{1}{3}} + (1 - a)^{\frac{1}{3}}]$, $Z_2 = (3a^2 + Z_1^2)^{\frac{1}{2}}$, and a is the angular momentum per unit mass. In geometrised units (Misner, Thorne & Wheeler 1973) a is between 0 – 1. Any particle attempting to move in a circular orbit within r_{ms} will fail, and fall inward. Bardeen, Press & Teukolsky (1972) showed that such a gravitational plunge would not produce significant radiation. Rather the maximum accretion efficiency is given by the binding energy at r_{ms} . In the limiting case when $a = 0$ (a non-rotating Schwarzschild black hole), $r_{ms} = 6r_g$ (where the gravitational radius is defined as $r_g = GM/c^2$) and the maximum efficiency is $\eta = 0.057$ (Salpeter 1964: considering general relativistic effects). In principle, a rotating black hole (Kerr black hole) can possess $a = 1$; however Thorne (1974) demonstrated that a rapidly spinning black hole will preferentially capture photons with negative angular momentum, thereby limiting the spin parameter to $a \approx 0.998$. This implies $r_{ms} = 1.23r_g$ and $\eta = 0.30$ (Thorne 1974). Clearly, accretion is a much more efficient mechanism of energy production than, say, nuclear fusion, for which $\eta = 0.007$.

As the angular momentum is transported through the disc to larger radii, the excess energy heats the gas and is radiated. Since the viscous time scale (radial drift time scale: t_v) in a thin disc is much longer than the orbital time scale (dynamical time scale: t_d), the energy is radiated locally making the disc radiative efficient. The emerging flux is then independent of the viscosity mechanism (Frank et al. 1992):

$$F(r) = \sigma_{SB}T^4(r) = \frac{3GM\dot{M}}{8\pi r^3}\left(1 - \left(\frac{r_{ms}}{r}\right)^{\frac{1}{2}}\right), \quad (1.5)$$

where σ_{SB} is the Stefan-Boltzmann constant and $T(r)$ is the effective temperature of the disc.

The temperature of the disc scales weakly with the black hole mass $T(r) \propto M^{-1/4}$. Considering an accretion disc around a supermassive black hole, the characteristic disc temperature is $kT \sim 1 - 10$ eV making them UV sources. Crudely approximating the soft-excess (Section 1.2.1) in AGN as a blackbody renders temperatures by a factor of 10 – 100 times higher than predicted by standard disc theory. However, as the luminosity approaches the Eddington limit (Equation 1.3), the disc no longer can be assumed geometrically thin. At this point, t_v is no longer negligible, and accretion energy may be advected inward before being radiated. The radiative inefficient flow known as the ‘slim-disc’ model was first discussed by Abramowicz et al. (1988). In this case, significant radiation can come from within r_{ms} , and T may exceed the standard thin disc limit. Of particular relevance is the application of slim-discs to NLS1 (Mineshige et al. 2000). Mineshige et al. demonstrated that the spectral and timing properties of all NLS1 observed with *ASCA* could be attributed to slim-discs.

It is conceivable that the soft-excess does not have a thermal origin in the accretion disc. Alternatives, which require further investigation, suggest explaining the

soft-excess as relativistically smeared ionised absorption (Gierlinski & Done 2004), or reflection (e.g. Fabian et al. 2002; Ross & Fabian in preparation; see Section 1.5), or Comptonisation (e.g. Vaughan et al. 2002; see Section 1.2.3).

1.2.3 Accretion disc coronae

The variability time scales indicate that the X-rays are coming from the innermost region surrounding the black hole. A natural candidate for this emission is the accretion disc. However, the X-ray power-law emission extends over the entire X-ray band (i.e. 0.1 – 300 keV). Thermal disc emission is expected to peak in the UV regime, and even under some specific conditions the observable emission is not expected to exceed a few hundred electron volts.

A promising mechanism for producing the observed spectrum is inverse Compton scattering (Comptonisation). In this process the low-energy photons emitted from the disc interact with hot ($T \approx 10^9$ K), relativistic electrons located in the accretion disc “halo” called the *corona*. Two types of energy transfers occur during these interactions. Firstly, the photons lose energy through the recoil of the electrons. Secondly, the photons gain energy by the Doppler shift of the moving electrons. The photons are up-scattered to higher energies when its mean energy ($\langle E \rangle$) is less than the thermal energy of the electrons:

$$\frac{\langle E \rangle}{mc^2} < \frac{4kT}{mc^2}. \quad (1.6)$$

The emerging spectrum depends on the Compton y parameter which is the product of the average energy gained per scatter and the total number of scatterings. If the electron gas is optically thin, then y is on the order of unity, and it can be shown (Shapiro, Lightman & Eardley 1976; Katz 1976) that a power-law spectrum with a slope of

$$\Gamma = -\frac{1}{2} + \sqrt{\frac{9}{4} + \frac{4}{y}} \quad (1.7)$$

emerges. When $y = 1$, $\Gamma = 2$, which is comparable to what is seen in AGN. Of course other assumptions, such as geometry, also come into play. As the energy of the photons become comparable to the electron thermal energy, the photons no longer gain energy, and a sharp cutoff is expected in the spectrum at $E_{cut} = 2kT$. The cutoff energies seen with *BeppoSAX* (Section 1.2.1) are consistent with $T \sim 10^9$ K, giving further credence to this picture.

While it appears that, at least to first order, the coronal picture is correct there are two significant challenges. Firstly, a mechanism to heat the coronal electrons, and then re-heat them when they have donated their energy, is currently unknown. Galeev, Rosner & Vaiana (1979) suggest that the process may be similar to how the hot solar corona above the cool photosphere is heated. That is, magnetic loops from the accretion disc rise into the low-density corona and burst, then through reconnection of the the field line dissipate their energy into hot electrons. There is significant theoretical work that is required to fully solve this problem, but early results do give the idea some validity (e.g. Miller & Stone 2000). In Chapters 6 and 8 we show

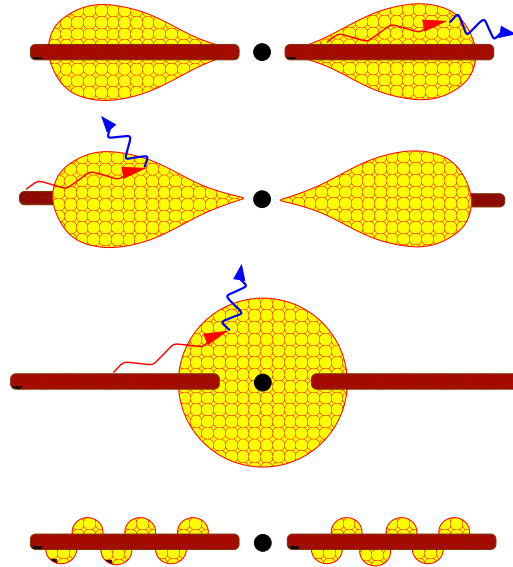


Figure 1.2: Possible geometries for the accretion disc corona. In the top panel is the “slab” or “sandwich” geometry. The two middle panels are “sphere+disc” geometries, and the lower panel is referred to as a “patchy corona”. The slab geometry tends to predict softer emission than is observed, while in the remaining geometries the corona is inefficiently cooled by the disc photons. Figure taken from Reynold & Nowak (2003).

evidence for the existence of hard (2 – 10 keV) X-ray flares, which could be explained in this context. The second outstanding issue is that the specific geometry of the corona is completely unknown. While there is general agreement that the disc and corona are physically disconnected, the exact picture is often contrived to explain specific observations (Fig. 1.2).

1.3 An introduction to Narrow-line Seyfert 1

1.3.1 Opening remarks

In 1978 Davidson and Kinman described the optical spectrum of Mrk 359 as being similar to that of a Seyfert 1, but with unusually narrow permitted lines. They went on to suggest that Mrk 359 warranted further study. During that same year, Koski (1978) and Phillips (1978) noted similar features in another AGN, Mrk 42. Over the years other similar objects were identified and in 1985 Osterbrock & Pogge formally classified them as “Narrow-line Seyfert 1” galaxies (NLS1) according to their optical spectra. The formal, albeit subjective, criteria are as follow:

- NLS1 have narrow permitted lines which are only slightly broader than the forbidden lines. Based on a spectropolarimetric study of 18 NLS1, Goodrich (1989) determined that $FWHM(H\beta) < 2000 \text{ km s}^{-1}$ served as a reasonable discriminator between NLS1 and broad-line Seyfert 1s (BLS1).

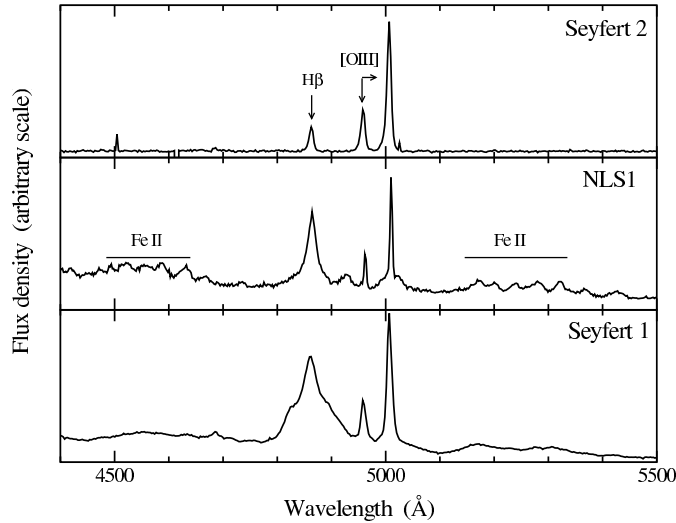


Figure 1.3: Optical spectra of Seyfert galaxies between 4400–5500 Å. The NLS1 is RX J1251.0+6603. The Seyfert 2 and Seyfert 1 are Mrk 1066 and NGC 3516, respectively. Relative to H β , the [O III] emission is clearly stronger in the Seyfert 2. The Fe II multiplets are visible in the spectra of both the NLS1 and the Seyfert 1, but absent in Mrk 1066. Also note the broader H β line in NGC 3516.

- There is often strong emission from Fe II multiplets in the optical spectrum (e.g. multiplets between 4500 – 4680 Å and 5105 – 5395 Å), or from the higher ionisation iron coronal lines.
- The [O III] emission is weak, with the flux ratio [O III]/H β < 3. This value was determined by Shuder & Osterbrock (1981) to effectively distinguish between Seyfert 1s and Seyfert 2s.

NLS1 are type-1 Seyferts; however they possess narrower permitted lines. Their optical spectra cannot be described by the physical models used to explain Seyfert 2 galaxies, and as will be seen throughout this work, their X-ray behaviour is also uncharacteristic of Seyfert 2s. Representative optical spectra from a NLS1, Seyfert 1, and Seyfert 2 are shown in Fig. 1.3. It must be asserted that NLS1 are not distinct from BLS1, rather they are the same type of object and their properties form a continuous sequence with increasing *FWHM* (e.g. Goodrich 1989; Boroson & Green 1992; Puchnarewicz et al. 1992; Boller, Brandt & Fink 1996; Grupe 1996; Brandt, Mathur & Elvis 1997; Wills et al. 1999; Grupe 2004; Gallo et al. 2004). Moreover, NLS1 are not rare. NLS1 comprise 10 – 20% of optically selected Seyfert 1s (e.g. Williams, Mathur & Pogge 2003), and the fraction is much higher in soft X-ray samples (\sim 50%; Puchnarewicz et al. 1992; Grupe 1996; Grupe 2004).

1.3.2 An overview of NLS1

The importance of NLS1 became apparent on the discovery of the ‘primary eigenvector’ (PC1; Eigenvector 1) in Boroson & Green’s (1992) principle component analysis of PG quasars. PC1 showed a strong anticorrelation between the strengths of [O III] and Fe II, with NLS1 as a class showing the strongest Fe II emission and weakest [O III]. While the physical driver of PC1 is still debated, there are strong indications that it is the fraction of the Eddington luminosity (L/L_{Edd}) at which the object is emitting which is responsible, implying that NLS1 are relatively high accretion rate systems. Crenshaw, Kraemer & Gabel (2003) presented a study of the host galaxy morphologies of NLS1 and BLS1, based on broad-band optical images from the *HST*. Large scale stellar bars appeared more frequently in NLS1 than in BLS1; thus providing an efficient mechanism to transport gas to the nuclear region (Friedli & Benz 1993).

There are no significant differences between NLS1 and BLS1 in their 0.2 – 2 keV, 5100 Å, or bolometric luminosities (Grupe et al. 2004). Given the comparable luminosities and indications for high accretion rates, it naturally follows that NLS1 possess a lower mass black hole compared to BLS1 of similar luminosity.

Black hole mass estimates indeed show that NLS1 have lower mass black holes (Wandel, Peterson & Malkan 1999; Peterson et al. 2000; Grupe & Mathur 2004). In addition, Grupe & Mathur (2004) found that the $M - \sigma$ relation, which is the correlation between the black hole mass and stellar velocity dispersions in the bulge of normal galaxies (e.g. Gebhardt et al. 2000a) and AGN (Gebhardt et al. 2000; Ferrarese et al. 2001), is not the same for NLS1 with high L/L_{Edd} (Mathur & Grupe 2004). The interpretation is that the accretion rate is highest at earlier evolutionary epochs and dwindles as the AGN ages; thus emphasising the assertion that NLS1 are young AGN (Grupe 1996; Grupe et al. 1999; Mathur 2000).

The strong Fe II emission in NLS1 is prevalent in the UV (e.g. Laor et al. 1997; Constantin & Shields 2003), optical (e.g. Boroson & Green 1992), and infrared (e.g. Rodríguez-Ardila et al. 2002). The observed widths and absence of forbidden emission suggests that Fe II is formed in the dense BLR. A great deal of effort was exerted to describe this emission in terms of photoionisation, but it soon became clear that photoionisation models could not account for all of the Fe II emission. The ‘Fe II discrepancy’ remains unsolved, though models which consider non-radiative heating (probably due to shocks produced in outflows), with an overabundance of iron (e.g. Joly 1987; Collin & Joly 2000) are promising. The idea of outflows seems relevant for NLS1 (see Chapters 2 and 4). As mentioned, the warm absorber observed at X-ray energies appears blueshifted indicating outflows. Moreover, the $H\beta$ line tends to have a pronounced blue asymmetry in NLS1 (e.g. Boroson & Green 1992; Grupe et al. 1999), which also favours an outflow interpretation. Outflow features in the UV are also present. Leighly & Moore (2004) showed that the high-ionisation lines (including C IV and N V) are blueshifted, whereas the intermediate- and low-ionisation lines are centred at their rest wavelengths. The profiles of the high-ionisation lines are consistent with a wind origin.

Dedicated studies of large samples of NLS1 to determine their class properties at

radio and infrared wavelengths are sparse. *ISO* observations of four NLS1 galaxies (Polletta & Courvoisier 1999) showed that their infrared spectra are consistent with those of BLS1. The presence of dust heated by a bright star forming region is suggested for only one (IRAS 13224-3809) of the four NLS1, and does not appear to be a general property of NLS1. Ulvestad, Antonucci & Goodrich (1995) conducted the first radio study of six NLS1, and determined that they were radio-quiet and not notably different from BLS1. Condon et al. (1998) considered a sample of *ROSAT/IRAS* galaxies for a *VLA* radio study. The sample included 24 NLS1, for which Condon et al. determined that radio emission was compact and unresolved at 1'' resolution. The radio-quiet nature of NLS1 is predicted by the Boroson & Green (1992) principle component analysis. Boroson & Green found that the strength of the Fe II emission was anticorrelated with radio power. NLS1, having strong Fe II emission, are expected to be radio-quiet. However, a few radio-loud NLS1 have emerged over the years: PKS 0558-504 (Remillard et al. 1991), RGB 0044+193 (Siebert et al. 1999), RX J0134-4258 (Grupe et al. 2000), and the radio-loudest NLS1 PKS 2004-447 (Gallo et al. in preparation).

Arguably the most fascinating NLS1 characteristics are manifested in the X-ray regime. Interest in this class of AGN intensified with the commission of *ROSAT* and *ASCA* in the 1990s. A breakthrough came with the *ASCA* observation of RE 1034+39 (Pounds, Done & Osborne 1995). The broad-band X-ray spectrum showed a very strong soft-excess rising above a steep power-law continuum at energies below ~ 2 keV. The spectrum bore a striking resemblance to the X-rays spectrum of Galactic black hole candidates (GBHC) in their most active states. The similarity prompted Pounds et al. to postulate that NLS1 were supermassive black hole analogies of GBHC. Coincidentally the analogy supports the assertion of high accretion rates in NLS1.

The watershed discovery was that of Boller, Brandt & Fink (1996; see also Laor et al. 1997, and Puchnarewicz et al. 1992), revealing an anticorrelation between the soft X-ray photon index measured by *ROSAT* and the optical $H\beta$ line width. NLS1 showed softer (steeper) 0.2 – 2 keV spectra than BLS1. Moreover, Brandt & Boller (1998) determined a highly significant anticorrelation between the *ROSAT* photon index and the Boroson & Green primary eigenvector. The revelation provided a strong link between the intrinsic properties of the continuum emission and the dynamics of the BLR. A smaller black hole mass and higher accretion rate could produce an accretion disc spectrum which is shifted to soft X-ray energies (e.g. Ross, Fabian & Mineshige 1992; see also Equation 1.5). The lower black hole mass would in turn result in smaller Keplerian velocities in the BLR.

The X-ray/BLR relation was extended with the discovery that NLS1 also exhibit steeper 2 – 10 keV spectra (Brandt, Mathur & Elvis 1997). The relation could be recovered via significant Compton cooling of the accretion disc corona due to the strong soft X-ray excess found in most NLS1. The lower energy gain per scattering (smaller Compton y parameter in Equation 1.7) would result in steeper hard X-ray slopes.

The X-ray variability properties of NLS1 are also fascinating (see, for example, Chapter 3 and 7). Boller et al. (1996) showed that NLS1 frequently displayed rapid

(~ 1000 s) variability, which could be interpreted as evidence for a small black hole mass. Extreme events were also frequent. Several large amplitude flares by factors of 60 and 15 on hourly time scales were reported during monitoring campaigns of IRAS 13224-3809 (Boller et al. 1997; see also Otani, Kii & Miya 1996) and PHL 1092 (Brandt et al. 1999), respectively. The variability in PHL 1092 is perhaps even more impressive given that it is a luminous quasar ($L_X \gtrsim 10^{45}$ erg s $^{-1}$). Leighly (1999) determined that as a class, NLS1 exhibit larger amplitude variations than BLS1 of similar luminosities. The simplest explanation is that NLS1 have shorter light-crossing time scales, than BLS1, due to smaller black hole masses. Since they are no fainter than BLS1, it again follows that NLS1 must be accreting at relatively large fractions of their Eddington accretion rates.

The variability processes in NLS1, and AGN in general, are simply not known, but numerous suggestions have been put forth. The very large-amplitude variability on short time scales implies a very high efficiency of converting accretion energy to radiation. Brandt et al. (1999) suggested that beaming may play a role in amplifying flares. Beaming from an edge-on disc system was proposed specifically for IRAS 13224-3809 (Boller et al. 1997), but recent *XMM-Newton* observations challenge this conclusion (Boller 2003). Mineshige et al. (2000) suggest that a consequence of the slim-disc scenario, is that the higher accretion rates will result in stronger magnetic fields. Large amplitude flares may result from reconnection of this more powerful magnetic field. It has also been suggested that occultation by large optically-thick clouds may produce high-amplitude variability seen in NLS1 (Abrassart & Czerny 2000; Brandt & Gallagher 2000; Tanaka et al. 2004; Grupe et al. 2004b; Section 1.4).

Interestingly, the rapid and extreme variability seen in the X-rays is not seen at optical wavelengths (though long-term trends in both bands are correlated). Radio-quiet AGN typically yield low-amplitude variations on time scales of a few days (e.g. Webb & Malkan 2000). Searches for rapid variability in IRAS 13224-3809 (Young et al. 1999; but see Miller et al. 2000), and in a sample of NLS1 (Klimek, Gaskell & Hedrick 2004) were unsuccessful. Giannuzzo & Stirpe (1996) have also suggested that NLS1 vary less than BLS1 do at optical wavelengths, but Klimek et al. argue that the claim cannot be supported given lack of an adequate control sample of BLS1.

The fact that the rapid and large amplitude X-ray variability is not duplicated in the optical band dictates that the mechanism responsible for the variability is not the same throughout the AGN.

1.4 Partial covering

Partial covering is an evolution of ideas based on observations of AGN and X-ray binaries. While some aspects of partial covering have received theoretical consideration (e.g. Celotti et al. 1992; Rees 1987; Abrassart & Czerny 2000), a rigorous, self-consistent, investigation of the problem has not been pursued. Unlike the reflection scenario (discussed in Section 1.5), it is not always possible to predict observations based on partial covering.

1.4.1 Historical evolution

One of the earliest discussions of partial covering resulted from observations of the Seyfert 1 NGC 4151 with *Einstein* and *HEAO-1* (Holt et al. 1980). The data could not be explained by absorption from a uniform column of cold gas. The simplest explanation was that NGC 4151 was viewed through a *patchy-absorber* which obscured $\sim 90\%$ of the X-ray emitting zone. It was determined that in the case of NGC 4151 the absorber would need a column density of about $N_{\text{H}} \approx 10^{22} \text{ cm}^{-2}$ and an overabundance of heavy ($Z \geq 14$) elements.

Tennant (1988) analysed 3-hours of *EXOSAT* data of the X-ray binary Cir X-1 during a bright, soft-flaring state. Tennant listed three arguments in favour of a *lumpy accretion* which provides partial obscuration of the source as small dense lumps move in and out of the line-of-sight. Firstly, the X-ray intensity varied by a factor of > 100 , with only very minor changes in the overall energy spectrum. Secondly, based on the conclusions of Robinson-Saba (1983) that the soft-high state spectrum of Cir X-1 was dominated by the accretion disc, in order to generate the observed variations dramatic changes in the accretion flow would be required. The third line of reasoning was that the typical light curve of Cir X-1 showed long periods of constant intensity, with large-amplitude variations occurring only near the time of the transitions (also see Dower, Bradt & Morgan 1982, Ikegami 1986, Oosterbroek et al. 1995).

The near zero phase *ASCA* observation of Cir X-1 revealed remarkable flux and spectral variability. Brandt et al. (1996) also adopted partial covering to describe the behaviour of this source; however, the geometry they assumed for the absorber was different than that proposed by Tennant (1988). Brandt et al. proposed a picture involving a direct component along with an electron-scattered component. In this case, the X-rays would be completely blocked at low energies, but would penetrate through the absorbing matter above $\sim 3 - 5 \text{ keV}$. They speculated that the absorbing material was the outer bulge of an accretion disc seen edge-on. Changes in the column density of the disc, due to disc rotation, would result in the observed spectral and flux variability of the source which is intrinsically constant. The low-energy photons would be observed by electron scattering, which probably occurs in the accretion disc corona.

1.4.2 A picture of partial covering

One of the primary challenges for partial covering is deriving a standard picture. Indeed, the physical and/or geometrical conditions are often contrived to explain a particular observation. For example in the absorber adopted by Brandt et al. (1996) to describe Cir X-1, the low-energy ($E \lesssim 3 \text{ keV}$) photons are never observed directly. Rather this emission is scattered into our line-of-sight. This is in contrast to the lumpy accretion picture of Tennant (1988). One potential prediction of models with a large amount of electron scattering is that the disc flux may be polarised over the expected interstellar value. The polarisation fraction should change with time as the absorbing column, and hence the direct contribution, varies. This type of partial covering has also been suggested for the highly-polarised NLS1, Mrk 1239 (Grupe, Mathur & Komossa

2004).

The partial covering model utilised in this dissertation follows the prescription of Tanaka et al. (2004), considering a neutral absorber. When a single absorber is responsible for the covering, the fitting model is expressed as:

$$[fe^{-\sigma N_H} + (1 - f)][F_{soft}(E) + F_{hard}(E)], \quad (1.8)$$

where f is the covering fraction of an absorber with a column density N_H , and photoabsorption cross-section σ . $F_{soft}(E)$ and $F_{hard}(E)$ are the model functions of the soft and hard components, respectively. If a straight power-law is adopted the required iron abundance for the absorber become very high (e.g. 50 times solar in the case of the NLS1 1H 0707-495; Boller et al. 2002). This is probably a manifestation of the spectral fitting as the model attempts to accommodate for curvature in the hard X-ray spectrum. The observed covering is certainly the summation of multiple absorbers. In this case, a more physical description for the situation may be double partial covering (an approximation for more complex cases involving multiple absorbing components):

$$[fe^{-\sigma N_H} + (1 - f)][f_2e^{-\sigma N_{H,2}} + (1 - f_2)][F_{soft}(E) + F_{hard}(E)]. \quad (1.9)$$

Here, f_2 and $N_{H,2}$ denote the covering fraction and column density of the second absorber. Adopting double partial covering introduces a natural curvature to the model without requiring abnormally high iron abundances (although 1H 0707-495 still requires ~ 5 times solar overabundance of iron; Tanaka et al. 2004).

In the model described by Equations 1.8 and 1.9 the soft and hard continuum components are equally covered by the absorbers. However, there is no a priori reason to expect that this is a more physical description. It should also be noted that the covering fraction (f) and column density (N_H) are covariant and it is not possible to solve for either uniquely.

The first *XMM-Newton* observation of the NLS1 1H 0707-495 in October 2000 revealed a sharp spectral feature at ~ 7 keV in which the spectrum ‘‘jumped’’ by a factor of > 2 within a few hundred eV (Boller et al. 2002). The measured energy and sharpness of the feature implied K-absorption by neutral iron. The fluorescent yield of iron is 0.34 (the probability that de-excitation will occur via fluorescence rather than autoionisation; Bambynek et al. 1972), so approximately one-third of the photons absorbed above the iron K-edge at 7.1 keV will be accompanied by subsequent K-fluorescence at 6.4 keV. The absence of the 6.4 keV iron line in 1H 0707-495 resulted in a fluorescence/edge ratio much smaller than predicted by the fluorescent yield, implying that the column density along the line-of-sight was higher than average. Coupled with the fact that there was low intrinsic absorption below ~ 1 keV led Boller et al. (2002) to consider a partial covering model.

The discovery of the fluorescent yield discrepancy has become an indicator for partial covering, and also places constraints on the geometry of the absorber. It is clear that the absorber is not necessarily spherically symmetric. Such a discrepancy has been found in a number of NLS1 (e.g. Boller et al. 2003; Pounds et al. 2004; Chapter 2 and 4), as well as in X-ray binaries (e.g. Ueda et al. 1998; Tanaka, Ueda &

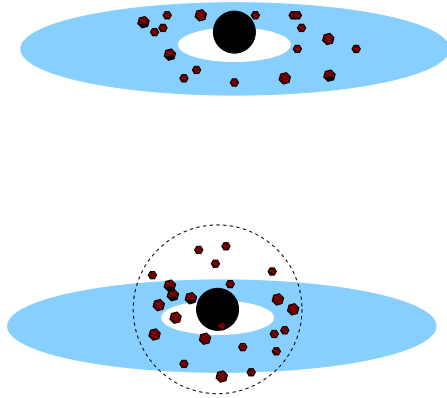


Figure 1.4: Two possible geometries for partial covering. Top panel: The absorbing clouds are distributed throughout the disc as may be expected in a “lumpy accretion” scenario (Tennant 1988). The figure may also be consistent with what is seen in some NLS1. Lower panel: Partial covering which is spherically symmetric and may not necessarily result in a fluorescent yield discrepancy.

Boller 2003). However, the conclusion that the fluorescent yield is not equatable with the 4π covering factor does not rule out partial covering. (see Fig. 1.4).

The low intrinsic absorption seen in NLS1 implies that some of the low-energy emission reaches the observer unobscured. This observation favours a patchy, *cloud-like* absorber (Fig. 1.4). The absence of Fe L-shell absorption (which has a smaller transitional cross-section), further implies that the absorber only partially covers the source.

For the objects discussed in this dissertation, the absorbing clouds block photons with energies $E \lesssim 7-8$ keV; therefore requiring densities of $10^{23}-10^{24}$ cm $^{-2}$. The high density also satisfies the assumption that the absorber can be close to the ionising continuum source and yet remain neutral (Rees 1987). Tanaka et al. (2003) demonstrated that given a certain column density, the covering fraction can reveal the number of clouds in the line-of-sight. Even in extreme cases, Tanaka et al. deduced that only a few (~ 3) clouds are required to satisfy the observed absorption. The distance of the absorber from the ionising component is also a challenge to determine. Tanaka et al. (2004) considered the variability time scales in 1H 0707-495 as an indication of the line-of-sight crossing time for a cloud. Assuming that the source is not intrinsically variable, and that the clouds are in Keplerian orbits, Tanaka et al. determined that the clouds are at a distance of a few hundred gravitational radii. A second distance calculation is given in Chapter 4, which agrees well with the value determined by Tanaka et al. (2004). Such dense clouds are likely confined by magnetic fields (e.g. Rees 1987;

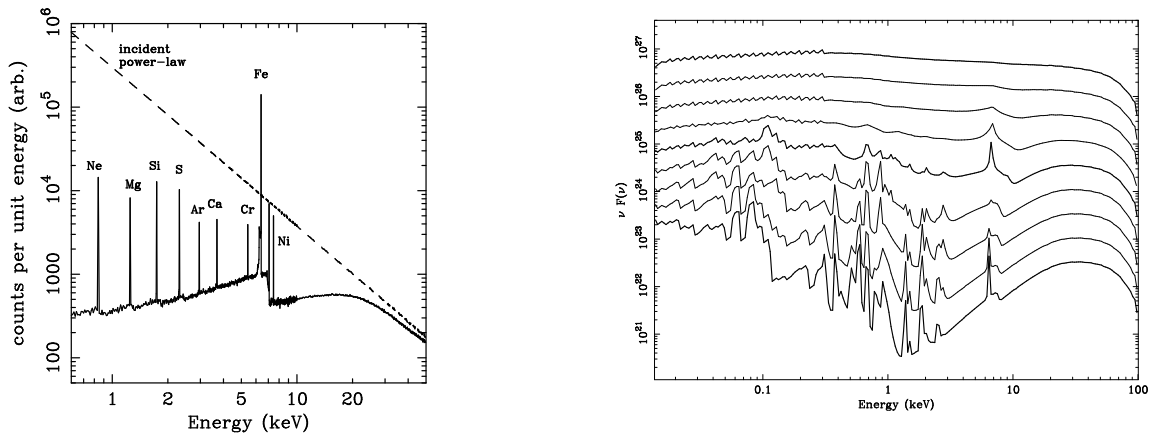


Figure 1.5: Left panel: The expected reflection spectrum produced when an incident power-law (dashed-line) illuminates a cold slab of gas with cosmic abundances. Figure taken from Fabian et al. (2000), and based on simulations from Reynolds (1996). Right panel: The curves represent the reflection spectrum produced from matter with different ionisation parameters (ξ). From bottom to top: $\log \xi = 1.0, 1.5, 2.0, 2.5, 3.0, 3.5, 4.0, 4.5, 5.0$. As ξ increases, the elements become more ionised. When the disc is fully ionised no further atomic features are present. The figure is taken from Reynolds & Nowak (2003) and based on calculations by Ballantyne, Ross & Fabian (2001). The figures do not portray relativistic effects close to the black hole which would broaden and blur the resulting reflection spectrum.

Celotti, Fabian & Rees 1992). Two plausible pictures for the type of partial covering that appears applicable to NLS1 observations are shown in Fig. 1.4.

1.5 Reflection and light bending

1.5.1 The reflection spectrum

It is conceivable that some fraction of the hard X-rays, likely produced in the corona, will illuminate the relatively cold accretion disc, giving rise to the reflection component in the spectrum. When the hard X-ray photons enter the accretion disc there are a number of possible interactions that can occur: Compton scattering by free or bound electrons, and photoelectric absorption followed by either fluorescent line emission or Auger de-excitation. So the photon is either destroyed, scattered, or reprocessed into a fluorescent line photon. Fig. 1.5 illustrates the expected reflection spectrum based on calculations which take all these processes into consideration (Reynolds 1996; based on similar calculations by George & Fabian 1991; Matt, Perola & Piro 1991; Ballantyne Ross & Fabian 2001).

Above 7.1 keV there is little absorption by metals and harder photons tend to Compton scatter back out of the disc, whereas incident soft photons are mostly absorbed. As a result, the reflection spectrum is suppressed by a factor of about σ_T/σ_{pe} , where σ_{pe} is the photoelectric absorption cross-section for the respective element. The

reflection spectrum peaks at energies between ~ 30 keV, where the incident photons are most likely to be reflected by the disc. Above these energies, electron recoil becomes important and incident photons are down-scattered to much lower energies and subsequently absorbed. This produces the turn-over in the reflection spectrum at ~ 50 keV. Moreover, there is a fluorescent line spectrum that results from the most abundant metals. The strongest of these lines is from Fe $K\alpha$, given its relatively high cosmic abundance and fluorescent yield.

As the disc is under constant bombardment by hard X-rays it is reasonable to consider reflection off ionised matter. The reflection spectrum has been re-calculated allowing the gas to be in different ionised states³ (e.g. Ross & Fabian 1993; Życki et al. 1994; Ross, Fabian & Young 1999). Detailed discussion of the emerging spectrum is given in the listed references, but it is important to note that the reflection spectrum and the Fe $K\alpha$ feature emerging from an ionised disc are very sensitive to the ionisation parameter ξ (right panel of Fig. 1.5).

1.5.2 Fe $K\alpha$ emission

The Fe $K\alpha$ ⁴ emission line is intrinsically a narrow feature (1 eV; Pozdnyakov, Sobol & Sunyaev 1979). However, the observed line profile is altered by the motions in the medium from which it originates, specifically, the accretion disc (Fabian et al. 1989; Laor 1991). In Fig. 1.6, a schematic description of the line altering effects (Doppler shifts and relativistic considerations) is given.

Consider a narrow annulus on a disc at some distance from the central mass, and viewed edge-on, such that one side of the disc approaches the observer while the other side recedes. If the disc is non-relativistic, a symmetric double-horned profile will emerge as the approaching material is shifted to higher energies (blueshifted) and the receding material is shifted to lower energies (redshifted) (top panel of Fig. 1.6). If the emission region is closer to the black hole, such that the disc is moving at speeds of about $0.3c$, special relativistic effects become considerable (second panel of Fig. 1.6). Special relativistic beaming (i.e. flux boosting) will enhance the emission from the blue-horn of the line and diminish the intensity of the red-horn, resulting in an asymmetric profile. In addition, the transverse Doppler effect (“moving clocks run slowly”) shifts the entire profile to lower energies. Finally, emission originating from within the deep potential well of the black hole will suffer from gravitational redshifting which will broaden the line and further shift the profile to lower energies (third panel of Fig. 1.6). The resulting profile (fourth panel of Fig. 1.6) will be the combination of all these effects summed over many annuli. The physical picture is further complicated by the inclination of the disc, ionisation state of the disc, disc emissivity, and black hole spin (e.g. see Laor 1991).

³The degree of ionisation for a constant density gas is defined by the ionisation parameter $\xi = 4\pi F_x/n$, where F_x is the illuminating flux and n is the gas density. Specifically, ξ measures the ratio of the photoionisation rate, which is $\propto n$, to the recombination rate, which is $\propto n^2$.

⁴The neutral Fe $K\alpha$ emission at 6.4 keV is actually a combination of two components: $K\alpha_1$ at 6.404 keV and $K\alpha_2$ at 6.391 keV. It is rare that the components are referred to separately.

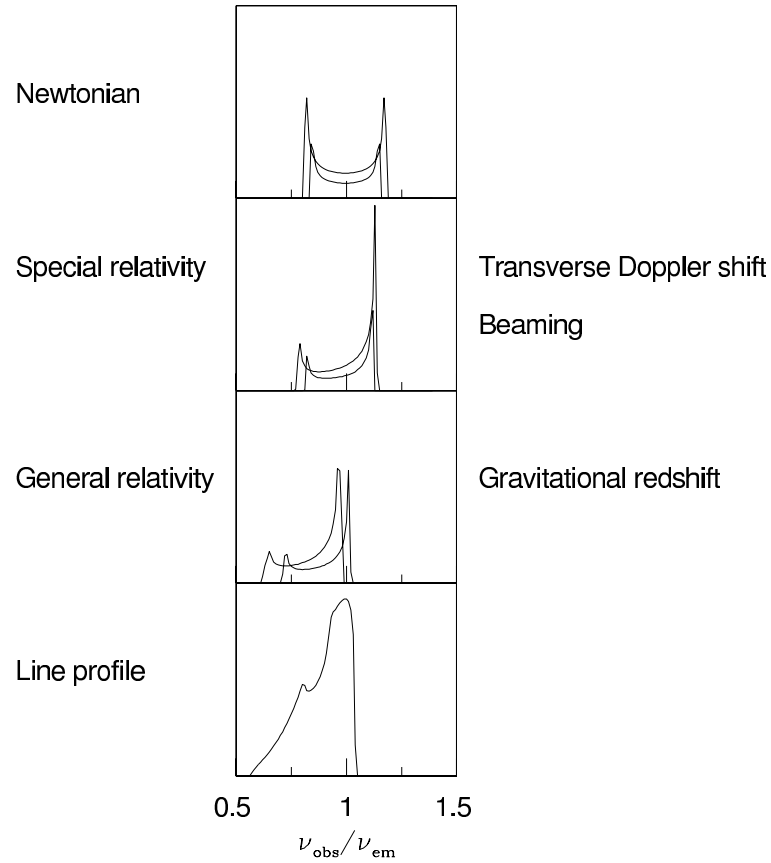


Figure 1.6: The asymmetrically broadened iron line seen in some AGN is produced by the interplay of several mechanisms (see text for greater detail). Firstly, (top panel) the contribution from different annuli on the disc form a double-peaked profile due to Keplerian motions. Special relativistic effects, specifically transverse Doppler shifting and beaming, produce the redshifted, asymmetric profile (second panel). Gravitational redshifting further broadens and redshifts the line (third panel). The predicted profile is a combination of all these effects summed over many annuli (fourth panel). Figure taken from Fabian et al. (2000).

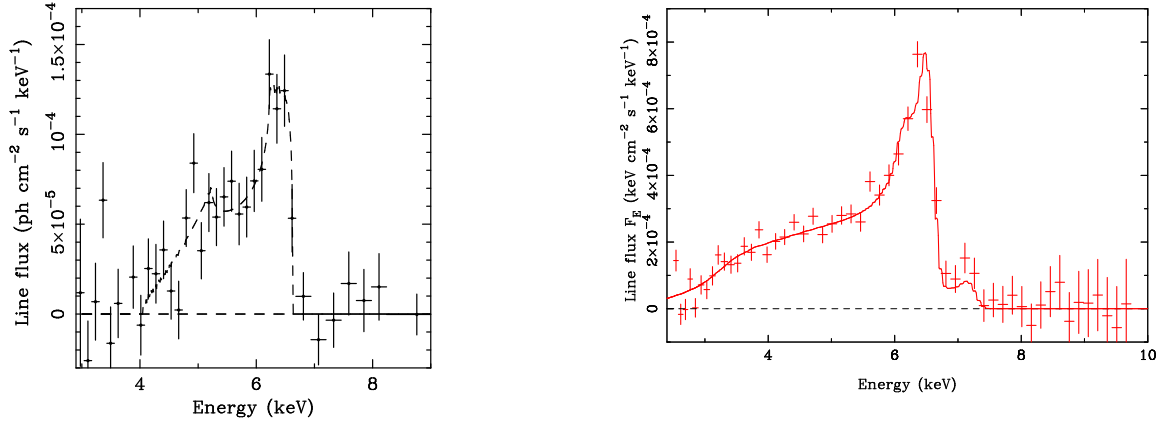


Figure 1.7: Left panel: The first detection of the double-horned relativistic profile observed in MCG-6-30-15 with *ASCA*. Figure taken from Tanaka et al. (1995). Right panel: The highest signal-to-noise data of the Fe $K\alpha$ line in MCG-6-30-15 observed with *XMM-Newton*. Figure taken from Fabian et al. (2002).

While there is strong theoretical foundation for the existence of relativistically broadened lines, detecting them with high significance is difficult. *ASCA* had apparently discovered these features in a large number of AGN (Nandra et al. 1997; Yaqoob et al. 2002), but very few of the detections have been confirmed with *Chandra* or *XMM-Newton*. These features are very difficult to model as accurate determination of the continuum is required. The situation is further complicated if the discs are ionised (see Section 1.5.1).

However, the most convincing detection of a relativistic Fe $K\alpha$ feature comes from the spectrum of the Seyfert 1 MCG-6-30-15 first discovered with *ASCA* (Tanaka et al. 1995) and later confirmed with *XMM-Newton* (Wilms et al. 2001; Fabian et al. 2002). In Fig. 1.7 the first *ASCA* detection (Tanaka et al. 1995) and the highest signal-to-noise detection (Fabian et al. 2002) are presented.

1.5.3 Light bending considerations

The iron line and reflection continuum, in general, are perhaps the most powerful diagnostic tools in understanding AGN and black holes. In principle, the next generation of X-ray telescopes will make Fe $K\alpha$ reverberation mapping (Reynolds et al. 1999) possible, which would ultimately reveal the accretion disc geometry and allow the most accurate black hole mass measurements (as well as confirm the existence of black holes in AGN). However, there are many challenges that need to be understood to utilise these tools. For example, there is certainly a shortage of detected lines, even though they are expected to arise naturally in most type-1 Seyferts. It may be that the line profiles are more difficult to constrain due to ionisation of the disc. If so, this should be overcome with more sensitive observations (see Chapter 9). However, other issues may be more fundamental to our understanding than our tech-

nology. As will be discussed throughout this dissertation, the X-ray spectra of many NLS1 can be described by reflection. However, iron lines with equivalent widths of $EW \approx 1 - 5 \text{ keV}$ are often required. Such strengths are orders of magnitude higher than predicted by theory. Secondly, a simple correlation between the variability of the power-law component and that of the reflection component is expected (with a short time delay); however a much more complicated relation has been observed (e.g. Vaughan & Edelson 2001). A theory to overcome these issues in the standard picture has been developed (e.g. Martocchia & Matt 1996; Martocchia, Karas & Matt 2000; Dabrowski & Lasenby 2001) and applied to some Seyfert 1s.

In the standard reflection picture, half of the hard X-ray photons reach the observer as direct power-law continuum while the other half illuminate the disc and are reprocessed as the reflection component. The X-ray variability is assumed to arise from physical changes in the primary source (e.g. flares due to magnetic reconnection, or hot-spots on the disc). The light bending model considers a different perspective. The primary continuum source has constant intrinsic luminosity. The observed variability is induced by gravitational light bending as the height of the primary source above the accretion disc varies (Fig. 1.8).

Consider a compact primary continuum source at some height above the accretion disc. If the height above the accretion disc is small (a few r_g), a large fraction of the emitted photons are bent toward the disc by the strong gravitational field of the central black hole, strongly reducing the direct power-law component which reaches the observer. In this case, most of the light will be reprocessed by the disc and the observed spectrum will be reflection dominated (left panel of Fig. 1.8). As the height of the source above the disc increases, the gravitational potential that the primary photons need to overcome is less. As a result the strength of the direct power-law component increases, while the reflection component diminishes (middle and right panels of Fig. 1.8).

The scenario works considerably well at describing the seemingly unpredictable variability of the reflection component with respect to the power-law continuum (Miniutti et al. 2003; Miniutti & Fabian 2004). In addition, Dabrowski & Lasenby (2001) demonstrated that Fe $K\alpha$ lines with extreme strengths ($EW \approx 5 \text{ keV}$) could be recovered depending on the location of the primary *hot spot* with respect to the rotation axis of the black hole and the observers line-of-sight. Moreover, in the reflection dominated state, the soft-excess could be attributed to the reflection component (Ross & Fabian 2004, in preparation). Given the resolution of current X-ray instruments and the added effects of relativistic blurring, the emission line excess could manifest itself as a blackbody with a characteristic temperature of $100 - 200 \text{ eV}$.

The physical nature of the light bending model remains debatable. The above description is best employed when considering a compact source (the primary continuum) which is centrally concentrated and close to the axis of a rotating black hole. The source could be related to magnetic dissipation due to flaring events (as discussed in Section 1.2.3). Other alternatives are that the source is associated with the inner part of an aborted jet producing relativistic particles illuminating the disc (Malzac et al. 1998), or the aborted jet itself (Ghisellini, Haardt & Matt 2004), or self-Compton

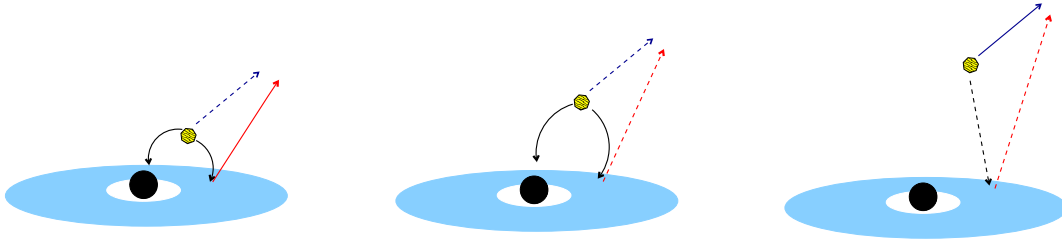


Figure 1.8: The principle behind the light bending scenario. The ‘primary’ continuum source located above the black hole/accretion disc system has constant luminosity, and only its height above the disc changes. The observer (located to the upper right) sees the direct (power-law) continuum from the primary source, as well as the reflected continuum from the disc (the more dominate component is marked with a solid line). Left panel: The primary source is closest to the black hole. Much of the light from the primary source will be ‘bent’ back toward the black hole/accretion disc. The observer will detect a spectrum which is dominated by the reflection component. Middle panel: The intermediate state in which much of the direct power-law component reaches the observer, as well as some reflection component. Right panel: The source height above the disc is at its maximum. The power-law continuum is dominate, whereas the reflection component is minimised. The total luminosity of the system increases as the height of the primary source above the disc increases.

emission from the base of a weak jet (e.g. Markoff, Falcke & Fender 2001).

1.6 XMM-Newton

1.6.1 The observatory

The *X-ray Multi-Mirror Mission (XMM-Newton)*; Jansen et al. 2001; Ehle et al. 2004) was launched from French Guyana on 1999 December 10. Six science instruments operate simultaneously while the space observatory travels its 48-hour highly elliptical orbit. The crux of the observatory are three Wolter-1 X-ray telescopes, each with an effective area of 1550 cm^2 at 1.5 keV, making *XMM-Newton* the most sensitive focusing X-ray telescope to date. Each telescope has a focal length of 7.5 m, and consists of 58 nested mirrors with the diameter of the largest being 70 cm. The three telescopes focus in-coming X-ray photons onto three detectors of the European Photon Imaging Camera (EPIC), each capable of working in several instrumental modes, and two Reflecting Grating Spectrometers (RGSs; den Herder et al. 2001). The sixth instrument is a 30 cm optical telescope (Optical Monitor (OM); Mason et al. 2001) which collects data in the optical and near-UV regime, rendering it possible to conduct simultaneous optical and X-ray studies.

Two of the X-ray telescopes are identical, and contain a grating assembly in their light path which disperses about 40% of the light onto a linear strip of 9 CCDs. The assemblies in each telescope make up the RGSs. About 44% of the light reaches the prime focus of the two telescopes undispersed, where a Metal-Oxide Semi-conductor (MOS1 or MOS2; Turner et al. 2001) camera is installed. The remaining light is absorbed by the support structures of the Reflection Grating Array. X-rays reach the prime focus of the third telescope unaffected by any assembly structures, and are detected by the EPIC pn (p-n-junction) camera (Strüder et al. 2001).

1.6.2 EPIC calibration and background

“The three most important things in X-ray astronomy are: calibration, calibration, and calibration.”

Keith Arnaud
August 2002

This is even more true when working with the most sensitive X-ray telescope of all time, since discoveries cannot be independently confirmed with other observatories. In the case of *XMM-Newton* this will remain so, until at least 2015 when the next generation of X-ray telescopes are planned to be put into commission. As such it is important to consider the calibration of the *XMM-Newton* instruments, and how the data used in this dissertation are affected. At some point throughout this dissertation every instrument on *XMM-Newton* is used; however, due to the limited brightness of the sources under study, the EPIC instruments are utilised the most since they

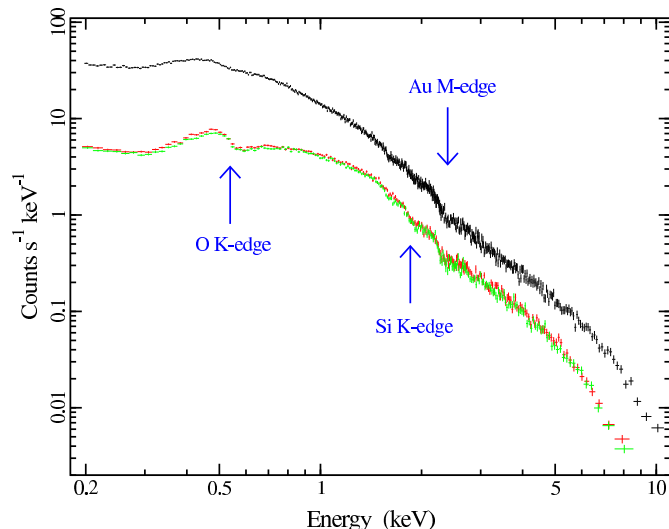


Figure 1.9: The EPIC spectra of the power-law source PKS 2155-304. The pn data (top curve) and MOS1 and MOS2 data (lower curves) are imprinted with instrumental features. The energies of the three strongest features are marked.

are the most sensitive. The discussion in this Section will concentrate on the EPIC calibration.

Spectral calibration

In X-ray astronomy the observed spectrum ($C(I)$) is not the true spectrum of the source, but rather the number of counts collected per instrument channel. $C(I)$ is related to the energy source spectrum ($M(E)$) folded through the instrumental response ($r(I, E)$), such that:

$$C(I) = \int_0^{\infty} M(E)r(I, E)dE \quad (1.10)$$

The instrumental response is accounted for by the *response matrix* which considers the probability that a photon of a certain energy will be detected in a specific detector channel. Factors which influence the instrumental response most significantly are the materials from which the telescope itself is built from, for example, gold from the mirrors and silicon from the detectors will absorb some X-ray photons. Consequently, features arising from the instruments are imprinted on the spectrum of every object observed, regardless of the X-ray telescope used (Fig. 1.9).

To minimise these effects, response matrices are generated which essentially model the instrumental features so that the “true” source spectrum can be derived. This is not a straightforward task as there are a number of factors which alter the instrumental model. For example:

- Some features are time variable. The process of transferring charge from pixel-to-pixel (described by the Charge Transfer Efficiency; CTE) is spatially and

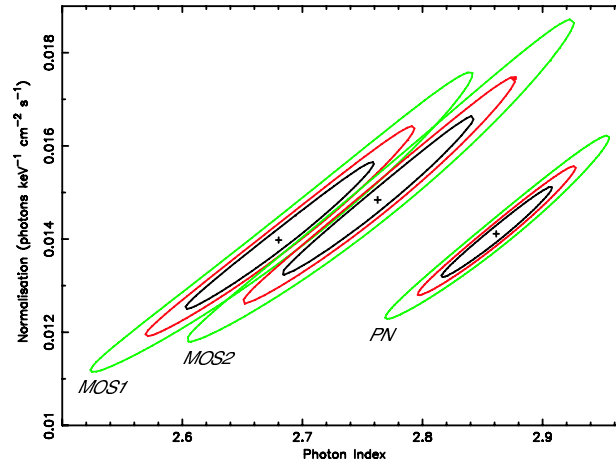


Figure 1.10: The 1σ , 2σ , and 3σ contours around the best-fit photon indices derived from fitting the 3 – 10 keV EPIC data of PKS 2155–304 with a power-law.

temporally changing, which results in changes in the relative appearance of the instrumental features.

- The modelling of a specific feature is not independent of other features. Modifications to correct one (e.g. a gain correction) may degrade the calibration of another.
- The true extent of the calibration uncertainties are only seen in very high signal-to-noise data when the systematic errors dominate over the statistical uncertainties. In cases of high signal-to-noise data, the response matrix may attempt to “overcompensate”, and hence introduce additional residuals to the fit.

In Fig. 1.9, the pn, MOS1, and MOS2 data from the blazar PKS 2155–304 are shown with the most significant instrumental features marked. PKS 2155–304 is a good calibration source because it is bright, compact, and its spectrum is featureless and power-law in nature. The strongest instrumental features are the K-edges of O and Si, and the M-edge of Au. Elsewhere, and in particular above ~ 5 keV, the object spectrum is relatively free of instrumental features. It is important to stress this point, especially when the detection of edge-like features above ~ 7 keV are discussed (Chapters 2 and 4). Also, in the case of I Zw 1 (Chapter 6), an emission/absorption-type feature detected at ~ 0.55 keV is handled rather conservatively due to the instrumental O K-edge close to this energy.

A power-law fitted to the 3–10 keV data illustrates another calibration uncertainty, and that is that the three EPIC instruments show different photon indices. In Fig. 1.10, the 1σ , 2σ , and 3σ contours are shown around the best-fit photon indices measured from the pn, MOS1, and MOS2 data. Clearly the photon indices measured by the three instruments are inconsistent, with the largest discrepancy being between the pn and the two MOSs. Interestingly, the result shown here for PKS 2155–304 is atypical. Normally the MOS2 and pn tend to agree quite well, while the MOS1 is dissimilar

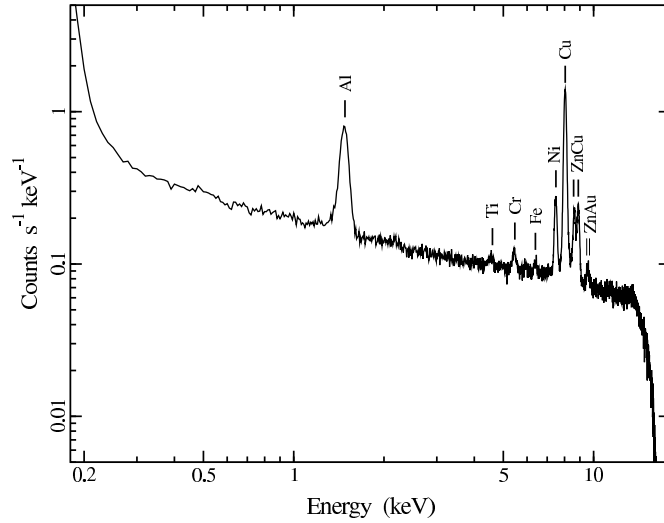


Figure 1.11: The EPIC pn background spectrum in the 0.2 – 18 keV range obtained from 313 ks of closed-filter, full-frame mode data. Some emission lines are marked. Data courtesy of M. Freyberg.

(Molendi & Sembay 2003, and chapters throughout this dissertation). Throughout this work the uncertainty in the photon indices is handled by allowing the photon indices from each instrument to vary independently of one another.

The intrinsic background is made up of the electronic noise, induced emission by high-energy particles, and cosmic rays passing through the telescope. In the 2 – 7 keV band the flux is about $0.1 \text{ erg cm}^{-2} \text{ s}^{-1}$. In Fig. 1.11 the intrinsic background spectrum for the EPIC pn instrument is presented. The spectrum was created from 3 years of calibration (closed-filter), full-frame data (313ks) by Freyberg et al. (2004). While the background spectrum is different for each observing mode, the figure illustrates the various emission features and relative normalisations. As is evident, the strongest features are from Al at 1.5 keV, and Cu at 8 keV. Freyberg et al. (2004) also demonstrated that some of the features (particularly Ni, Cu) are spatially inhomogeneous, with intensities corresponding to the electronics board mounted below the CCDs. On the other hand, the Al background is rather homogeneous. The lesson here is that careful background selection is fundamental to the spectral analysis. In Chapter 2, the background selection becomes questionable when a sharp spectral drop is discovered in IRAS 13224–3809 at $\sim 8 \text{ keV}$. It is not unreasonable to think that the feature could be an artifact of improper background subtraction, mainly due to Cu. However, the background is examined carefully, and a number of background regions are selected and analysed. In addition, the strength of the source feature cannot be accounted for by the background Cu.

1.7 Spectral fitting

Thus far the focus of the discussion has been in understanding the instrumental response ($r(I, E)$). In the remainder of this Section the attention will be on deriving the intrinsic source spectrum ($M(E)$).

Unfortunately, inverting Equation 1.10 to determine the source spectrum is not straightforward, as the solution tends to be non-unique and unstable to small perturbations in the observed spectrum (see Arnaud & Dorman (2002) and references within). Alternatively, a parameterised model representing the true spectrum is created, folded with the response matrix, and compared to the observed data. The model parameters are varied, and the process is repeated until the “best-fit” model is achieved, and the “best-fit” model parameters are determined.

Spectral fitting of all data in this dissertation is accomplished with the interactive X-ray spectral-fitting programme `XSPEC` (Arnaud 1996). `XSPEC` uses a modified Levenberg-Marquardt algorithm to calculate the best-fit model. A caveat is that the technique is a local one, and care must be taken to avoid confusing a local minimum with the global best-fit. During this work initial model parameters were selected from multiple, reasonable starting locations to increase the likelihood of finding the true minimum. Chi-square (χ^2) statistics are used to test the quality of the fits. To ensure that χ^2 statistics are applicable, the data are binned such that a minimum of 20 counts (but usually more) are in each bin.

`XSPEC` offers a multitude of models to fit data. As described in Section 1.2.1, the X-ray spectra of AGN can be generalised to some extent. As such, some `XSPEC` models are used quite frequently throughout this work. What follows is a general description of the models most often used in this dissertation.

Galactic absorption and element abundances

The photoelectric absorption of X-rays by neutral Galactic hydrogen in the line-of-sight is considered in all models. Hydrogen column densities are adopted from various studies (e.g. Dickey & Lockman 1990 or Elvis et al. 1991) depending on the object being analysed. This adopted value is taken to be the best-fit value, and not permitted to vary. Absorption cross-sections from Balucinska-Church & McCammon (1992), and element abundances from Anders & Grevesse (1989) are assumed throughout.

Thermal emission from an accretion disc

Though the true nature of the soft-excess is not known, it is normally treated as thermal emission from an accretion disc, crudely approximated as a single blackbody spectrum (Planck function). In this case the free model parameters are the temperature of the blackbody and the source flux. In the presence of higher quality data, the spectrum is treated more realistically as emission from multiple blackbody components (Mitsuda et al. 1984; Makishima et al. 1986). Here the free parameters are the temperature at the inner disc radius, and a normalisation factor which is dependent on the inner disc radius, disc inclination, and source distance.

Comptonisation

Comptonisation processes are normally fitted with a simple power-law, where the free parameters are the dimensionless photon index (Γ) and the 1 keV flux (F). This is normally sufficient in describing the 0.3 – 10 keV spectrum since the power-law cutoff in AGN is expected at much higher energies (see Section 1.2.3). However, in some cases (e.g. Chapters 2, 4, and 7), it would appear that a “curved” power-law, is a better approximation to the data. In these situations a power-law with a low-cutoff energy ($E_c < 10$ keV) is used to mimic the effect of a curved power-law. This is not considered a physical solution, but simply gives a better fit.

Lines and edges

All of the objects studied in this dissertation are too dim to fully exploit the high resolution of the RGS. As such, emission and absorption lines detected in the moderate resolution EPIC instruments can be adequately modelled with a Gaussian profile. The free parameters are the line energy, width, and flux.

Above a threshold energy (E_{edge}) the spectrum modified by an absorption edge is absorbed by an amount:

$$a(E) = e^{-\tau(E/E_{edge})^{-3}}$$

where τ is the opacity through the absorber (optical depth).

In some objects (e.g. I Zw 1; Chapter 6), due to modest spectral resolution, and possible blending of the warm absorber features, it is often not possible to distinguish between edges and absorption/emission lines.

1.8 Outline of this dissertation

The high sensitivity of *XMM-Newton* across a large energy range allows us to examine, essentially for the first time in detail, the broad-band properties of NLS1. In this dissertation I present analyses of five of the most intriguing NLS1.

ROSAT observations of IRAS 13224–3809 revealed some of the most extreme variability ever observed in a radio-quiet AGN. The spectral and timing properties of this enigmatic object are discussed in Chapters 2 and 3, respectively.

1H 0707–495, known for its persistent and rapid variability, was the first NLS1 discovered with *XMM-Newton* to exhibit a sharp spectral drop at high energies. A second *XMM-Newton* observation of 1H 0707–495 was conducted two years after the first. In Chapters 4 and 5, the two observations of 1H 0707–495 are compared, and its behaviour is described in the context of partial covering and reflection.

The optical properties of I Zw 1 exemplify the NLS1 class, and hence it has become known as the prototype NLS1. However, as will be shown in Chapter 6, its X-ray spectral properties are atypical of most other members of its class.

A *ROSAT* monitoring campaign of PHL 1092 demonstrated extreme variability similar to IRAS 13224–3809. In contrast to IRAS 13224–3809, PHL 1092 is a very luminous quasar, and the measured luminosity changes indicated a radiative efficiency

in excess of what is expected from accretion by a Kerr black hole. The most sensitive X-ray observation of PHL 1092 is discussed in Chapter 7.

The strong soft-excess and rapid variability of NAB 0205+024 have made it an important object to study the nature of NLS1 behaviour in luminous narrow-line quasars. The X-ray analysis of NAB 0205+024 is presented in Chapter 8. The X-ray brightness of NAB 0205+024 (compared to other similar objects) affords us the opportunity to study the NLS1 phenomenon in a quasar with relatively high signal-to-noise.

A summary of the results and discussion of future prospects is given in Chapter 9.

Chapter 2

Spectral properties of the Narrow-Line Seyfert 1 galaxy IRAS 13224–3809

2.1 Introduction

ROSAT, *ASCA*, and *XMM-Newton* have shown that many Narrow-Line Seyfert 1 galaxies (NLS1) possess remarkable X-ray properties compared to their broad-line counterparts. NLS1 are generally characterised by a strong soft X-ray excess, steep power-law continuum, and extreme X-ray variability (e.g. Puchnarewicz et al. 1992; Boller, Brandt & Fink 1996; Brandt, Mathur & Elvis 1997; Brandt & Boller 1998; Vaughan et al. 1999). With the superior sensitivity of *XMM-Newton* came the discovery of further complexity in the form of sharp spectral drops above 7 keV without significant Fe-K emission (Boller et al. 2002; Fabian et al. 2002). In the case of 1H 0707–495 two physical interpretations were discussed: (i) partial covering (e.g. Holt et al. 1980; Rees 1987; Celotti, Fabian & Rees 1992; Brandt & Gallagher 2000), in which the sharp drop is attributed to absorption by iron in dense clouds (Boller et al. 2002; Chapter 4), and (ii) a reflection-dominated accretion disc spectrum (Fabian et al. 2002), where the drop is ascribed to the blue edge of a relativistically broadened iron line. Both models provided acceptable spectral fits to the 1H 0707–495 data. The very high iron overabundance in the Boller et al. (2002) interpretation was significantly reduced to more realistic values in the reanalysis by Tanaka et al. (2004).

In this Chapter, the discovery of a high-energy, sharp spectral drop in a second NLS1, IRAS 13224–3809, is discussed. IRAS 13224–3809 is one of the most exciting NLS1 to study as it exhibits many of the extreme characteristics that make this class of objects so interesting. Strong Fe II emission in its optical spectrum (Boller et al. 1993); a giant soft X-ray excess (Boller et al. 1996; Otani et al. 1996; Leighly 1999a; Boller et al. 2003); extreme, rapid, and persistent variability in X-rays (Boller et al. 1996; Otani et al. 1996; Boller et al. 1997; Leighly 1999b; Chapter 3); and now, sharp spectral features, are all traits of IRAS 13224–3809.

2.2 X-ray observations and data analysis

IRAS 13224–3809 was observed with *XMM-Newton* (Jansen et al. 2001) on 2002 January 19 during revolution 0387 for about 64 ks. During this time all instruments were functioning normally. The EPIC pn camera (Strüder et al. 2001) was operated in full-frame mode, and the two MOS cameras (MOS1 and MOS2; Turner et al. 2001) were operated in large-window mode. All of the EPIC cameras used the medium filter. The two Reflection Grating Spectrometers (RGS1 and RGS2; den Herder et al. 2001) also gathered data during this time. The Observation Data Files (ODFs) were processed to produce calibrated event lists using the *XMM-Newton* Science Analysis System (SAS v5.3.0). Unwanted hot, dead or flickering pixels were removed as were events due to electronic noise. Event energies were corrected for charge-transfer losses. The latest available calibration files were used in the processing. Light curves were extracted from these event lists to search for periods of high background flaring. A significant background flare was detected by the EPIC cameras approximately 20 ks into the observation and lasted for ~ 5 ks. Although the total background counts at flare maximum were only one-third of the source counts (in the pn data), the segment was excluded during most of the analysis. The total amount of good exposure time selected was 55898 s and 58425 s for the pn and MOS detectors, respectively. The source plus background photons were extracted from a circular region with a radius of $35''$, and the background was selected from an off-source region and appropriately scaled to the source region. Single and double events were selected for the pn detector, and single-quadruple events were selected for the MOS.

High resolution spectra were obtained with the RGS. The RGS were operated in standard Spectro+Q mode for a total exposure time of 63963 s. The first-order RGS spectra were extracted using RGSPROC, and the response matrices were generated using RGSRMFGEN.

The Optical Monitor (OM; Mason et al. 2001) collected data in the fast mode through the UVW2 filter ($1800 - 2250 \text{ \AA}$) for about the first 25 ks of the observation. For the remainder of the observation the OM was operated in the grism mode. In total, seven photometric images were taken, each exposure lasting 2000 s.

2.3 X-ray spectroscopy

The source spectra were grouped such that each bin contained at least 20 counts. Spectral fitting was performed using XSPEC v11.2.0 (Arnaud 1996). Fit parameters are reported in the rest frame of the object. The quoted errors on the model parameters correspond to a 90% confidence level for one interesting parameter (i.e. a $\Delta\chi^2 = 2.7$ criterion). The Galactic column density toward IRAS 13224–3809 is $N_{\text{H}} = 4.8 \times 10^{20} \text{ cm}^{-2}$ (Dickey & Lockman 1990). Element abundances from Anders & Grevesse (1989) are used throughout. Luminosities are derived assuming isotropic emission and a standard cosmology with $H_0 = 70 \text{ km s}^{-1} \text{ Mpc}^{-1}$, $\Omega_M = 0.3$, and $\Omega_\Lambda = 0.7$.

In the following analysis the EPIC pn data are used to constrain the sharp spectral feature at 8 keV as they contain the highest photon statistics. The energy range up to

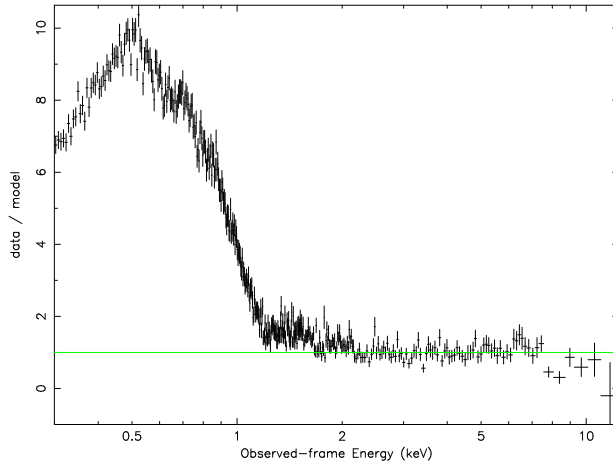


Figure 2.1: Residuals (data/model) remaining from fitting a simple power-law model to the 2 – 7 keV EPIC pn data of IRAS 13224–3809, and extrapolating to higher and lower energies. The sharp spectral feature at ~ 8 keV, and the soft X-ray excess emission are most prominent. The photon index in the 2 – 7 keV band is ($\Gamma = 1.9 \pm 0.1$).

about 12 keV can be explored with the EPIC pn while above that energy the spectrum becomes background dominated. Above 8 keV, a total of 120 source plus background and 68 background counts were collected. The combined MOS1 and MOS2 spectrum is dominated by high background at energies greater than 6 keV.

2.3.1 Mean spectral properties

Discovery of a sharp spectral feature

For illustrative purposes, a simple power-law is fitted to the 2 – 7 keV pn spectrum of IRAS 13224–3809, and extrapolated to higher and lower energies (Fig. 2.1). The most obvious features are the strong excess emission below about 1.5 keV, and the presence of a sharp spectral drop at ~ 8 keV. Fitting the 2 – 12 keV spectrum with a simple power-law and edge model, resulted in the edge parameters, energy (E) and optical depth (τ), having values of $E = 8.2 \pm 0.1$ keV and $\tau = 1.12^{+0.76}_{-0.45}$ (Fig. 2.2). The flux absorbed by the edge is $\sim 4.3 \times 10^{-14}$ erg cm $^{-2}$ s $^{-1}$.

An emission feature is marginally detected ($\Delta\chi^2 = 8$ for the addition of 3 free parameters to the edge and power-law fit) at $E = 6.86 \pm 0.16$ keV. The strength of the line (equivalent width; EW) is about 200 eV, and the line flux is $\sim 1.0 \times 10^{-14}$ erg cm $^{-2}$ s $^{-1}$. The line energy is entirely consistent with emission from H- and He-like iron.

A partial covering model

The observed spectrum shows no intrinsic cold absorption above the Galactic column density, but there does exist an abrupt flux drop at 8.2 keV, most likely due to an

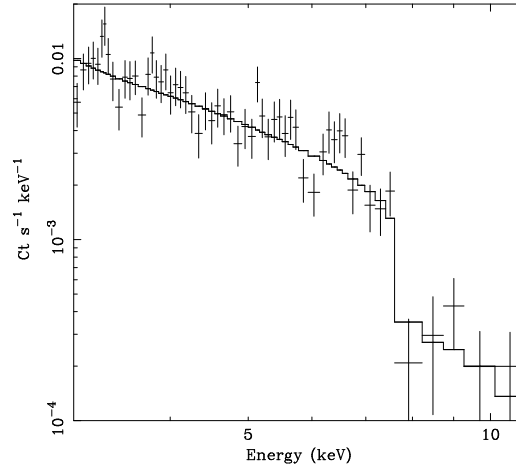


Figure 2.2: A simple power-law and edge fitted to the 2–12 keV band. The edge parameters are $\tau = 1.12^{+0.76}_{-0.45}$ and $E = 8.2 \pm 0.1$ keV.

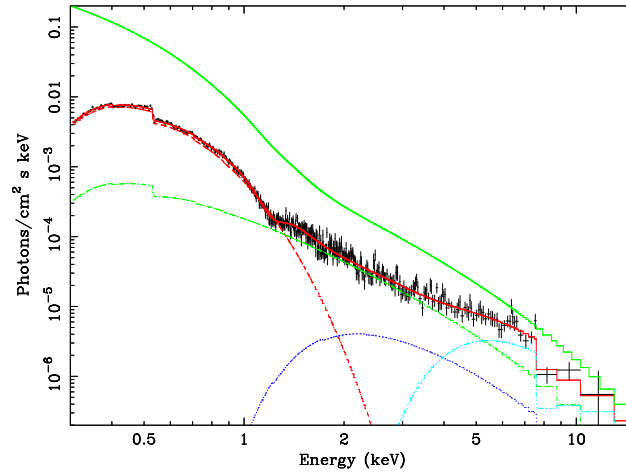


Figure 2.3: Double partial covering model applied to the EPIC pn spectrum of IRAS 13224–3809. The continuum emission is a blackbody and cutoff power-law (see text for details). The upper (green) curve is the absorption-corrected (intrinsic) spectral model.

absorption edge. The energy of the edge is significantly different from that of the neutral iron absorption edge at 7.1 keV. If the absorption edge and possible line emission are related by photoionisation processes (e.g. the fluorescent yield) then the measured line-to-edge flux ratio is in disagreement with the expectation that the absorber is in a spherically symmetric distribution (in the case of spherical symmetry the line-to-edge flux ratio should concur with the fluorescent yield for iron).

However, it is unlikely that the line and edge are physically associated. If the edge was formed in photoionised material, then the measured edge energy would correspond to the K-edges of Fe XVIII-XX, and accompanying line emission should be seen at ~ 6.6 keV. The detected line at $E = 6.86 \pm 0.16$ keV is inconsistent with this scenario, and clearly due to higher ionisation states of iron [at least He-like iron ($E = 6.7$ keV)]. On the other hand, if the sharp feature is a blueshifted neutral edge, then a narrow, blueshifted, neutral iron line is expected at ~ 7.3 keV. Again, the measured width and energy of the marginally detected line at $E \approx 6.86$ keV is inconsistent with this picture. The observed features can be explained in terms of absorption if allowances are made for partial covering (i.e. a patchy absorber; Holt et al. 1980).

A partial covering model was applied to the pn data. The fit comprised of a multi-coloured disc (MCD; Mitsuda et al. 1984; Makishima et al. 1986) model for the soft-excess, and a partially covered power-law for the hard continuum. In addition, the model required an absorption feature at ~ 1.2 keV (see below), which was accounted for by subtracting a Gaussian profile. A good fit was obtained [$\chi^2 = 510/471$ degrees of freedom (dof)] using two absorbers (i.e. double partial covering; see Equation 1.9), but a very steep photon index was required ($\Gamma \simeq 3.4$). The photon index appears extreme given the typical values found in AGN (e.g. Brandt, Mathur & Elvis 1997; but see Gierlinski & Done 2004). Replacing the straight power-law with a cutoff power-law did not improve the fit ($\chi^2 = 509/470$ dof), but did result in more conservative spectral slopes. The model is shown in Fig. 2.3. The best-fit inner-disc temperature was $kT = 160$ eV, and the power-law parameters were $\Gamma = 2.0$ and $E_{cut} = 4.4$ keV. The column densities (and covering fractions) of the line-of-sight absorbers were $N_{\text{H}} \approx 1.2 \times 10^{22} \text{ cm}^{-2}$ (0.06) and $\approx 1.5 \times 10^{23} \text{ cm}^{-2}$ (0.77). The Fe abundance was about 10 times solar with a 90% confidence lower limit of 2 times solar. The average effective slope of the cutoff power-law over the 1 – 5 keV band was approximately $\Gamma = 2.5$.

The temperature and (absorption-corrected) luminosity of the disc require that its inner radius is only about one gravitational radii (assuming a $10^6 M_{\odot}$ black hole). If the soft-excess is in fact physically described by a MCD model then the object would be super-Eddington when bright (see Tanaka et al. 2004).

Detection of Fe L absorption

Additionally, a broad absorption feature at $E = 1.19 \pm 0.02$ keV with an intrinsic width of $\sigma \approx 0.12$ keV, is required in the model with rather high statistical significance (Fig. 2.4). The strength of the line is $EW \approx 120$ eV. The absorbed flux is $1.9^{+0.02}_{-0.04} \times 10^{-13} \text{ erg cm}^{-2} \text{ s}^{-1}$. The RGS1 spectrum is consistent with, but does not constrain, the presence of an absorption feature (no data were collected from RGS2 in the energy

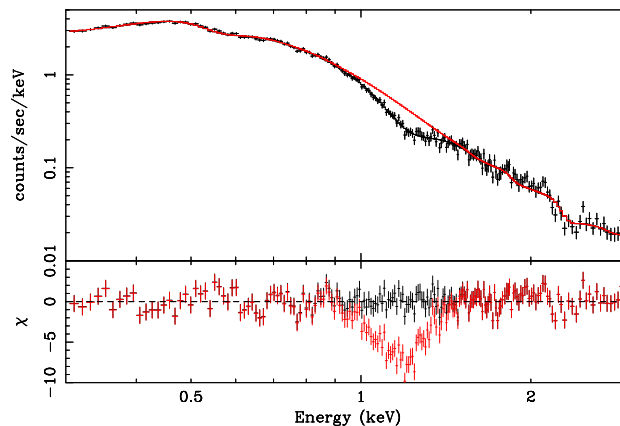


Figure 2.4: Spectral fit to the soft energy spectrum obtained with a double partial covering model (see text for details). Strong residuals are apparent around 1.2 keV, most likely due to Fe-L absorption (light data points). Including a Gaussian profile removes these residuals (dark data points). The significance of the detection is shown in the lower panel in terms of sigma.

range). Other features in the RGS spectra cannot be constrained with the available photon statistics.

The deep absorption feature is similar to that reported by Leighly et al. (1997) from the *ASCA* spectrum. Leighly et al. interpreted the feature as oxygen absorption in a highly relativistic outflow ($0.2 - 0.3 c$). A more prosaic explanation was put forward by Nicastro, Fiore & Matt (1999) who interpreted the feature as a complex of ~ 60 strong resonance absorption lines due mostly to Fe L. Their analysis required a column density of $\log N_{\text{H}} = 23.5$ (cgs) for the absorbing material and an ionisation parameter of $\log \xi = 1$ (cgs). The absorber was outflowing with a velocity of $\sim 1000 \text{ km s}^{-1}$ (see their Figure 4). Such an absorption model does not simply recover the observed 8 keV feature.

An alternative disc-line explanation

In the case of 1H 0707–495, Boller et al. (2002) noted that the sharp drop at 7.1 keV could be the blue wing of a strong, relativistically blurred iron emission line. This would require an unique geometry or environment to achieve such a strong line; the spectrum needs to be reflection-dominated. Fabian et al. (2002) discussed one possibility involving a corrugated inner accretion disc; an alternative would be gravitational light bending (e.g. Martocchia, Matt & Karas 2002; Fabian & Vaughan 2003; Chapters 1 and 5). A reflection dominated spectrum can also be applied to IRAS 13224–3809 (see Fig. 2.5).

Fitting the 2–12 keV spectrum with a power-law continuum plus an emission line with a Laor (1991) profile worked well, resulting in an emissivity index $q = 6.2 \pm 1.2$, inner and outer disc radii of $r_{\text{in}} = 1.3^{+0.2}_{-0.1}$ and $r_{\text{out}} > 180$ gravitational radii, and an inclination of $i \approx 60 \pm 3^\circ$. The disc inclination and emissivity are covariant in the

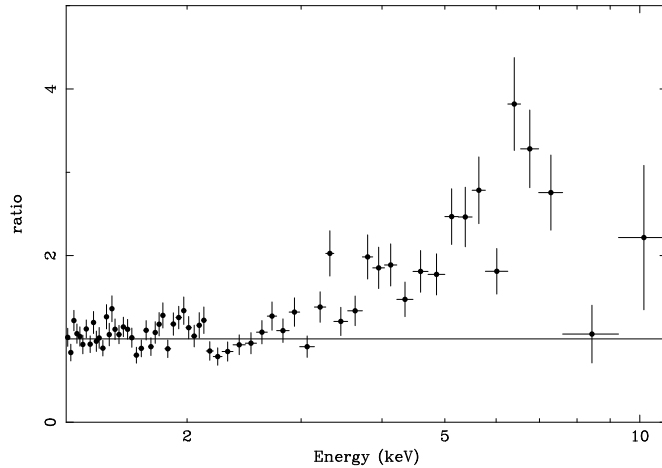


Figure 2.5: The 1–12 keV ratio (data/model) from fitting a power-law between the 1.3–3 keV and 8 – 12 keV bands. The deviations can be seen as a very strong emission line.

fitting, and a wide range of inclination angles are possible. The equivalent width of the line is unusually high at 5.6 keV. To examine whether such a strong line could be produced, the ionised slab models (Ross & Fabian 1993) were applied to the data. With the metal abundances set to 7 times solar, and using Galactic absorption, a mediocre fit ($\chi^2_{\nu} = 1.3$) was obtained over the entire energy range from 0.4 – 12 keV. Some sharp deviations at the 2 – 3 σ level occur at ~ 6 keV and again at ~ 8 keV. As with 1H 0707–495 this model requires the X-ray spectrum to be reflection-dominated. The sharp jump in the spectrum at ~ 1 keV is due to strong line and recombination emission by Fe L, O, and other elements.

2.3.2 Flux-dependent spectral properties

The 0.3 – 10 keV light curve of IRAS 13224–3809 shows strong and rapid variability with flux changes of about a factor of 8 (Fig. 3.1). The variability properties of IRAS 13224–3809 are discussed fully in Chapter 3, but here the high- and low-flux state spectra are examined.

The high- and low-flux spectra are constructed from those intervals in the light curve where the source count rate is ≥ 2.5 count s $^{-1}$ and ≤ 1.5 count s $^{-1}$, respectively. The average fluxes in the two states are different by a factor of three. These two spectra were fitted simultaneously with the same spectral model as in Section 2.3.1 (i.e. double partial covering). With the Fe abundance fixed at 3 times solar, a good fit ($\chi^2 = 667/631$ dof) was obtained (Fig. 2.6). The best fitting continuum parameters were: $kT = 160$ eV, $\Gamma = 2.0$, and $E_{cut} = 4.0$ keV. The column densities (and covering fractions) of the absorbers in the high-flux spectrum were $N_{\text{H}} \approx 1.0$ (0.66) and ≈ 20 (0.53), and in the low-flux spectrum ≈ 3.1 (0.53) and ≈ 23 (0.87), where the column density is in units of 10^{22} cm $^{-2}$. When the flux is low the absorption increases.

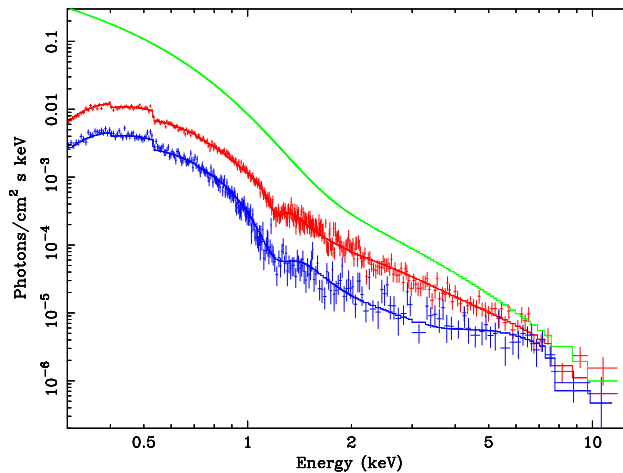


Figure 2.6: Unfolded spectral fits to the high- and low-flux data (middle and lower curve, respectively). Note the flattening of the hard spectrum in the lower flux state. The flattening can be explained in the partial covering scenario by an increased column density and/or increased covering fraction of the absorbing material. The upper curve gives the absorption corrected spectral model.

2.4 Discussion

IRAS 13224–3809 exhibits an unusual combination of spectral features:

- (1) A sharp spectral drop by a factor of ~ 5 at ~ 8 keV.
- (2) Marginal detection of an Fe K emission lines, which likely is not associated with the ~ 8 keV edge.
- (3) A flattening of the spectrum above 3 keV during periods of diminished intensity.
- (4) Strong soft-excess emission.
- (5) A significant Fe L absorption feature at ~ 1.2 keV.

The most plausible explanation for spectral features (1), (2), and (3) appears to be double partial covering. The soft X-ray excess is most probably due to the higher temperature achieved in a slim accretion disc (Abramowicz et al. 1988) as often seen in NLS1 (Mineshige et al. 2000). Presently it is not clear whether the Fe L absorption feature is physically connected with the partial covering scenario.

The lack of strong emission lines and Fe L edge absorption can be explained if the absorber subtends only a small solid angle as seen from the central black hole. An immediate consequence, given the variability in the absorber, is that the absorber must be located close to the central black hole, maybe even within the accretion disc region as suggested by e.g Rees (1987); Celotti, Fabian & Rees (1992); and Brandt & Gallagher (2000). The flattening of the spectrum provides strong evidence for partial covering, as an increased absorbing column and/or a larger covering fraction

is expected when the source flux is low. Although the partial covering model explains the data well, the present photon statistics above the edge still do not allow precise determination of the iron abundance, nor the disentanglement of the covariant covering fraction and absorbing column.

The sharpness of the feature, if due to a photoelectric edge, is surprising. At 8.2 keV the absorbing matter must be partially ionised (the threshold energies for Fe XIX–XXIII are 7.93, 8.07, 8.21, 8.35 and 8.49 keV) in which case a range of ionisation states is expected. These make the observed edge broad rather than sharp (e.g. Palmeri et al. 2002). Alternatively the feature may be a neutral edge in approaching matter (say in a wind or jet along the line-of-sight; Chartas et al. 2002). The velocity of the matter is then required to be $0.15c$ ($c = 2.9979 \times 10^5 \text{ km s}^{-1}$). This then requires a significant outflow of mass and kinetic energy from the object.

The extreme spectral properties detected in NLS1 with *XMM-Newton* should further stimulate a combined theoretical and observational effort to improve our understanding of the physics in the inner-most regions of AGN. To more precisely constrain the form of the sharp spectral feature in IRAS 13224–3809 and distinguish between different models we need a much stronger signal above 8 keV. This may be possible if the source is observed during one of its giant amplitude fluctuations.

Chapter 3

The X-ray variability of IRAS 13224–3809

3.1 Introduction

In Chapter 2 an array of spectral complexities in IRAS 13224–3809 were introduced. In this Chapter the timing properties of IRAS 13224–3809 as observed with *XMM-Newton* are examined and discussed in context of the spectral models presented in Chapter 2.

IRAS 13224–3809 is among the most X-ray variable radio-quiet Seyfert 1 galaxies known. The first systematic X-ray monitoring campaign with *ROSAT* in 1996 showed persistent, rapid, giant-amplitude count rate variability (Boller et al. 1997). Over the course of the observations the largest outburst was by a factor of ~ 60 on hourly time scales. The source flux also rose by a factor of 57 in two days. The *ASCA* monitoring campaign (Otani et al. 1996) further demonstrated that the extreme variability seen with *ROSAT* was not unique, but persistent behaviour in IRAS 13224–3809.

3.2 The UV observation

The apparent *UVW2* (1800–2250 Å) magnitude of IRAS 13224–3809 was 15.21 ± 0.07 corresponding to a flux density of $4.56 \times 10^{-15} \text{ erg cm}^{-2} \text{ s}^{-1} \text{ Å}^{-1}$. The flux density was consistent with previous UV observations with *IUE* (Mas-Hesse et al. 1994; Rodríguez et al. 1997). The rms scatter in the seven hour Optical Monitor (OM) light curve was less than 0.5%. This agrees with the limits on rapid variability from the optical band (Young et al. 1999; but see Miller et al. 2000).

The optical to X-ray spectral index, α_{ox} , was calculated using the definition

$$\alpha_{ox} = \frac{\log(f_x/f_o)}{\log(\nu_x/\nu_o)}, \quad (3.1)$$

where f_x and f_o are the intrinsic flux densities at 2 keV and 1990 Å, respectively.¹ The

¹A conversion from Equation 3.1 to the standard definition of the spectral index between 2500 Å and 2 keV (α'_{ox}) is $\alpha'_{ox} = 0.96\alpha_{ox} + 0.04\alpha_u$, where α_u is the power-law slope between 1990–2500 Å. We assume that $\alpha_u \approx 0$ is reasonable, given the flatness of the UV spectra between 1100–1950 Å (Mas-Hesse et al. 1994).

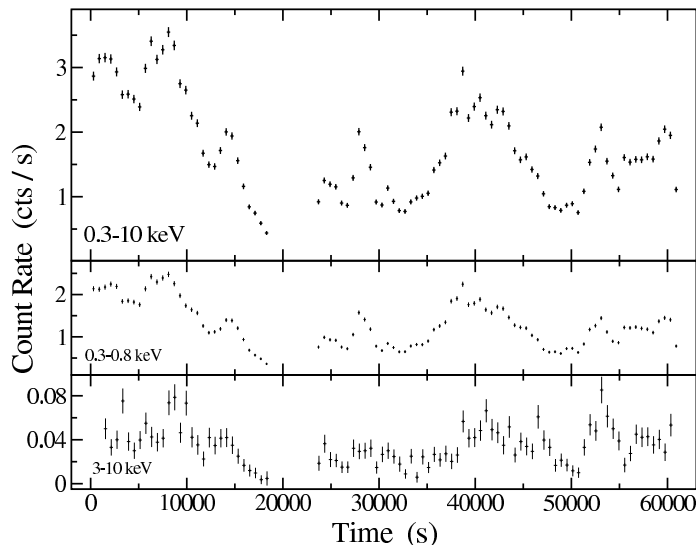


Figure 3.1: Three light curves of IRAS 13224-3809 in 600 s bins. The energy bands (and average count rates) are (from top-down): 0.3–10(1.74), 0.3–0.8(1.30), and 3–10(0.03) keV. Zero seconds on the time axis marks the start of the observation at 03:15:02 on 2002-01-19. The region of high background flaring has been omitted.

selection of the UV wavelength corresponds to the peak response in the *UVW2* filter (2120 Å). Under the assumption that the UV light curve remains constant during the second half of the observation, we determined an average spectral index of $\langle \alpha_{ox} \rangle = -1.57$. As the 2 keV X-ray flux varies, α_{ox} fluctuates from -1.47 in the high state, to -1.73 in the low state.

3.3 The X-ray light curves

In the remainder of the Chapter we will concentrate on the EPIC pn light curve due to its high signal-to-noise. We will make reference to the various flux states, which we have defined as: high ($> 2.5 \text{ count s}^{-1}$), low ($< 1.5 \text{ count s}^{-1}$), and medium ($1.5-2.5 \text{ count s}^{-1}$). The MOS light curves were also analysed and found to be entirely consistent with the pn results. In the interest of brevity, the MOS results will not be presented here.

3.3.1 Flux variability

EPIC pn light curves of IRAS 13224-3809 in three energy bands are presented in Fig. 3.1. The average count rate in the 0.3–10 keV energy band is $(1.74 \pm 0.05) \text{ count s}^{-1}$. Variations by a factor of ~ 8 occur during the observation. Using a 600 s bin size, the minimum and maximum 0.3 – 10 keV count rates are (0.44 ± 0.03) and $(3.55 \pm 0.08) \text{ count s}^{-1}$, respectively. True to its strong soft-excess nature, IRAS 13224-3809

generates nearly three-quarters of the average count rate in the 0.3 – 0.8 keV band. Light curves were compared to a constant fit with a χ^2 test. A constant fit could be rejected for all of the light curves at $> 3\sigma$ significance.

Giant-amplitude flaring events, as observed in the *ROSAT* and *ASCA* observations, are not present during this observation. In fact, the light curve appears to be in a period of relative *quiescence* compared to those earlier observations. The unabsorbed 0.3 – 2.4 keV flux is between $(0.3 - 0.7) \times 10^{-11}$ erg cm $^{-2}$ s $^{-1}$ during the *average* low- and high-flux states. Extrapolation of the data from 0.3 keV to 0.1 keV allows us to estimate a 0.1 – 2.4 keV flux of $(0.4 - 1.1) \times 10^{-11}$ erg cm $^{-2}$ s $^{-1}$. It is interesting to note that while the *XMM-Newton* light curve does not display giant flaring episodes, the flux during this observation is close to the *ROSAT* HRI (0.1 – 2.4 keV) flux during the largest flaring events (3.3×10^{-11} erg cm $^{-2}$ s $^{-1}$; Boller et al. 1997). Therefore, in comparison to the *ROSAT* observations, IRAS 13224–3809 is in a relatively high-flux state. In fact, the median HRI flux over the *ROSAT* 30-day monitoring campaign was $\sim 0.2 \times 10^{-11}$ erg cm $^{-2}$ s $^{-1}$, while the average estimated 0.1 – 2.4 keV flux during this *XMM-Newton* observation is about a factor of three greater. It is not clear, with only the current observation in hand, whether this flux increase is a long-term change (i.e. lasting for periods of days-months), or due to some sort of extended outburst.

Rapid variability

We conducted a search for the shortest time scales for which we could detect variability in IRAS 13224–3809 by employing the excess pair fraction method (Yaqoob et al. 1997). We constructed 90 light curves with time bin sizes from 6 – 1550 s and calculated the excess pair fraction (EPF) for each of them. The results are plotted in Fig. 3.2. The dotted line in Fig. 3.2 is the level of the EPF expected from Poisson noise. The measurements run into the Poisson noise for bin sizes less than ~ 70 s. With a bin size of 90 s the source is variable at greater than 3σ .

We searched further for indications of rapid variability by determining the shortest doubling times; that is, by searching for the shortest time interval in which the count rate doubles. Count rate doubling times on the order of 800 s were reported during the *ROSAT* observations and as low as 400 s during the *ASCA* observation. With this most recent *XMM-Newton* observation, numerous such events are found on time scales between 300 – 800 s, and the shortest measured doubling time is about 270 s.

Persistent variability

Clearly absent from the light curves are the giant and rapid flux outbursts that one has come to expect from IRAS 13224–3809 (Boller et al. 1993; Otani et al. 1996; Boller et al. 1997; Leighly 1999b). In the galaxy’s defence, long monitoring with *ROSAT* (Boller et al. 1997) suggests that such flaring events occur every few days; hence, were probably missed by this short (< 1 day) observation. However, short time binning of the light curve (< 100 s) reveals persistent variability.

With 60 s binning of the data, we searched for segments of quiescence in the light curve. Dividing the light curve into 10 minute segments, we used the χ^2 test to search

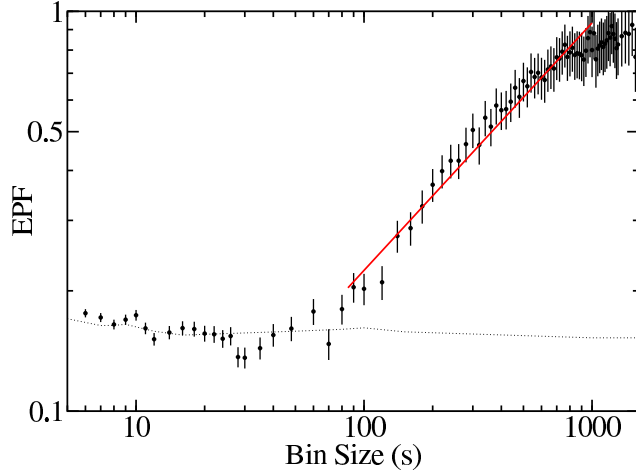


Figure 3.2: The EPF as a function of bin width calculated for IRAS 13224–3809. The dotted line is the estimated level of the EPF expected from Poisson noise. The faint, solid line is a power-law fit to the 85 – 1000 s (1.2×10^{-2} – 10^{-3} Hz) region, with a normalisation of $0.013^{+0.003}_{-0.002}$ and an index of 0.619 ± 0.036 . This measured index is related to the power-law index of the power spectrum (α), and consistent with $\alpha = -1.619$ (see Yaqoob et al. 1997 for a detailed explanation).

for global variability in each segment and found all of the segments to be variable at $> 3\sigma$ significance. In this manner, we worked our way through shorter time segments. Examining 9 minute segments we found that 101 of 103 segments were variable at $> 3\sigma$ significance (the other 2 segments were variable at $> 2.6\sigma$). The shortest segment size tested was 5 minutes, for which we determined that $\sim 62\%$ (115/187) of the segments showed variability at a significance level $> 2.6\sigma$. The variable segments do not appear to be associated with a particular flux state. About 65% of the high-flux segments and 57% of the low-flux segments displayed variability.

The persistent variability on such short time scales disfavors the idea that the variability is dominated by intrinsic disc instabilities, primarily because of the much longer time scales required for this process (Boller et al. 1997). This is, perhaps, in line with the lack of simultaneous UV fluctuations (as found in the OM light curve). Some AGN models predict that the UV and soft X-ray emission are the same physical process, namely thermal emission from the accretion disc (*Big Blue Bump*). Bearing this in mind, one would expect that the UV and soft X-rays should vary on similar time scales if the variability were due primarily to disc instabilities. Since this is not the case for IRAS 13224–3809 (in addition to the high thermal temperature derived in Chapter 2), there must be some other overriding process responsible for the rapid X-ray variability on time scales of minutes.

The persistent variability on such short time scales is also in contradiction with the

idea that the variability arises from a *single*, rotating hot spot on the disc. Furthermore, there are no detectable temperature changes in the soft spectrum, as would be expected due to beaming effects. However, the hot spot model cannot be dismissed as the cause of the large-amplitude fluctuations during flaring episodes. The persistent variability on time scales of minutes is most likely due to a combination of effects, and no one origin (e.g. disc instabilities, coronal flaring, hot spots) can be definitively ruled out.

Radiative efficiency

If we assume photon diffusion through a spherical mass of accreting matter we can estimate the radiative efficiency, η , from the expression $\eta \gtrsim 4.8 \times 10^{-43} (\Delta L / \Delta t)$ (Fabian 1979; see also Brandt et al. 1999 for a discussion of important caveats), where ΔL is the change in luminosity, and Δt is the time interval in the rest frame of the source. From both *ROSAT* (Boller et al. 1997) and *ASCA* (Otani et al. 1996) observations of IRAS 13224–3809, a radiative efficiency exceeding the maximum Schwarzschild black hole radiative efficiency ($\eta = 0.057$) was determined. It is tempting to attribute this result to accretion onto a Kerr black hole, or anisotropic emission, or X-ray hot spots on the disc.

We calculated the radiative efficiency at several points in the 200s binned 0.3 – 10 keV light curve. From the mean unabsorbed luminosity ($6 \times 10^{43} \text{ erg s}^{-1}$) and average count rate ($1.74 \pm 0.05 \text{ count s}^{-1}$) we were able to calculate a conversion factor between count rate and luminosity ($1 \text{ count s}^{-1} = 3.4 \times 10^{43} \text{ erg s}^{-1}$) and hence, calculate the luminosity rate of change from the observed change in count rate. Minimum and maximum count rates and times were averaged over at least two bins (ideally three). The regions selected correspond to the most rapid changes in count rate (either rising or falling), and they occupy various regions in the light curve (i.e. regions were selected in the high-, low-, and medium-flux states, as well as events transcending the different flux states).

The most rapid rate of change was $\Delta L / \Delta t = (4.10 \pm 0.91) \times 10^{40} \text{ erg s}^{-2}$ corresponding to a radiative efficiency of $\eta \gtrsim 0.020$. Averaging over all ten selected regions we determine an average radiative efficiency of $\eta \gtrsim 0.013$. No clear trend is seen between the value of η and the flux state of the object from which the measurement was made. Since the calculated η is a lower limit, our small value is not inconsistent with the η calculated from the *ROSAT* or *ASCA* observations; nevertheless, it is nearly a factor of 10 smaller, and we are clearly consistent with the efficiency regime of a Schwarzschild black hole. It would stand to reason that we do not necessarily have a Kerr black hole in IRAS 13224–3809 since radiative efficiency limits in excess of the Schwarzschild limit are only found in the *ROSAT* (Boller et al. 1997) and *ASCA* (Otani et al. 1996) observations during periods of giant flaring outbursts. The large values of η found in past observations are probably due to radiative boosting or anisotropic emission during the flaring events.

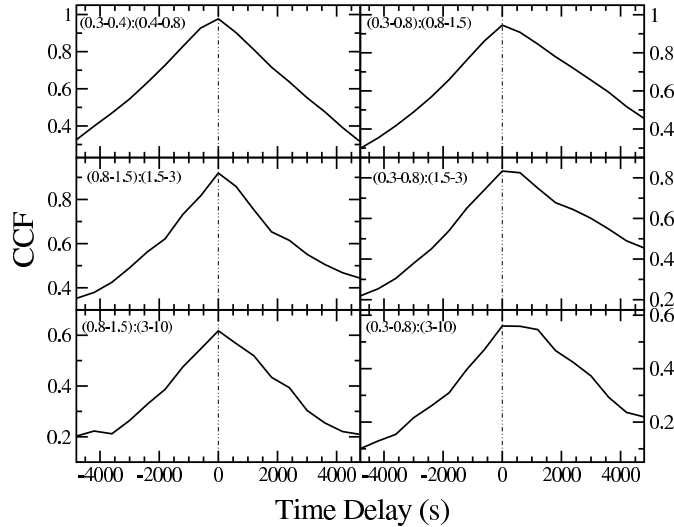


Figure 3.3: Six of the CCFs calculated from the light curves with 600 s binning. The energy bands being cross correlated are shown in the top left of each window. The calculations were conducted such that a positive shift in time would indicate a lag of the second energy band.

Correlations among the light curves

Several light curves in different energy bands were produced and compared with each other, and found to be correlated. The significance of the correlations were measured with the Spearman rank correlation coefficient (Press et al. 1992; Wall 1996). All of the light curves are well correlated with each other at $> 99.9\%$ confidence.

Given the variability in all the light curves, and the significant correlation amongst all of them, it was natural to search for leads and lags by calculating the cross correlation function (CCF).² We calculated CCFs between all the light curves and we present six of them in Fig. 3.3. Most of the cross correlations are symmetric with a peak corresponding to zero time delay. However, when the soft 0.3 – 0.8 keV band is cross correlated with harder energy bands (right column of Fig. 3.3), the CCFs become broad and somewhat flat-topped with a noticeable asymmetry toward longer lags. Because the time sampling is sufficiently fast to resolve the variations in the light curves, it is the width of the ACF that ultimately limits the resolution of the CCF. The soft light curve has a red power spectrum (a power-law fit to the power spectrum has an index of ~ -2 ; see Fig. 3.2), giving an ACF that is quite broad. The pronounced asymmetry of the CCF suggests we are barely resolving a lag between the two light curves. Using the *centroid* of the CCF yields a lag of the 3 – 10 keV band by 460 ± 175 s. The other two CCFs in the right column of Fig. 3.3 also reveal a slight asymmetry. The CCFs peak at a lag of zero, but the asymmetry suggests the hard bands lag the soft. The pronounced asymmetry of the 3 – 10 keV versus the

²When calculating cross correlation functions, all of the data were utilised to avoid dealing with gapped time series.

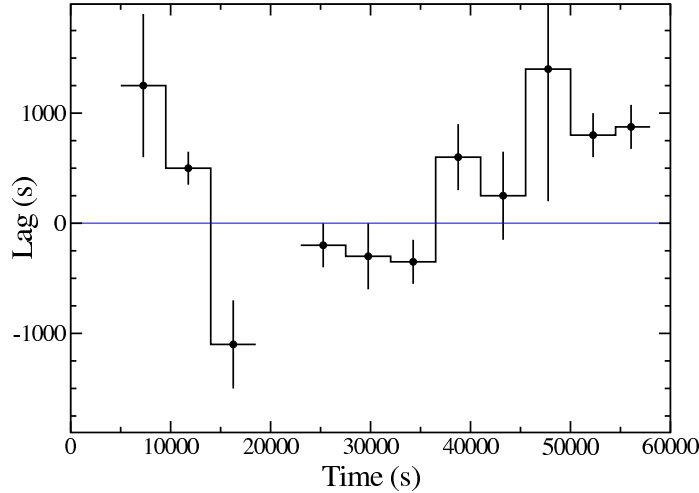


Figure 3.4: The lag measured between the 3 – 10 keV and 0.3 – 0.8 keV light curves, in 4500 s intervals, over the duration of the observation. The lag alternates in such a way that at times the soft band leads the hard (positive lag), and at other times, the hard leads the soft (negative lag). The time interval during which the background flare occurs has been omitted.

0.3 – 0.8 keV CCF warranted more attention.

Careful inspection of the light curves indicate that the hard X-rays do not always lag the soft; in some cases it appears that the reverse is true. To investigate further, we cut the soft and hard light curves into 12 segments, each 4500 s in duration with 50% overlap between them (so only every other segment is independent). We then computed the CCF in each of these shorter light curves. The results confirmed our visual suspicion — in some cases the hard X-rays lead the soft while at other times it lags. The results are shown in Fig. 3.4. The lags span approximately -1100 s to $+1400$ s and appear to be mildly correlated with the soft X-rays in the sense that when the soft X-rays are strong, the hard lags the soft. The lag is positive more often than negative in our light curves, explaining why the full CCFs show a slight positive lag. Error bars on the lags were determined via a Monte Carlo technique: 5000 simulated soft and hard light curves were generated by varying every observed datum according to a Gaussian distribution whose standard deviation was equal to the uncertainty in the observation. The CCF was computed for each light curve pair and the peak recorded. The width of the distribution of the 5000 peaks was used to estimate the uncertainty in the lag. This was repeated for each of the 12 light curve segments. The perceived lags and leads are likely due to a physical separation between the soft and hard emitting regions and/or reprocessing.

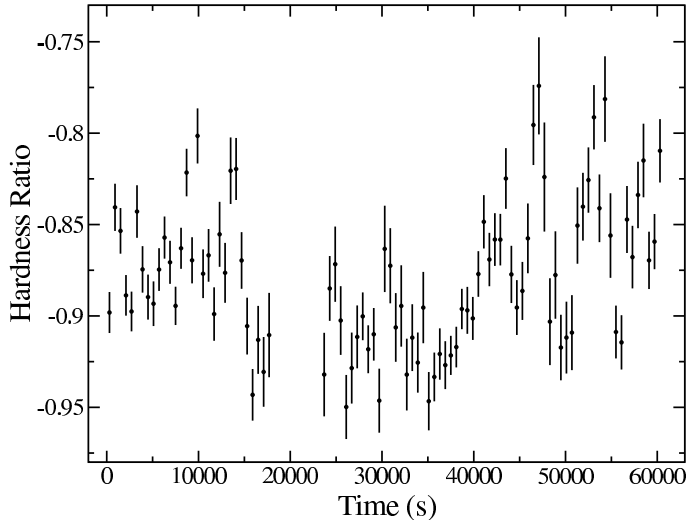


Figure 3.5: A typical hardness ratio variability curve. In this example $H = 1.5 - 10$ keV and $S = 0.3 - 1.5$ keV (see text for details). Zero seconds on the time axis marks the start of the observation at 03:15:02 on 2002-01-19. The region of high background flaring has been omitted.

3.4 Detection of significant and rapid spectral variability

From the available light curves we calculated seven hardness ratios by the definition $(H - S)/(H + S)$, where H and S are the count rates in the hard and soft bands, respectively. With this formalism, the value of the hardness ratio will be between -1 and $+1$, and the harder spectra will have more positive values. A typical hardness ratio is shown versus time in Fig. 3.5. In this case $H = 1.5 - 10$ keV and $S = 0.3 - 1.5$ keV. All seven ratios show similar time variability to the hardness ratio in Fig. 3.5, albeit, some with poorer signal-to-noise. In addition, each hardness ratio curve was tested for global variability via a χ^2 test. In all cases, the hardness ratios were inconsistent with a constant at greater than 2.6σ . The spectral variability depicted in Fig. 3.5 is significant and rapid. In addition, the variability appears to intensify after about 40 ks into the observation. With the multiple spectral components required in the spectral model, isolating the location of the spectral variability is challenging.

We notice in Fig. 3.1 that the overall trend in the count rate light curves is very similar between different energy bands; however, on closer inspection it becomes noticeable that the amplitude of the variations is different. To illustrate this observation better we produce normalised light curves in four energy bands, and in 10 ks bins (Fig. 3.6). It becomes clear with this manner of binning that the amplitude of the flux variations are different among the energy bands, and indeed, there does appear to be a significant increase in the $3 - 10$ keV flux after ~ 40 ks.

We searched for the source of the spectral variability further by calculating the fractional variability amplitude (F_{var}) following Edelson et al. (2002). The results are

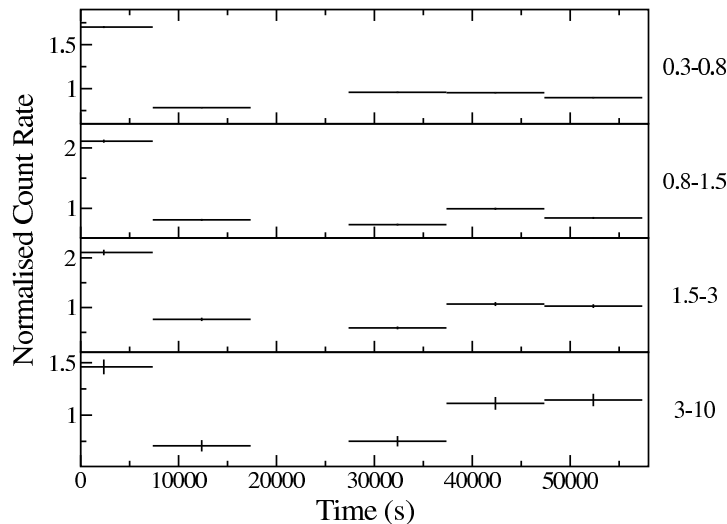


Figure 3.6: Four normalised X-ray light curves in various energy bands, and in 10 ks bins. After ~ 40 ks, the amplitude of the fluctuations becomes greater in the 3–10 keV band than in the softer energy bands. Note that although the count rate error bars are plotted, they are too small to see in some of the light curves.

shown in Fig. 3.7 using 200 s binning of the light curves. Most of the variability is observed between 0.8 and 2 keV. This region is quite complex as it includes the broad Fe L absorption feature, and the point where the blackbody and power-law components intersect (see Chapter 2); hence, it is difficult to isolate any one component.

A difference spectrum (high–low) also confirms the spectral variability. A power-law is a good fit to the difference spectrum over the 1.3–8 keV band.

3.4.1 Flux correlated spectral variability

Given the reasonable agreement in the appearance of the hardness ratios and the light curves we searched for common trends in hardness ratio versus count rate plots. Using the Spearman rank correlation coefficient to test for correlations, four of the hardness ratios were found to be correlated with the light curves at more than 99.5% confidence. These four hardness ratios are plotted against the count rate in Fig. 3.8. The four flux correlated hardness ratios are ($H:S$):

- (1) (3–10):(0.3–0.8),
- (2) (3–10):(1.5–3),
- (3) (0.8–1.5):(0.3–0.8),
- (4) (3–10):(0.8–1.5).

The count rates used are the summation of H and S .

As can be seen from Fig. 3.8, in four cases the spectral variability is correlated with the variability in the count rate. In three cases, spectral hardening was observed during periods of lower count rates. This general effect has been observed previously

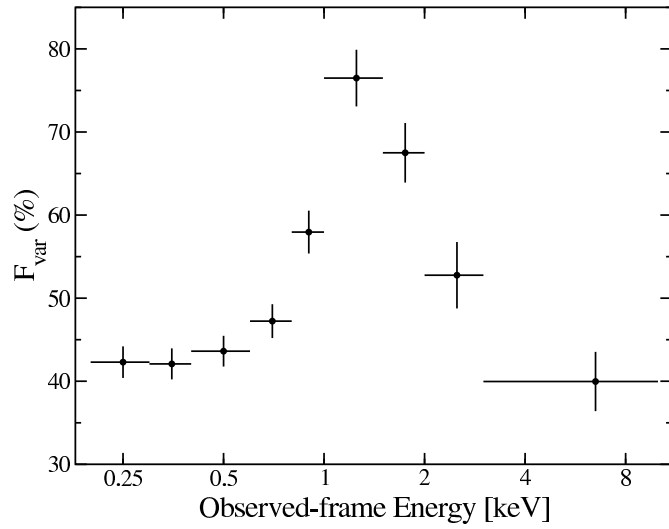


Figure 3.7: F_{var} calculated in nine energy bins between 0.2 and 10 keV. The light curves used were in bins of 200 s.

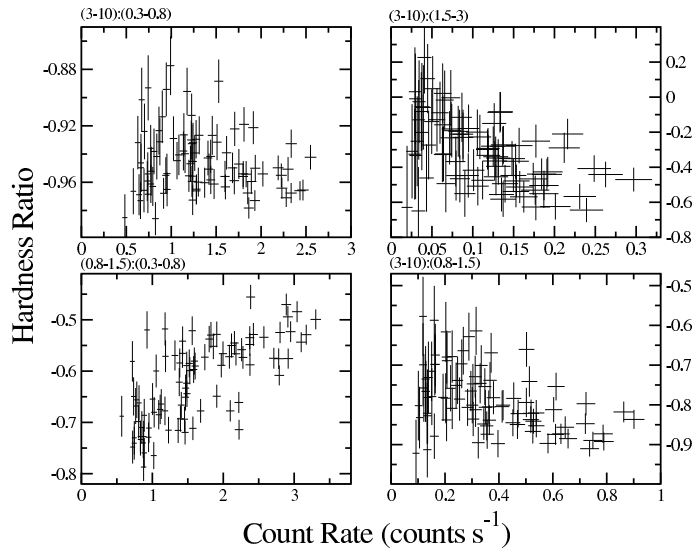


Figure 3.8: Four hardness ratios correlated with count rates. The bands used are show in the upper left of each panel. The count rates used are the summation of H and S .

Table 3.1: Comparison of the blackbody and power-law unabsorbed fluxes in the 0.8–1.5 keV band. Fluxes are in units of 10^{-13} erg cm $^{-2}$ s $^{-1}$. The associated uncertainty in the fluxes is derived from the uncertainty in the count rates, and it is shown in brackets. The fourth column is the ratio of power-law flux over blackbody flux (column 3/column 2).

Flux State	Blackbody Flux	Power-law Flux	Ratio
High	7.97(0.18)	5.00(0.11)	0.63
Medium	4.89(0.14)	2.41(0.07)	0.49
Low	2.95(0.20)	0.67(0.05)	0.23

in IRAS 13224–3809, as well as in other AGN, for example: MCG–6-30-15 (Lee et al. 2000), NGC 5548 (Chiang et al. 2000), 3C 273 (Turner et al. 1990), and NGC 7314 (Turner 1987). The trend is a more common feature among X-ray novae (see Tanaka & Shibazaki 1996). Such a trend is predicted by the partial covering model, and is further supported by the spectral analysis of IRAS 13224–3809 (Fig. 2.6). However, the hardness ratio (0.8–1.5):(0.3–0.8) (lower left panel of Fig. 3.8) shows the reverse effect – increased intensity when the spectrum is hard. Such a relation was also found in the radio-loud NLS1 PKS 0558–504 (Gliozzi et al. 2001). In that object, the hardening with increased flux was interpreted as an additional hard component due to a radio jet. This is probably not the case for IRAS 13224–3809 since it is radio-quiet and since the unusual hardness pattern is only observed over a small energy range. Since the 0.8 – 1.5 keV energy band is very complicated due to the comparable contributions from the thermal, power-law, and Fe L components, it is difficult to isolate or eliminate any one of these components. An alternative explanation for the observed trend is that each spectral component varies differently (or not at all) with changing flux. For example, the spectral variability in the Fe L could be independent of the flux. Similarly, the continuum in this band could also be independent of the flux changes and of the Fe L. However, when these possibly independent behaviors are combined, the trend presented in Fig. 3.8 (lower left panel) arises. A more likely picture is that the intrinsic power-law is more variable than the soft component. This is supported somewhat by Fig. 3.6, and we provide further evidence in support of this claim in Table 3.1. We modelled the 0.2 – 7 keV spectrum in various flux states (flux states are defined in Section 3.3). In Table 3.1 we show the unabsorbed fluxes of the power-law and blackbody components in the 0.8 – 1.5 keV band. It is clear that the power-law does in fact show larger amplitude variations in this energy band. While the difference between the blackbody flux in the low and high state is ~ 2.5 , the power-law flux changes by more than a factor of 7. This is most likely the cause for the trend observed in the lower left panel of Fig. 3.8.

3.4.2 A possible lag between flux variations and spectral variations

Further complexities arise when we scrutinize the 0.3–1.5 keV light curve and spectral variations in greater detail. We calculated the cross correlation function of the 0.3 –

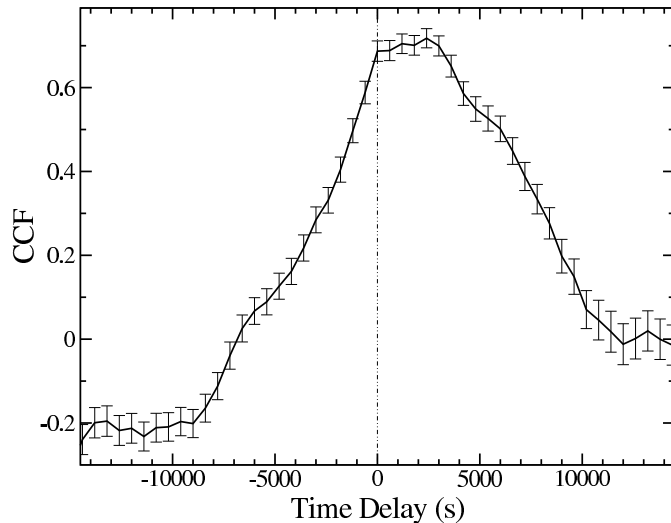


Figure 3.9: The cross correlation of the $H = 0.8 - 1.5$ keV and $S = 0.3 - 0.8$ keV light curve and hardness ratio variability curve. The CCF indicates a short delay between the two curves, such that, the hardness ratio curve lags behind the light curve.

1.5 keV light curve versus the 0.8 – 1.5 keV to 0.3 – 0.8 keV hardness ratio variability curve. The cross correlation is presented in Fig. 3.9, and indicates that the hardness ratio curve lags behind the light curve by 2000^{+1500}_{-2000} s. It is not clear whether this observation is supporting the reprocessing of soft photons idea, or indicating variability in the Fe L absorption feature, or some other effect.

Calculating light curve versus hardness ratio cross correlation functions for the other bands did not reveal any significant correlations. This could be an effect of the poorer signal-to-noise in those bands as opposed to some physical process. The band for which we have determined a lag is, perhaps not surprisingly, the highest signal-to-noise energy range.

3.5 Discussion

3.5.1 General findings

We have presented the timing properties of the NLS1 IRAS 13224–3809 from a 64 ks *XMM-Newton* observation. Our findings are summarized below.

- (1) As expected, persistent and rapid variability was prevalent, although no giant-amplitude variations were detected. The source was in a relatively high flux state compared to the *ROSAT* HRI observation.
- (2) Unlike previous *ROSAT* and *ASCA* observations, the radiative efficiency was below the limit for a Schwarzschild black hole.

- (3) Light curves in several bands were all well correlated. When any two light curves were cross correlated, most showed a symmetric correlation peaking at zero lag. However, when the time averaged 0.3 – 0.8 keV band was cross correlated with higher energy bands, an asymmetric cross correlation profile was found. Further inspection indicates that the lag varies — in some cases the hard X-rays lead, and at other times they lag.
- (4) Four of seven hardness ratio variability curves showed correlations with count rate fluctuations. Three of the four indicated spectral hardening at lower count rates, supporting the partial covering scenario. The fourth hardness ratio, (0.8–1.5):(0.3–0.8), was characterised by hardening at higher count rates, most probably due to a more variable power-law component.
- (5) The same hardness ratio, (0.8–1.5):(0.3–0.8), also shows a possible time delay compared to the light curve; thus, suggesting flux induced spectral variability.

3.5.2 Reprocessing scenario

The basic idea in many AGN models is that high-energy emission is produced in the accretion disc corona by Comptonisation of soft photons, which are likely thermal in nature. The detected positive lags (soft leads hard) in Fig. 3.3 and 3.4, could be indicative of such a process. In this situation the time lag would be due to either a physical separation between the two emitting regions, or the reprocessing rate in the corona, or, most likely, a combination of the two. On the other hand, we also see evidence of the hard emission leading the soft (Fig. 3.4 and 3.6), which could be occurring if high-energy coronal photons are irradiating the disc and being Compton scattered. In this case, the perceived lag would most probably be due to a physical separation between the emitting regions, since the reprocessing rate is likely short due to the high densities in the disc. Interesting is the fact that the apparent leads and lags are alternating, indicating that both processes are occurring simultaneously but only one is dominating at a given time.

3.5.3 Future tests for the partial covering and disc-line models

The partial covering model (Holt et al. 1980; Boller et al. 2002; Tanaka et al. 2004) is a very good fit to the spectrum in Chapter 2. The fit can adequately describe the sharp spectral feature at 8.1 keV, and the absence of the Fe line expected from the fluorescent yield, all with a reasonable Fe overabundance. The panels in Fig. 3.8 which demonstrate spectral hardening during states of lower intensity are fully consistent with the partial covering scenario. Observations of the intensity recovering above the edge, and the detection of other edges (e.g. Ni spectroscopy), would validate the partial covering scenario in IRAS 13224–3809.

The disc-line model (Fabian et al. 2002) also provided a good fit across the whole energy band to the data in Chapter 2, and without requiring extra absorption (albeit, with a large equivalent width for the broad Fe line). Such a model is not inconsistent

with the observed flux and spectral variability in IRAS 13224–3809, nor is it inconsistent with the interpretation that the asymmetric cross correlation functions are a result of reprocessing of soft energy photons. We could test for the presence of the Fe line by measuring the depth of the edge feature at ~ 8.1 keV in various flux or temporal states. The overwhelming strength of the proposed line suggests that the variations we have detected probably arise within the line. Therefore, one would expect that as the line profile changes so would the depth of the edge. A constant edge depth would be inconsistent with the disc-line interpretation. With the current photon statistics it is not possible to conduct such a test precisely.

In general, much of the timing behavior can be described in the context of the partial covering phenomenon, with intrinsic source variability being a secondary effect. The variability behavior of IRAS 13224–3809 suggests a complicated combination of effects which we have started to disentangle in this present analysis. A much longer observation with *XMM-Newton*, including the detection of a giant outburst event, would allow us to answer several of the questions raised during this most recent X-ray observation.

Chapter 4

Long-term spectral changes in the partial-covering candidate NLS1 1H 0707–495

4.1 Introduction

The first observation of the Narrow-Line Seyfert 1 galaxy (NLS1) 1H 0707–495 ($z = 0.0411$) with *XMM-Newton* in October 2000 revealed a sharp spectral feature at ~ 7 keV in which the spectrum “jumped” by a factor of > 2 within a few hundred eV (Boller et al. 2002; hereafter B02). The measured energy and sharpness of the feature implied K-absorption by neutral iron; however, the absence of a fluorescence line suggested a more complicated situation. These observations coupled with the low intrinsic absorption below ~ 1 keV led B02 to consider a partial covering model (Holt et al. 1980) to interpret the X-ray spectrum. Although a good fit was obtained, the model required a steep intrinsic power-law ($\Gamma = 3.5$) and an iron overabundance of > 35 times solar.

In an alternative approach, Fabian et al. (2002) treated the spectrum as being dominated by a reflection component, where the deep edge was interpreted as the blue wing of a relativistically broadened iron line. This model was also successful in describing the 0.5 – 11 keV spectrum (including the soft-emission component), and required a more modest iron overabundance of 5 – 7 times solar.

A second attempt at fitting the spectrum with a partial covering model was made by Tanaka et al. (2004; hereafter T04). They demonstrated that a partial covering model, implementing a cutoff power-law (rather than a simple power-law), greatly reduced the iron abundance to ≈ 5 times solar.

Three months following the *XMM-Newton* observation, 1H 0707–495 was observed with *Chandra* (Leighly et al. 2002; hereafter L02). The flux was found to be about 10 times higher than what was measured with *XMM-Newton*. A preliminary investigation found that the edge feature was weak, possibly even absent, during the *Chandra* observation.

1H 0707–495 was observed with *XMM-Newton* for a second time two years after

the first observation. In this paper we will focus on the differences between the two *XMM-Newton* observations, and attempt to explain them in the context of the partial covering phenomenon. A reflection interpretation is also possible, and is investigated further in Chapter 5.

4.2 Observations and data reduction

The second *XMM-Newton* observation of 1H 0707–495 occurred on 2002 October 13 during revolution 0521 (hereafter this observation will be referred to as AO2). The total duration was 80 ks, during which time all instruments were functioning normally. The observation was carried out identically to the first Guaranteed Time observation during revolution 0118 (hereafter referred to as GT). The EPIC cameras were operated in full-frame mode and utilised the medium filter.

The Observation Data Files (ODFs) from the GT and AO2 observations were processed to produce calibrated event lists using the *XMM-Newton* Science Analysis System (SAS v5.4.1). Unwanted hot, dead, or flickering pixels were removed as were events due to electronic noise. Event energies were corrected for charge-transfer inefficiencies. EPIC response matrices were generated using the SAS tasks ARFGEN and RMFGEN. Light curves were extracted from these event lists to search for periods of high background flaring. A background flare was detected during the first few ks of the AO2 observation, and the data have been ignored during this interval. The total amount of good exposure time selected was 70 ks and 78 ks for the pn and MOS detectors, respectively. Source photons were extracted from a circular region 35" across and centred on the source. The background photons were extracted from an off-source region and appropriately scaled to the source selection region. Single and double events were selected for the pn detector, and single-quadruple events were selected for the MOS. The total number of source counts collected in the 0.3 – 10 keV range by the pn, MOS1, and MOS2 were 275451, 46284, and 46426, respectively. Comparing the source and background spectra we found that the spectra are source dominated below 10 keV.

High-resolution spectra were obtained with the Reflection Grating Spectrometers (RGS). The RGS were operated in standard Spectro+Q mode, and collected data for a total of 76 ks. The first-order RGS spectra were extracted using the SAS task RGSPROC, and the response matrices were generated using RGSRMFGEN. The RGS data were background dominated during the GT observation.

4.3 The AO2 spectral and timing analysis

4.3.1 Spectral analysis

The source spectra were grouped such that each bin contained at least 40 counts. Spectral fitting was performed using XSPEC v11.2.0 (Arnaud 1996). Fit parameters are reported in the rest frame of the object. The quoted errors on the model parameters

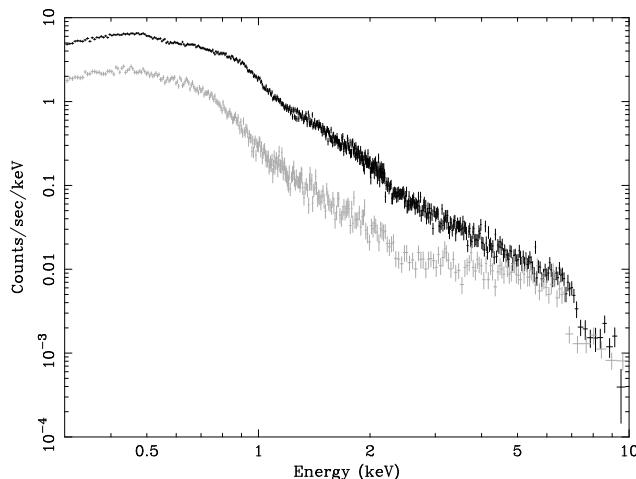


Figure 4.1: The 0.3 – 10 keV AO2 (black data points) and GT (gray data points) pn data separated by about two years.

correspond to a 90% confidence level for one interesting parameter (i.e. a $\Delta\chi^2 = 2.7$ criterion). The Galactic column density toward 1H 0707–495 is $N_{\text{H}} = 5.8 \times 10^{20} \text{ cm}^{-2}$ (Dickey & Lockman 1990). Element abundances from Anders & Grevesse (1989) are used throughout. Luminosities are derived assuming isotropic emission and a standard cosmology with $H_0 = 70 \text{ km s}^{-1} \text{ Mpc}^{-1}$, $\Omega_M = 0.3$, and $\Omega_\Lambda = 0.7$.

While both the pn and MOS data from each observation were examined for consistency, the discussion focuses on the pn results due to the higher signal-to-noise and the better stability of the pn calibration over the two years separating the observations.

Figure 4.1 gives a direct comparison between the GT and AO2 time-averaged spectra. In general, the count rate below $\sim 5 \text{ keV}$ is higher during the AO2 observation; however, between 5–10 keV the fluxes are comparable. The flattening of the spectrum above $\sim 2 \text{ keV}$, seen in the GT data, is clearly diminished in the AO2 data. The depth (τ) and energy (E) of the edge-like feature at $\sim 7 \text{ keV}$ have changed.

Fitting a power-law and edge to the 3 – 10 keV AO2 data resulted in a good fit ($\chi^2 = 126/122 \text{ dof}$), with the edge parameters $E = 7.49 \pm 0.10 \text{ keV}$ and $\tau = 0.84_{-0.22}^{+0.25}$. The edge was also sharp, with an intrinsic width $< 160 \text{ eV}$ [measured with the SMEDGE (Ebisawa 1991) model in XSPEC]. Treating the $\sim 7.5 \text{ keV}$ drop as a blueshifted neutral edge, we would expect neutral iron emission at $\sim 6.7 \text{ keV}$. However, the best-fit line ($E \approx 6.74 \text{ keV}$) was broad ($\sigma \approx 229 \text{ eV}$) and only a marginal improvement to the edge fit ($\Delta\chi^2 = 6$ for 3 additional free parameters). The broadness of the line is problematic, as it would be expected that the line be narrower than the edge.

The 90% upper limit on the line flux is $1.08 \times 10^{-14} \text{ erg cm}^{-2} \text{ s}^{-1}$, whereas the flux absorbed by the edge is $8.49 \times 10^{-14} \text{ erg cm}^{-2} \text{ s}^{-1}$, resulting in a line-to-edge flux ratio of 0.13. For a spherically symmetric distribution of absorbing material, the expected line-to-edge flux ratio is approximately equal to the fluorescent yield for iron (0.34; Bambynek et al. 1972). Therefore, for 1H 0707–495 the expected ratio is more than 2.5 times the measured value, and the discrepancy is even larger if the edge and line

are assumed to arise from ionised iron (Krolik & Kallman 1987). The measured line-to-edge flux ratio indicates that the absorber covers a solid angle $\Omega/4\pi \lesssim 0.4$.

When applying to the AO2 data the partial covering model used by T04 to interpret the GT observation, it was found that the two data sets were very similar. The 2 – 10 keV spectrum could be fitted with a cutoff power-law ($\Gamma \approx 2$, $E_{cut} \approx 5$ keV), modified by an absorber with an iron overabundance of ~ 5 times solar, consistent with what was used to model the GT data. The primary difference was that the AO2 model only required one absorber, which was equivalent to setting the covering fraction of the second absorber, used on the GT data, to zero. The reduced amount of absorption could simultaneously explain the apparently steeper spectrum and the shallower edge seen in the AO2 data. Indeed, the intrinsic, unabsorbed 2 – 10 keV spectra from the two observations were entirely consistent, with a flux difference of only a factor of ~ 2 . The edge was found at a higher energy (7.5 ± 0.1 keV) during the AO2 observation, and this will be discussed at length in Section 4.4. The use of the power-law with a low cutoff energy is simply empirical. Allowing for curvature in the high-energy spectrum greatly reduces the iron abundances.

Considering the broad-band (0.3 – 10 keV) spectrum, a multi-coloured disc black-body component (MCD; Mitsuda et al. 1984; Makishima et al. 1986) was included to fit the soft-excess below ~ 1.5 keV.

In treating the intrinsic absorption in the GT data, T04 found that including an edge at 0.37 keV (0.39 keV rest frame) was an improvement over using only neutral absorption. It was uncertain if the edge was required due to calibration uncertainties or if it was due to intrinsic C v absorption in 1H 0707–495. In order to make the most direct comparison with the earlier observation we also included an edge at 0.37 keV, in addition to Galactic and intrinsic cold absorption. All model parameters for the AO2 fit are given in Table 4.1.

While the continuum model of an intrinsically absorbed MCD and cutoff power-law modified by partial covering provided a good fit to the high- and low-energy spectra, the fit was inadequate in the 0.5 – 2 keV range ($\chi^2 = 1340/569$ dof). The AO2 continuum appeared to be modified by line-like absorption and emission. Fits using only one Gaussian profile (either an absorption or emission line) were unsuccessful, as were attempts to fit the data with an absorption edge. Two distinct Gaussian profiles, one absorption and one emission, were required. An absorption profile with an equivalent width of $EW \approx -50$ eV, an energy of $E \approx 1.17$ keV, and a width of $\sigma \approx 115$ eV, as well as an emission profile with $EW \approx 25$ eV, $E \approx 0.92$ keV, and $\sigma \approx 50$ eV, were included in the broad-band fit ($\Delta\chi^2 = 684$ for 6 addition free parameters).

The RGS spectra are of low signal-to-noise, but confirmed the existence of the absorption feature detected in the pn. The improvement to the partial covering continuum, by the addition of the Gaussian absorption profile was $\Delta\chi^2 = 231$ for 3 additional free parameters. The line energy and width was $E = 1.19_{-0.11}^{+0.02}$ keV and $\sigma = 245_{-32}^{+133}$ eV, respectively. No strong emission features were prominent in the RGS spectra at approximately 0.92 keV (only one RGS is effective in this energy range); however there was indication of a skewed excess at a slightly lower energy which could

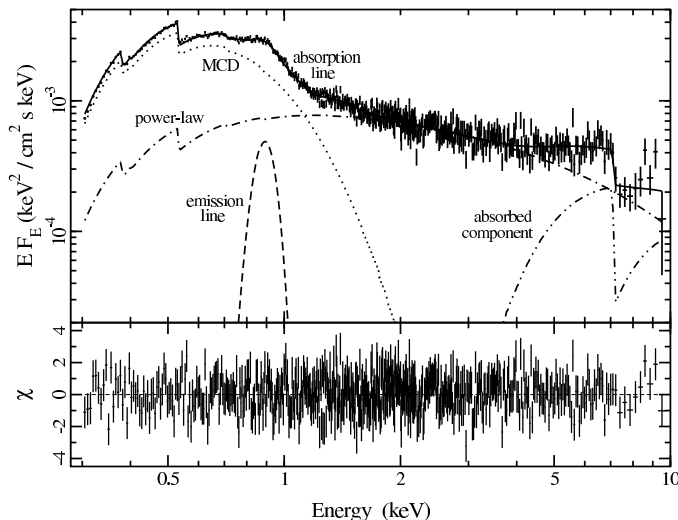


Figure 4.2: The best-fit partial covering model fitted to the AO2 EPIC pn data. In the upper panel we present the unfolded model with the individual components marked. The fit residuals (in terms of sigma) are shown in the lower panel.

be consistent with the EPIC findings. The absence of a convincing emission feature in the RGS is probably a result of the poorer signal-to-noise, since the feature was detected in all three EPIC instruments, as well as the earlier *Chandra* observation (L02).

The complete partial covering model applied to the EPIC pn AO2 data is presented in Fig. 4.2 ($\chi^2 = 656/563$ dof), and the fit parameters are given in Table 4.1. The 0.3 – 10 keV flux and luminosity, corrected for Galactic absorption, are 1.1×10^{-11} erg cm $^{-2}$ s $^{-1}$ and 4.4×10^{43} erg s $^{-1}$, respectively. The 2 – 10 keV luminosity is 4.7×10^{42} erg s $^{-1}$.

4.3.2 Timing analysis

The 0.3 – 12 keV pn light curve from the GT and AO2 are presented in Fig. 4.3. The average count rate was about three times higher during AO2 than it was during the GT observation. Count rate variations by about a factor of four were seen throughout both observations. The persistent and rapid variability is quite typical of 1H 0707-495 (Leighly 1999).

During the GT observation, 1H 0707-495 displayed no significant spectral variability. Hardness ratio curves showed some variability (Figure 5 of B02), but they were uncorrelated with flux. The fractional variability amplitude F_{var} , (Edelson et al. 2002), was calculated at both epochs in the 0.3 – 12 keV bands to examine the degree of variability in each band. There was no significant spectral variability during the GT observation (left panel of Fig. 4.4); however, the rms spectrum portrayed substantially

Table 4.1: Model parameters for the partial-covering fit to the pn data ($\chi^2 = 656/563$ dof). Superscript f indicates that the parameter is fixed. Fluxes (F) are given in units of $\text{erg cm}^{-2} \text{s}^{-1}$ and have been corrected for Galactic absorption.

Low-Energy Absorption			
Galactic ^{f}	$5.8 \times 10^{20} \text{ cm}^{-2}$		
Intrinsic (cold)	$(1.6 \pm 0.2) \times 10^{20} \text{ cm}^{-2}$		
Intrinsic (edge)	$E^f = 0.37 \text{ keV}$	$\tau = 0.37 \pm 0.05$	
Continuum			
MCD	$kT = 155 \pm 1 \text{ eV}$		$F = 1.00 \times 10^{-11}$
Cutoff power-law	$\Gamma = 2.0 \pm 0.1$	$E_{cut} = 4.5_{-0.7}^{+0.9} \text{ keV}$	$F = 4.11 \times 10^{-12}$
Partial Coverer			
Absorption	$N_{\text{H}} = 43_{-19}^{+14} \times 10^{22} \text{ cm}^{-2}$		
Fe abundance	$3_{-1}^{+7} \times \text{solar}$		
Covering fraction	0.69 ± 0.01		
Line Features			
Emission	$E = 921 \pm 10 \text{ eV}$	$\sigma = 50 \pm 13 \text{ eV}$	$EW \approx 25 \text{ eV}$
Absorption	$E = 1.17_{-0.04}^{+0.02} \text{ keV}$	$\sigma = 114_{-17}^{+29} \text{ eV}$	$EW \approx -50 \text{ eV}$

more spectral variability during the AO2 observation (data points in right panel of Fig. 4.4).

The AO2 F_{var} appears similar to the rms spectrum from the high-flux state *Chandra* observation (L02), as well as to the rms spectrum of some broad-line Seyfert 1s, such as NGC 4151 (Zdziarski et al. 2002). In addition, it is notably similar to the F_{var} spectrum of another partial covering candidate NLS1, IRAS 13224–3809 (Fig. 3.7).

Fabian et al. (2004a) modelled the AO2 rms spectrum shown in Fig. 4.4, and demonstrated that it could be well-fitted as the superposition of two components with different intrinsic rms: a variable power-law (in flux only), and a less variable reflection component.

The energy-dependent variability can also be explained within the partial covering scenario. For a finite extension of the emission region, the covering condition can be more complex than described by a single absorber with parameters f (covering fraction) and N_{H} (column density in units of 10^{22} cm^{-2}). As a better approximation we assume two partial coverers (double partial covering; see T04 and Equation 1.9), and then model the high-flux ($> 5 \text{ counts s}^{-1}$) and low-flux ($< 3 \text{ counts s}^{-1}$) spectra simultaneously for a common intrinsic spectrum (e.g. see Fig. 2.6). The high- and low-flux spectra are grouped with bins containing at least 40 and 20 counts, respectively. All model parameters of the high- and low-flux spectra are linked, and only the covering fraction (f) of each absorber is allowed to vary independently. The model gives a satisfactory fit ($\chi^2 = 770.9/683$ dof). The covering parameters of the two absorbers (f, N_{H}) are determined to be (0.61, 36.0) and (0.46, 0.21) in the high-flux state, and (0.80, 36.0) and (0.0, 0.21) in the low-flux state. In Fig. 4.4 (right panel) we show the

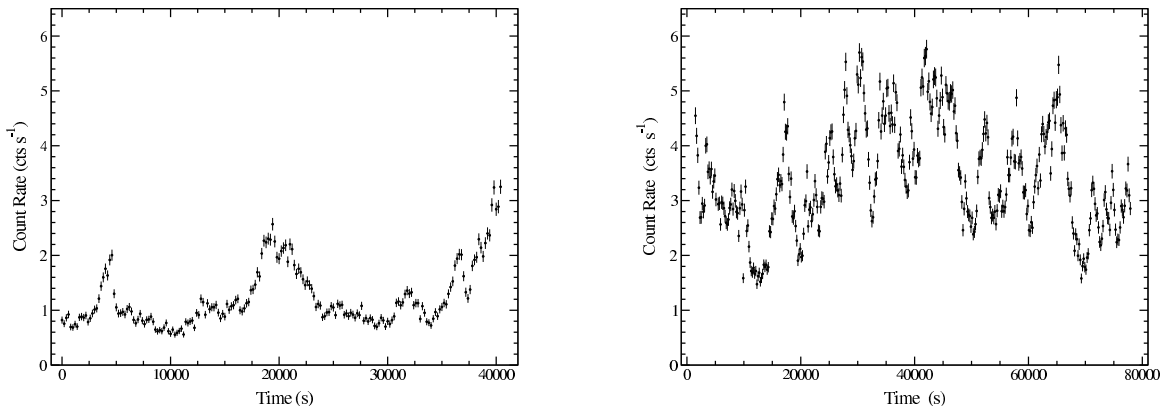


Figure 4.3: The GT (left panel) and AO2 (right panel) pn light curve in the 0.2 – 12 keV band. The count rate scale is identical on both graphs to ease the comparison. Bin sizes are 200 s.

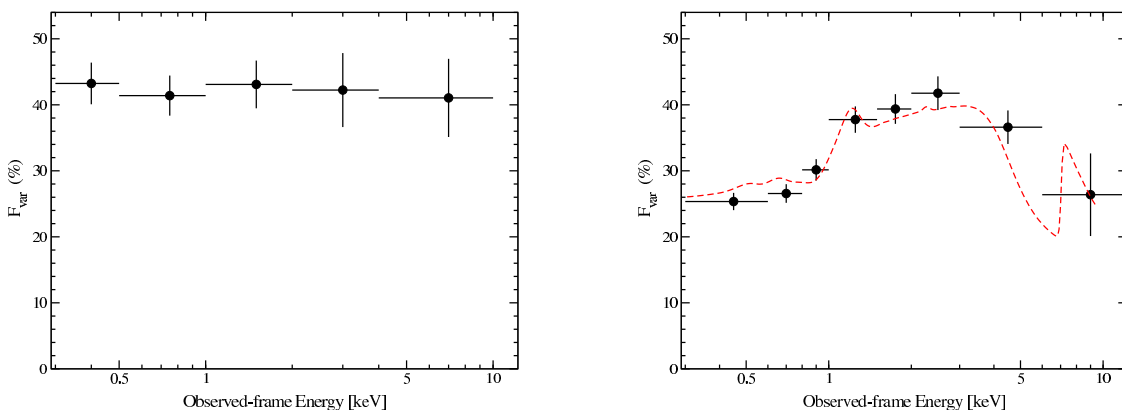


Figure 4.4: The GT (left panel) and AO2 (right panel) F_{var} calculated in the 0.3 – 12 keV band, using 400 s binning of the light curves (data points). The F_{var} scale is identical on both graphs to ease the comparison. Overplotted on the AO2 rms spectrum is the ratio of the high- and low-flux spectral models (red, dashed line).

ratio (high/low) of the two models (dashed-line) overplotted on the rms spectrum. A double partial covering can reproduce the energy-dependent variations in shape and amplitude.

4.4 Discussion

4.4.1 A shifting edge and relativistic outflows

Perhaps the most interesting changes between the two observations are the differences in the edge parameters (Fig. 4.5). During the GT observation the edge energy was $E = 7.0 \pm 0.1$ keV, entirely consistent with neutral iron. At the second epoch the edge energy was considerably higher, $E = 7.5 \pm 0.1$ keV. In addition, the edge depth

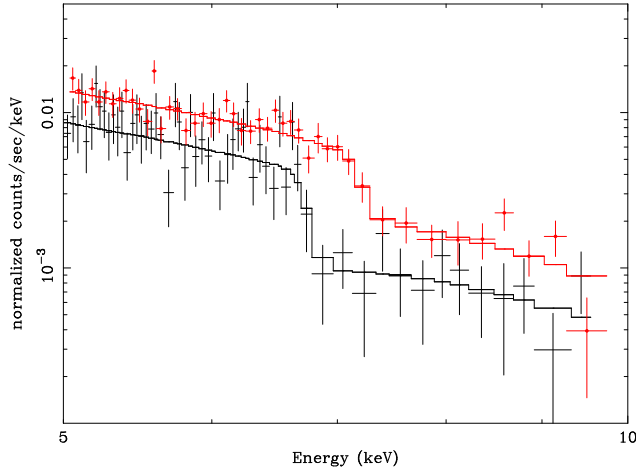


Figure 4.5: The edge plus power-law fitted to the AO2 (top curve; red dots) and GT (bottom curve; black crosses) pn data. The edge energy and depth are clearly different; however, the edge width remains comparable (and narrow).

during AO2 was approximately half as deep as it was during the first observation. The intrinsic edge widths were narrow at both epochs. The 90% confidence upper-limits on the intrinsic edge widths were 350 eV and 160 eV during the GT and AO2 observation, respectively. If we continue to adopt the iron edge interpretation for the second observation, the edge energy corresponds to absorption by Fe VII–X.

Two scenarios emerge as possible explanations for the differing edge energies: (1) a change in the ionisation state, or (2) a high-speed outflow.

While a change in the ionisation state due to a change in the ionising continuum is plausible, the drawback is that the sharpness of the edge is narrow in both observations. Palmeri et al. (2002) discuss two distinct spectral features of the Fe K-edge which seem relevant here. Firstly, a sharp edge is only expected in low-ionisation plasmas [$\xi = (L/nR^2) \lesssim 10$ (cgs units are hereafter assumed), where L is the incident X-ray luminosity, n is the gas density, and R is the distance from the radiation source], in which case the edge energy would be consistent with neutral iron within the available resolution. Secondly, for higher ionisation plasmas ($\xi \gtrsim 1$), a strong absorption feature appears at about 7.2 keV, arising from the $K\beta$ unresolved transition array (UTA). Even within our uncertainties, we can dismiss absorption features below ~ 7.3 keV; therefore a photoionisation interpretation for the shifting edge seems unlikely.

On the other hand, if the edge arises from a neutral absorber, the observed energy implies an approaching velocity of $(0.05 \pm 0.01)c$. This interpretation is consistent with the edge width remaining constant over the two year span. In the context of the partial covering phenomenon, assuming that new absorbers are not being generated, the outflowing material would result in a decrease of the covering fraction, and subsequently a decrease in the edge depth as the absorbers cover a smaller solid angle. Both effects, a shallower edge and reduced absorption, are observed in the AO2 data. Evidence for an outflow was also seen in the *HST* spectrum of 1H 0707–495 (Leighly

2004), although not at such high velocities. An equally sharp feature in IRAS 13224–3809 (Chapter 2) was found at 8.2 ± 0.1 keV. The outflow scenario was also suggested in that case.

Considering a patchy-absorber model, and following, for example, Turner et al. (1993), Reynolds (1997) and Ogle et al. (2004), the mass loss rate can be estimated by combining the continuity equation $\dot{M} = 4\pi R^2 f_v n m_p v$ (where f_v is the volume-filling factor and n the atomic density) with the expression for the ionisation parameter to obtain $\dot{M} = 4\pi f_v (L/\xi) m_p v$. For $v = 0.05c$, ionising luminosity $L = 5 \times 10^{43}$ erg s $^{-1}$ and $\xi \lesssim 1$, this gives $\dot{M} \gtrsim 10^4 (f_v/\xi) M_\odot \text{ yr}^{-1}$ and a kinetic luminosity $L_w \gtrsim 10^{48} (f_v/\xi)$ erg s $^{-1}$. The mass accretion rate estimated in TO4, assuming a slim-disk (see Section 4.4.2) and their estimated mass, is $\dot{M}_{acc} \approx 0.1 M_\odot \text{ yr}^{-1}$. For the outflow rate to be consistent with the mass accretion rate, $f_v/\xi < 5 \times 10^{-6}$ (cgs) is required, i.e. the absorber is extremely clumped. A clumped medium is also the simplest way to reduce the mass flux (Krolik et al. 1985).

Inserting the value of L into $\xi = L/nR^2$ gives $nR^2 = 5 \times 10^{43}/\xi$ (cgs), where R is the distance to the absorber. For simplicity, we assume spherical “blobs” of radius r , which are randomly distributed. The covering fraction obtained from the fit shows that the average number of intersecting blobs in the line-of-sight is approximately two (Tanaka, Ueda & Boller 2003). Using the column density estimated from the fit, $4nr = 4 \times 10^{23}$ cm $^{-2}$, we get $R^2/r = 5 \times 10^{20}/\xi$ cm. The mean free path of an ionising photon is given by $l = 4r/3f_v$. Since $R > 2l$; $R^2/r > 8R/3f_v$, we obtain $R < 2 \times 10^{20} (f_v/\xi) \sim 10^{15}$ cm, and $r < 2 \times 10^9 \xi$ cm. These values are not inconsistent with those estimated from the time scale of variability (TO4). The atomic density is very high, $n > 5 \times 10^{13}/\xi$ cm $^{-3}$. Such blobs would need to be confined by magnetic fields (e.g. Rees 1987).

4.4.2 The low-energy spectrum

At both epochs, the low-energy continuum is dominated by a thermal component which can be successfully fitted with a MCD. The inner-disc temperature is noticeably higher ($\sim 50\%$) during AO2 ($kT_{AO2} \approx 155$ eV, $kT_{GT} \approx 103$ eV).

In addition, a strong ‘P Cygni type’ feature is also observed during AO2 (Fig. 4.6). The profile is likely coincidental and unrelated to the outflow scenario since there is no evidence of P Cygni type profiles in the RGS.

An extended warm medium

Qualitatively, the P Cygni type feature is similar to that detected during the *Chandra* observation of 1H 0707–495. In a preliminary investigation L02 determined that the feature was best described when both emission and absorption were considered. We have also treated the feature as a blended absorption and emission profile from a warm medium.

Similar absorption features have been observed in other NLS1. Nicastro, Fiore & Matt (1999) suggest that such absorption features are likely a blend of resonance

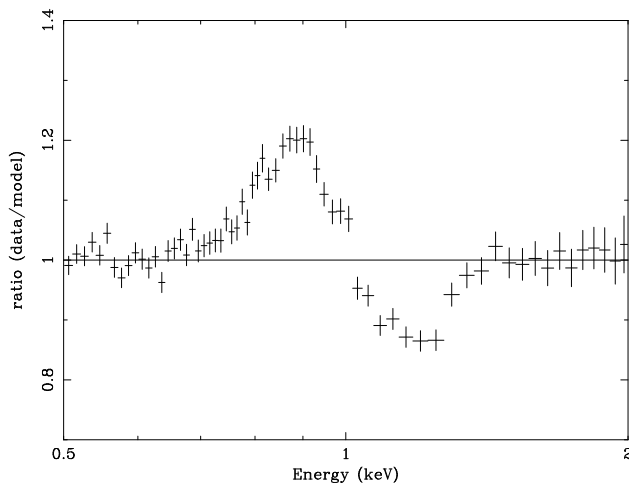


Figure 4.6: Spectral complexity in the low-energy spectrum. The residuals (data/model) remaining between 0.5 – 2 keV after the AO2 pn spectrum is fitted with a MCD plus power-law model (see text for details).

absorption lines due to mostly ionised L-shell iron. Interestingly, IRAS 13224–3809, another partial covering NLS1 candidate, also displays a similar absorption feature (Fig. 2.4).

The emission feature can be explained as arising from an extended warm medium, at lower ionisation, and lying outside the line-of-sight. In addition to the *Chandra* observation, similar emission features have been observed in the NLS1: NGC 4051 during its low-flux state (Uttley et al. 2003), and Mrk 1239 (Grupe et al. 2004). For both objects, the authors attributed the emission to ionised Fe and/or Ne. In a thorough investigation of the low-state RGS spectra of NGC 4051 Pounds et al. (2004) identified emission features around 900 eV as arising from Ne IX and the radiative recombination continua from O VIII. Detailed simulations of high-resolution data are still required to address the exact nature of this feature in 1H 0707–495.

The emission/absorption feature was not detected during the low-flux GT observation (B02; Fabian et al. 2002; T04). Simulations of the pn data using the AO2 model and a 40 ks exposure time (consistent with the GT exposure time) indicated that both the emission and absorption features should have been significantly detected during the shorter GT observation, if they were present. Furthermore, an absorption feature was detected in the *ASCA* observations of 1H 0707–495 (Leighly et al. 1997; Leighly 1999; Vaughan et al. 1999) when the flux was comparable to the AO2 flux. Indications are that these warm features are time variable, at least on time scales of months, and possibly related to the luminosity of 1H 0707–495 in such a way that the features are present during higher-luminosity states.

Slim-disc considerations

If the low-energy continuum is due to disc emission, then the measured temperature is too high for a standard accretion disc (discussed in Chapter 1). It was shown in T04 that the intrinsic bolometric luminosity during the GT observation was near the Eddington limit for an estimated mass of $\sim 2 \times 10^6 M_{\odot}$. During the AO2 observation the intrinsic luminosity was approximately a factor of two higher. In these luminosity regimes ($L_{bol} \approx 1 - 2L_{edd}$) the slim-disc model, first proposed by Abramowicz et al. (1988), is applicable.

Mineshige et al. (2000) adopted the slim-disc model to describe the disc emission and variability in a sample of NLS1, including 1H 0707–495. A key element of the slim-disc approximation is that the temperature-luminosity relation is steeper when $L_{bol} \approx L_{edd}$, than it is in the standard disc case (e.g. Mineshige et al. 2000; Watarai et al. 2001). This can explain the observed increase in temperature against a moderate increase in luminosity.

A significant increase in the accretion rate resulting in higher luminosities could potentially explain the long-term variability seen in a warm medium supposedly located light-months away.

4.4.3 Short-term spectral variability

The rms spectrum during the GT observation showed no significant spectral variability. The explanation for this is rather straightforward in terms of partial covering (e.g. T04). If the soft and hard emission regions are equally covered by the absorber then little spectral variability is expected. The AO2 spectral variability is much more complex; however, it can still be described in the context of partial covering if we adopt a double partial covering (see T04 and Equation 1.9). A similar picture can probably be drawn for the spectral variability in IRAS 13224–3809 (Chapter 2 and 3). Admittedly, a second absorber does introduce additional parameters into the fit, but considering the possible complexity of partial covering in reality, a double coverer is probably a better description of the physical processes involved than a single absorber is.

4.4.4 Comments on previous X-ray observations of 1H 0707–495

As indicated by its name, 1H 0707–495 was identified as a *HEAO-1* source. Remillard et al. (1986) reported a 2–10 keV flux of $2.4 \times 10^{-11} \text{ erg cm}^{-2} \text{ s}^{-1}$, a factor of ~ 20 higher than the AO2 observation, and more than 50 times higher than the GT observation. Clearly, source confusion was a consideration with this mission, and it is possible that not all of the *HEAO-1* flux is attributed to 1H 0707–495. However, Remillard et al. had good reasons against a false detection, and no new information has surfaced to strongly question the identification (R. Remillard 2004, private communication).

About three months after the first *XMM-Newton* observation of 1H 0707–495, it was observed with *Chandra*. A preliminary analysis by L02 showed that the flux of 1H 0707–495 had dramatically increased by nearly a factor of 10. Interestingly,

L02 found that a ~ 7 keV edge was not statistically required by the data. The 90% upper-limit on the edge depth was $\tau < 0.8$.

In principle (and barring detailed analyses), these earlier observations could be understood in the context of partial covering. The *HEAO-1* flux is high (assuming it was all attributed to 1H 0707–495), but it is comparable to the intrinsic value estimated by T04; thus it could be achieved with a near “minimum” in the covering fraction of the absorber. As with the AO2 observation, the *Chandra* observation showing a diminished (possibly absent) edge and higher flux could also arise from a reduction in the covering fraction.

4.5 Conclusions

Two *XMM-Newton* observations of 1H 0707–495 separated by more than two years are examined and compared. Our findings are as follow:

- (1) The edge energy and depth are significantly different, while the intrinsic edge width remains consistently narrow (< 300 eV). Between the two observations, the edge energy has shifted from ~ 7.0 keV to ~ 7.5 keV, and the edge depth has diminished by $> 50\%$.
- (2) Emission and absorption lines are detected in the low-energy spectrum indicating the presence of an extended warm medium.
- (3) The temperature of the MCD component used to model the soft-excess is much higher during the AO2 observation ($kT_{AO2} \approx 155$ eV) compared to the GT observation ($kT_{GT} \approx 103$ eV).
- (4) The flux variability during GT and AO2 is typical of what has been seen in 1H 0707–495 previously. There was also strong spectral variability during AO2 which was not observed during the GT observation.

The X-ray spectrum of 1H 0707–495 appears remarkably different over the span of two years, showing apparent changes in the spectral slope, as well as changes in the edge characteristics. We have demonstrated that the primary X-ray source (the power-law emitter) is not required to undergo any physical changes during this time; rather the differences can be explained simply by changes in a line-of-sight absorber associated with the partial covering phenomenon. The changes in the disc temperature, line-like features at low energies, energy-dependent time variability, and shift in the edge energy may be related to an increase of the intrinsic luminosity. The energy-dependent time variability can be explained assuming two separate absorbers (there could be a range of absorbers). The shift of the edge energy is a challenge since it requires that the absorber is extremely clumpy.

Further observations of 1H 0707–495 in various flux states should be able to distinguish between the partial covering and reflection models.

Chapter 5

X-ray reflection in 1H 0707–495

5.1 Introduction

An alternative explanation for the sharp spectral drop in 1H 0707–495 is enhanced reflection in the X-ray spectrum (see Section 1.5). A reflection dominated spectrum was discussed in detail by Fabian et al. (2002b) for the GT observation of 1H 0707–495. A corrugated disc was invoked to account for the X-ray reflection dominating the observed emission. The continuum source was assumed to be mostly hidden from direct view in a corrugation, but its reflection observable from the walls. If the reflecting material is the inner parts of an accretion disc then the reflection spectrum is blurred by Doppler and gravitational redshift effects. The sharp 7 keV drop in 1H 0707–495 is then the blue edge of the relativistically-blurred iron emission line. The shift in edge energy during the second *XMM-Newton* observation can then be due to a change in ionisation or geometry of the irradiated material.

Gravitational light bending is another alternative which naturally produces reflection-dominated and relativistically blurred spectra during low flux states. An important prediction of the model is that reflection is correlated with the power-law continuum only at very low flux levels, while at higher fluxes it is almost constant despite large continuum variability.

In this Chapter, the light bending model is applied to the AO2 observation of 1H 0707–495 to investigate whether reflection-dominated emission can account for the entire *XMM-Newton* spectrum and its variations.

5.2 An emission line in the spectrum of 1H 0707–495?

A power-law was fitted to the 1.5 – 2 keV and 7.5 – 12 keV data. The residuals from this fit over the 0.3 – 12 keV band is shown in Fig. 5.1. A large skewed emission-like feature, similar to that found in MCG–6-30-15 (Tanaka et al. 1995; Fabian et al. 2002a; see Fig. 1.7) is evident between about 4–7 keV, and a steep soft-excess is found below 1 keV. The data between 1.5 – 12 keV were then modelled with a power-law and a relativistic emission line (Laor 1991). A good fit was obtained ($\chi^2 = 365/334$

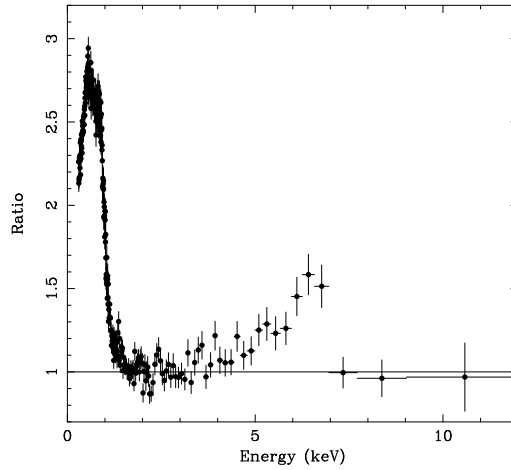


Figure 5.1: Ratio of the XMM-Newton pn spectrum of 1H 0707-495 to the power-law which fits best between 1.5 – 2 keV and 7.5 – 12 keV. A broad iron line and a steep soft-excess are evident. Data have been rebinned for visual clarity.

dof) with $\Gamma = 2.8$. Notice that no extreme inclination was required to reproduce the spectral drop ($i \simeq 40 - 50^\circ$). The strength of the line was $EW \approx 1.8$ keV, and its rest frame energy was $E \approx 6.7$ keV implying that ionised reflection need to be considered. The reflection continuum is then complicated (see Fig. 1.5) and needs to be modelled properly.

5.3 Reflection dominated spectra

Ionised reflection models (Ross & Fabian 1993) were fitted to the entire 0.3 – 12 keV observable band. Reasonable agreement was obtained (Fig. 5.2; $\chi^2 = 760/575$ dof) with a model which was relativistically blurred, had 3 times solar abundance, and a photon index $\Gamma = 3$ (which is the maximum in the available grid). The ionisation parameter of the reflection model was $\log \xi = 2.8$ (cgs). This was not as good a fit as was obtained with the partial covering model in Chapter 4 ($\chi^2 = 656/563$ dof), but that model had five separate components (apart from cold absorption) operating on different parts of the spectrum. In contrast, the reflection model has only two components (power-law and reflection), both of which are broad-band. In Fig. 5.3, the (blurred) reflection plus power-law model used to describe the data in Fig. 5.2 is presented.

The intrinsic unblurred reflection spectrum is shown in Fig. 5.4. A large iron K emission line and edge dominate the spectrum around 7 keV and a steep soft-excess occurs below 1 keV. The bump in the blurred spectrum just below 1 keV, modelled as a Gaussian emission line in the partial covering model (Chapter 4), is due to a complex of iron-L lines.

The relativistic blurring is accomplished using a Kerr kernel (Laor 1991) with a radial emissivity index of $q \simeq 5.1$ (where the emissivity has the radial dependence r^{-q})

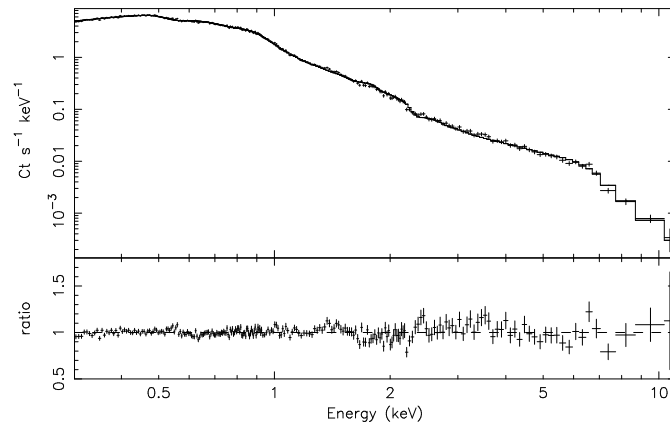


Figure 5.2: The best-fitting (blurred) ionised reflection plus power-law model plotted on the spectrum of 1H 0707-495. Simple photoelectric absorption has also been applied. The model fits the data reasonably well over the entire observed energy band. Data have been rebinned for visual clarity.

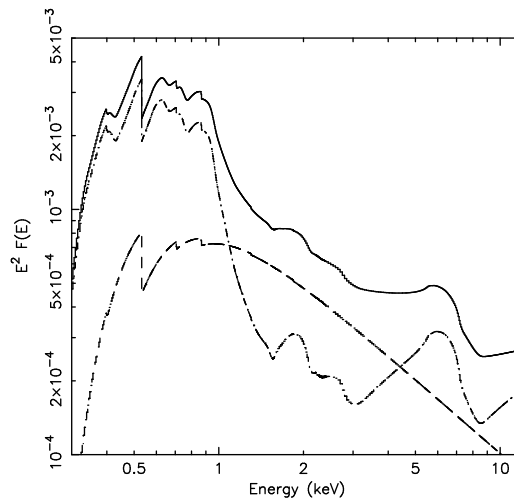


Figure 5.3: The (blurred) ionised reflection plus power-law model used in the fit shown in Fig. 5.2.

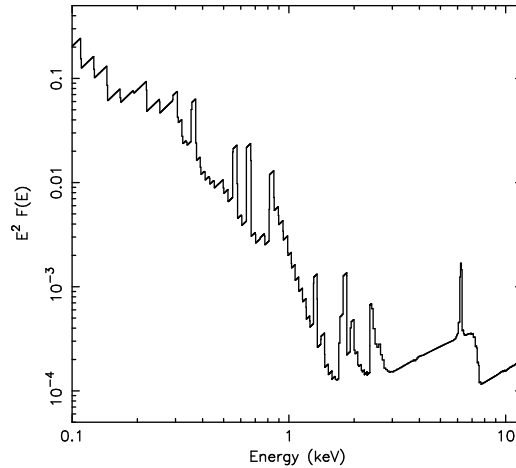


Figure 5.4: The unblurred best-fitting reflection model. The abundances are 3 times solar and $\xi = 10^{2.8}$. The irradiated gas is assumed to be of constant density with no intrinsic emission.

from $r_{\text{in}} \simeq 2.25$ to $r_{\text{out}} = 100$ gravitational radii, and disc inclination of $i \simeq 50^\circ$. The disc inclination is different from that obtained in the previously published analysis of the GT observation ($i < 30^\circ$, see Fabian et al. 2002b). This will be discussed in Section 5.4.

Models with higher abundances improve on the fit of the second (AO2) observation. At 7 times solar abundances the drop is sharper, but emission below about 0.7 keV is overproduced. This is probably a result of overestimating the oxygen abundance. The data appear to require a high iron abundance, but smaller oxygen abundance. A more extensive grid of reflection models with variable element abundances is required to pursue this issue further (and may also reduce the low-energy residuals in the present analysis). A range of ionisation parameters may also be needed to match the range of disc radii, so leading to a highly multi-parameter solution.

5.4 Comparison between the GT and AO2 observations

During the first GT observation of 1H 0707–495 the count rate was significantly lower than during the AO2 observation (see Fig.4.1 and 4.3). In both observation a spectral flattening above ~ 3 keV is evident and according to the interpretation here, it is related to the presence of a reflection component including a broad iron emission line. The most remarkable difference between the two observations is the drop energy. When modelled by a simple edge, it shifted from $E \simeq 7$ keV in the GT observation to $E \simeq 7.5$ keV in the AO2 observation. Moreover, the edge depth is considerably smaller during the higher flux AO2 observation, while it remains narrow at both epochs (Fig. 4.5).

The reflection-dominated model for the GT observation (Fabian et al. 2002b) was described by multiple reflectors (all components being blurred), and no power-law

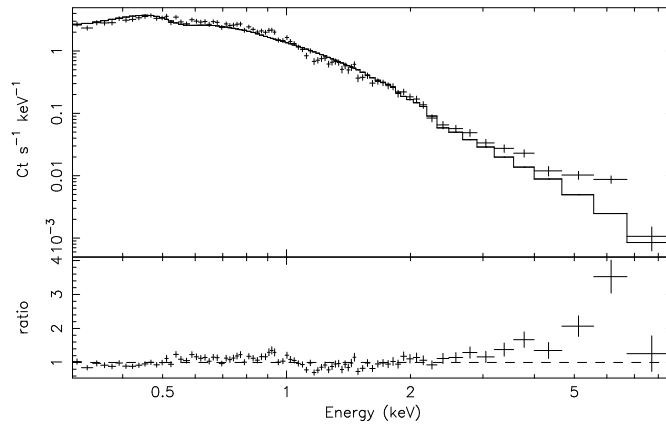


Figure 5.5: The difference spectrum, made by subtracting the high- and low-flux spectra, with the best fitting power-law plus cold absorption model.

continuum. The broad-band spectrum was completely dominated by reflection. The presence of different reflection components with different ionisation parameters most likely reproduces the radial distribution of ionisation on the disc, and does not allow easy derivation of the average ionisation state; however, a value of $\log \xi \approx 2$ seems to be a reasonable estimate for the GT observation. During the AO2 observation, $\log \xi = 2.8$ is measured.

The best-fit model for the GT observation was obtained by fixing the emissivity index of the relativistic blurring model to $q = 3$ and the disc inclination was derived to be about 20° . The inclination measured here is approximately 50° and seems to contradict the GT analysis. However, re-fitting the best-fit model of Fabian et al. (2002b) for the GT observation while allowing the emissivity index free to vary, results in a common solution for the two observations with inclination $\sim 50^\circ$. The new fit for the GT observation is of the same statistical quality of that presented in Fabian et al. (2002b) with $\chi^2 = 288/303$ dof. The main difference between the two observations is that the emissivity index is much steeper during the GT ($q \simeq 7$) than during the AO2 observation ($q \simeq 5$). A flatter emissivity profile reduces the effect of gravitational redshift on the sharp reflection features (emission lines and edges) so that the ~ 7 keV edge seen during the GT is observed at slightly higher energy during the AO2. Therefore, it is a combination of a higher ionisation parameter and flatter emissivity profile that is responsible for the edge energy shift. As mentioned, the other major difference between the two observations is that the spectrum is completely dominated by reflection during the GT observation, while a power-law continuum becomes visible during the AO2 (compare Fig. 5.3 with Figure 5 of Fabian et al. 2002b).

5.4.1 Source variability

1H 0707-495 varied dramatically during the second *XMM-Newton* observation. Spec-

tra were obtained when the source exceeded $4.5 \text{ counts s}^{-1}$ and when it was less than $3.5 \text{ counts s}^{-1}$ (see Fig. 4.3 for the broad-band light curve). The difference between them is shown in Fig. 5.5 when fitted with a power-law and cold absorption. It is close to a power-law of photon index 3.5, but shows a bump at iron-K energies. The source is therefore not identical in behaviour to MCG-6-30-15 where a difference spectrum mostly shows the power-law component (Fabian et al. 2002). In 1H 0707-495 the reflection component must vary too. In particular, since a bump is seen in the 4–7 keV band, the broad iron line must be stronger at high-flux states than at low fluxes. We have fitted the high- and low-flux spectra separately allowing only the normalisations of the power-law and reflection components to vary. Good fits ($\chi^2_\nu \simeq 1$) were found for both. The reflection normalisation changes by a factor of 1.7 while the power-law by a factor of 2.8 (a factor ≈ 1.6 between the two). The variability is dominated by changes in the flux of the power-law continuum, but the reflection component also varies.

As shown in Fig. 4.4, the fractional variability amplitude (F_{var}) during the AO2 observation is larger (again, by about a factor ≈ 1.6) in the intermediate band ($\sim 1 - 5 \text{ keV}$) than it is in the soft and hard bands. Moreover, F_{var} is roughly the same in the soft and hard bands where, according to the spectral analysis discussed here, ionised reflection dominates (Fig. 5.3). Therefore, in the reflection-dominated model, the energy dependent variability is easily understood. The 1–5 keV band is dominated by the power-law continuum which contributes the most to the source variability. The soft and hard bands do exhibit the same F_{var} because they are both dominated by ionised reflection from the accretion disc, which is less variable than the power-law continuum. During the first *XMM-Newton* observation of 1H 0707-495, the F_{var} was constant (Fig. 4.4). The analysis of Fabian et al. (2002b) strongly suggests a completely reflection-dominated spectrum during the GT observation. The constant F_{var} is then the result of a dominant broad-band spectral component in the overall 0.3–12 keV spectrum (i.e. ionised reflection from the disc), or if a weak power-law is present, it varies with the same amplitude as the reflection component.

5.5 Discussion

Remarkably, a relativistically blurred reflection-dominated model gives a reasonable fit to the new *XMM-Newton* spectrum of 1H 0707-495 over the entire observed energy band. The parameters are similar to those of MCG-6-30-15 (Fabian et al. 2002) and NGC 4051 (Uttley et al. 2004) in their low-flux states, but with a steeper photon index.

The results are consistent with fits to the earlier GT data (Boller et al. 2002; Fabian et al. 2002b), except that the photon index of the illuminating power-law was slightly flatter with $\Gamma \sim 2.5$, rather than $\Gamma \sim 3$ as measured here. The edge energy shifted from 7 keV to 7.5 keV in two years. The shift is not principally due to a change in ionisation state, although the best fits do show an increase in $\log \xi$ from 2 to 2.8. The energy of the iron line actually remains consistent with the helium-like emission, but the emissivity index is larger during the GT than it was during the AO2 observation. The higher emissivity index emphasises the inner radii of the disc, consequently increasing

the effects of gravitational redshifting, and shifting the line to lower energies (thus the drop at lower energies during the GT).

Several NLS1 objects with the strongest soft-excess exhibit an apparent absorption feature near 1 keV (e.g. Leighly 1999). The model proposed here for 1H 0707–495 requires no absorption feature in the 1–1.5 keV band (as it does in the partial covering model), but has instead line emission just below 1 keV. Therefore, it is possible that the spectra of other NLS1 can be explained by ionised reflection as well.

Strong gravitational light bending (Section 1.5) can explain the behaviour of 1H 0707–495 and possibly other NLS1, as discussed by Miniutti & Fabian (2004). The model predicts that in the lowest flux state, when the continuum source is closest to the centre of the disc, the power-law contribution is depressed and a reflection component which is relativistically blurred with steep emissivity profile is produced. Multiple reflection associated with returning radiation, or modelling a radial profile of the ionisation parameter, may provide the most interesting spectral parameterisation (Ross, Fabian & Ballantyne 2002). The observed rapid variability can be associated with changes in height of the continuum source above the black hole. This produces a correlation between the reflection component and the power-law component at low fluxes (e.g. the GT observation). At higher fluxes (AO2 observation), the model predicts a variable power-law component and an almost constant reflection component.

The fractional variability amplitude behaviour in both the first and second *XMM-Newton* observations, as well as the flux-flux plots analysis discussed in Fabian et al. (2004) support the light bending interpretation. The flux-flux plot analysis (Fabian et al. 2004) demonstrated that during the AO2 observation the spectral variability could be understood in terms of a variable component (e.g. the power-law), and a less variable component (e.g. the reflection), in excellent agreement with the light bending model. The observed rms spectrum is very well reproduced by this simple model (see Figure 9 of Fabian et al. 2004).

As pointed out by Miniutti & Fabian (2004) the inner disc emission is preferentially beamed along the equatorial plane thus illuminating the outer regions of the disc. This low velocity, high density material would then produce intermediate- and low-ionisation emission lines which are observed as narrow, as opposed to the blueshifted, broad high-ionisation lines likely produced in a lower density and high velocity wind (Leighly & Moore 2004; Leighly 2004a). The high-ionisation lines then appear predominantly blueshifted since the disc itself prevents us from seeing the outflow on the other side. Since the disc emission (here ionised reflection) has a very steep spectral shape and peaks below 1 keV, only a minor fraction is available for iron fluorescence above 7 keV. The associated narrow iron line is therefore weak and, if present, would be difficult to detect above the level of the much stronger inner disc emission dominated by the broad line in the 5–7.5 keV band.

The results indicate that the emission from 1H 0707–495, and likely other NLS1, originates within a few (10 or so) gravitational radii of the black hole. NLS1 may be among the best sources with which to probe the extreme gravity around the black hole.

Chapter 6

The prototype narrow-line quasar I Zw 1: Low-energy spectral complexity, iron lines, and hard X-ray flares

6.1 Introduction

Aside from being the prototype Narrow-Line Seyfert 1 galaxy (NLS1), I Zw 1 is an important object having influence in many areas of AGN astronomy. Its strong and narrow optical/UV emission lines minimise blending effects and allow I Zw 1 to be used as a template for optical (Boroson & Green 1992) and UV (Vestergaard & Wilkes 2001; Laor et al. 1997) Fe II emission. Taking its luminosity into consideration ($M_B \sim -23.5$; Schmidt & Green 1983), I Zw 1 is also defined as a quasar, likely making it the nearest quasar known ($z = 0.0611$). Although its infrared luminosity falls just short of those of Ultraluminous Infrared galaxies (ULIRGs), I Zw 1 exhibits properties of both QSOs and ULIRGs, and hence Canalizo & Stockton (2001) consider it as a possible transition object from QSO to ULIRG. Scharwächter et al. (2003; see also Eckart et al. 2000) used VLT observations to examine the host properties of I Zw 1. They observed an interacting spiral galaxy with a young stellar population in the disc as well as young, hot stars, and supergiants in the bulge, which is indicative of strong starburst activity.

At X-ray energies, I Zw 1 displays many of the characteristics typically associated with NLS1. *ROSAT* observations (Boller et al. 1996; Lawrence et al. 1997) found a steep 0.1 – 2.4 keV spectrum, described by a power-law of photon index ~ 3 , and notable variability (change by a factor of 1.5 in ~ 6000 s). However, Leighly (1999a) found that an absorbed power-law, without a soft-excess, was sufficient to fit the 0.5 – 10 keV *ASCA* continuum. In addition, Leighly detected a very strong ($EW \approx 1300$ eV) Fe K α line (see also Reeves & Turner 2000), which suggested a nucleus-wide overabundance of iron in I Zw 1.

In this Chapter we present a 20 ks *XMM-Newton* observation of I Zw 1. We begin by describing the observation and the data reduction in the next section. Section 6.3 is devoted to the results from the Optical Monitor. In Section 6.4 we discuss the X-ray spectra observed with the EPIC. In Section 6.5 we concentrate on the timing

properties. Lastly, in Section 6.6, we will conclude with a summary of our results.

6.2 Observation and data reduction

I Zw 1 was observed with *XMM-Newton* (Jansen et al. 2001) on 2002 June 22 during revolution 0464 for about 20 ks. During this time all instruments were functioning normally. The EPIC pn camera (Strüder et al. 2001) was operated in large-window mode, and the two MOS cameras (MOS1 and MOS2; Turner et al. 2001) were operated in small-window mode. All of the EPIC cameras used the medium filter. The two Reflection Grating Spectrometers (RGS1 and RGS2; den Herder et al. 2001) and the Optical Monitor (OM; Mason et al. 2001) also gathered data during this time. The Observation Data Files (ODFs) were processed to produce calibrated event lists using the *XMM-Newton* Science Analysis System (SAS v5.4.1). Unwanted hot, dead, or flickering pixels were removed as were events due to electronic noise. Event energies were corrected for charge-transfer losses. EPIC response matrices were generated using the SAS tasks ARFGEN and RMFGEN. Light curves were extracted from these event lists to search for periods of high background flaring. A short (lasting < 300 s), small-amplitude flare (equivalent to less than 3% of the source count rate) was detected about 9.5 ks into the observation. The data for this time period were ignored during the analysis. The total amount of good exposure time selected was 18650 s and 21006 s for the pn and MOS detectors, respectively. The source plus background photons were extracted from a circular region with a radius of $35''$, and the background was selected from an off-source region and appropriately scaled to the source region. Single and double events were selected for the pn detector, and single-quadruple events were selected for the MOS. The statistics were clearly dominated by the source at energies below 10 keV. The total numbers of good counts collected by the pn, MOS1, and MOS2 instruments were 137840, 45581, and 46829, respectively. The *XMM-Newton* observation provides a substantial improvement in spectral quality over the 28.3 ks exposure (92.4 ks duration) *ASCA* observation in which ≈ 12000 counts were collected (Leighly 1999b).

High-resolution spectra were obtained with the RGS. The RGS were operated in standard Spectro+Q mode for a total exposure time of 20713 s. The first-order RGS spectra were extracted using RGSPROC, and the response matrices were generated using RGSRMFGEN.

The Optical Monitor collected data through the *UVW2* filter (1800 – 2250 Å) for about the first 9 ks of the observation, and then it was switched to grism mode for the remaining time.

6.3 UV analysis

The Optical Monitor collected data in the fast mode through the *UVW2* filter (1800 – 2250 Å) for about the first half of the observation. The rest frame wavelength range observed through the *UVW2* filter is roughly 1700 – 2120 Å. Besides continuum emission,

Laor et al. (1997) attributed much of the emission in this spectral region to Fe II and Fe III multiplets. There is also some strong emission from Al III, and semi-forbidden species of Si III], C III], and N III].

In total, five photometric images were taken, each exposure lasting 1660s. The apparent *UVW2* magnitude is 14.36 ± 0.04 corresponding to a flux density of $9.94 \times 10^{-15} \text{ erg cm}^{-2} \text{ s}^{-1} \text{ \AA}^{-1}$ which is about a factor of three lower than during the 1994 *HST* observation (Laor et al. 1997). The approximately 2.5-hour light curve is flat with the exception of one data point which exhibits a 1σ deviation from the average. We do not consider this event significant.

Taking advantage of the simultaneous UV/X-ray observations, we derive the nominal spectral slope, α_{ox} , between 2500 Å and 2keV. For the UV flux, we use the peak response of the *UVW2* filter (2000 Å in the rest frame). We note from the *HST* spectrum, that the flux density at 2000 Å is approximately equal to the flux density at 2500 Å (Laor et al. 1997). By assuming a negligible continuum slope between 2000 – 2500 Å we are able to extrapolate the *UVW2* flux at 2000 Å to 2500 Å. For the model dependent X-ray flux (see Section 6.4) we used only the EPIC data which were collected simultaneously with the UV data (i.e. the first 10ks of the observation). We determine a value of $\alpha_{ox} = 1.20$ which is notably X-ray stronger than the value of 1.41 reported by Lawrence et al. (1997), and 1.56 reported by Brandt et al. (2000).¹ The spectral index between 2500 Å and 2 keV is clearly variable with time, but always appears X-ray strong compared to the predicted value for radio-quiet quasars of this luminosity (Vignali et al. 2003).

6.4 X-ray spectral analysis

The source spectra were grouped such that each bin contained at least 40 counts. Spectral fitting was performed using XSPEC v11.2.0 (Arnaud 1996). Fit parameters are reported in the rest frame of the object, although the figures remain in the observed-frame. The quoted errors on the model parameters correspond to a 90% confidence level for one interesting parameter (i.e. a $\Delta\chi^2 = 2.7$ criterion), and luminosities are derived assuming isotropic emission. The Galactic column density toward I Zw 1 is $N_H = 5.07 \times 10^{20} \text{ cm}^2$ (Elvis et al. 1989). A value of the Hubble constant of $H_0 = 70 \text{ km s}^{-1} \text{ Mpc}^{-1}$ and a standard cosmology with $\Omega_M = 0.3$ and $\Omega_\Lambda = 0.7$ have been adopted throughout.

Initially all three EPIC spectra were fitted separately to examine any discrepancies. The 3 – 10keV spectra were first fitted with a single power-law modified by Galactic absorption. The pn and MOS2 are entirely consistent; the photon indices for the pn and MOS2 fits are $2.26^{+0.05}_{-0.06}$ and 2.18 ± 0.10 , respectively. However, the MOS1 photon index is much flatter ($\Gamma_{MOS1} = 1.95 \pm 0.10$) and does not lie within the 90% confidence range of the other EPIC instruments. This inconsistency in the MOS1 data was

¹Brandt et al. (2000) use a reference point of 3000 Å for the UV flux. It is also worth noting that at 3000 Å there is a relatively strong Fe III multiplet emission that will make I Zw 1 appear X-ray *weaker* than if we were to consider only the continuum.

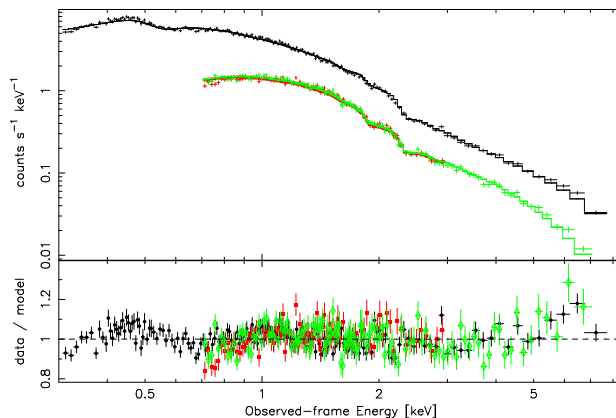


Figure 6.1: In the upper panel we present an absorbed power-law fitted to the EPIC 0.3 – 10 keV data. The top curve is the pn data and the data points in the bottom curve are the MOS1 and MOS2 data. In the lower panel are the residuals (data/model) of the power-law fit. Black circles, red squares, and green diamonds are the pn, MOS1, and MOS2 residuals, respectively. The data have been highly binned for display purposes only.

previously realised in an observation of 3C 273 by Molendi & Sembay (2003). Molendi & Sembay noted a difference in the MOS1 photon index compared to the other EPIC photon indices of $\Delta\Gamma \sim 0.1$. The difference in our observation is larger ($0.13 < \Delta\Gamma < 0.31$). However, the pn data dominate the fits above 3 keV given the higher statistics afforded by this instrument. Including the 3 – 10 keV MOS1 data has little influence on the model results. For clarity, the figures are shown without the 3 – 10 keV MOS1 data, but the fit statistics will include all of the data. Cross-calibration uncertainties between pn and MOS appeared quite significant in our observation at energies below ~ 0.7 keV; therefore, the EPIC data are only fitted together at energies above 0.7 keV. Between 0.7 – 3 keV, the data from all three instruments appears entirely consistent.

In Fig. 6.1 we present the 0.3 – 10 keV EPIC spectra fitted with an absorbed power-law. The fit is reasonable given its simplicity ($\chi^2 = 1325.4/1076$ dof); however, a number of features are immediately apparent. The total photoelectric absorption is nearly twice that expected from the Galactic hydrogen column density, indicating that I Zw 1 is intrinsically absorbed. An excess above the power-law is observed between 0.4 – 0.6 keV. The weak soft-excess is marked on the red side by absorption which extends to the energy limit of the detector, and on the blue side by an absorption feature which dips below the power-law from 0.6 – 0.8 keV. Positive residuals between 6 – 7 keV likely suggest emission due to iron.

6.4.1 Fe K emission

We begin the spectral analysis by considering the 3 – 10 keV band alone. Fitting a power-law in this region results in positive residuals between 6 – 7 keV in the observed-frame, as is shown in Fig. 6.1 ($\chi^2 = 333.4/295$ dof). In addition, the fit demonstrates that the spectrum is steep compared to broad-line Seyfert 1s, with $\Gamma = 2.24 \pm 0.05$.

We attempt several model fits to describe the feature between 6 – 7 keV. A Gaussian model, disc-line model (Fabian et al. 1989), and a Laor line model (Laor 1991) are all relatively successful in fitting the data, but none could be ruled superior over the others. In all cases, the addition of a line model results in further steepening of the power-law continuum ($\Gamma \sim 2.3$). The best-fitting parameters to the simplest line model (i.e. Gaussian profile) are $E = 6.69_{-0.33}^{+0.14}$ keV, $\sigma = 316_{-136}^{+268}$ eV, and $EW = 179 \pm 17$ eV ($\chi^2 = 309.5/292$ dof).

A further intriguing possibility for the reflection component is the existence of multiple emission lines. In Fig. 6.2, we have displayed the 5.7 – 7.1 keV pn data (6.0 – 7.5 keV rest frame energies), to take advantage of the higher signal-to-noise data afforded by the EPIC pn instrument. On careful inspection of the residuals in the pn data we can distinguish two separate humps between 6 – 7 keV. We introduce a single Gaussian into the fit and fix its energy at 6.40 keV to account for emission from neutral Fe $K\alpha$. The resulting line width is ≈ 70 eV, and both the quality of the fit and the residuals are improved ($\Delta\chi^2 = 20.2$ for 2 additional free parameter). A second Gaussian is added to model the remaining residuals at slightly higher energies. This second Gaussian further improves the fit and minimises the residuals in this spectral region ($\Delta\chi^2 = 6.4$ for 3 additional free parameters). This second line has an energy of $E \approx 6.87$ keV and it is slightly broader ($\sigma \approx 140$ eV) than the neutral Fe $K\alpha$ line. The energy of this broad line is consistent with emission from a blend of H- and He-like iron. Formal modelling, with all parameters left free to vary, resulted in a similar fit quality as the *step-wise* process just described ($\chi^2 = 307.4/290$ dof).

We further examined the possibility that the positive residuals between 6 – 7 keV could be the result of three narrow Fe $K\alpha$ lines: neutral (6.40 keV), He-like (6.70 keV), H-like (6.97 keV) lines. We included three narrow ($\sigma = 10$ eV) Gaussian profiles at the above stated energies and computed the fit. The triple line model is a good fit to the EPIC data ($\chi^2 = 308.6/293$ dof). We obtain values of $EW = 32 \pm 1$ eV, 52 ± 2 eV, and 52 ± 2 eV for the neutral, He-like, and H-like Fe $K\alpha$ lines, respectively.

Modelling of the *ASCA* observation of I Zw 1 required a strong, (partially) ionised Fe $K\alpha$ line. Leighly (1999a) fitted a 1300 eV line with a rest energy of $7.0_{-0.3}^{+0.6}$ keV, while Reeves & Turner (2000) established the line centre at $6.77_{-0.17}^{+0.11}$ keV with $EW = 483_{-211}^{+212}$ eV. Both line energies are consistent with our simultaneous fit of the pn and MOS data, using a single, broad Gaussian profile ($E = 6.69_{-0.33}^{+0.14}$ keV), though our line appears substantially weaker ($EW = 179 \pm 17$ eV). Utilising the higher sensitivity of the EPIC pn detector, we find that the broad feature between 6 – 7 keV can be well described by emission from multiple narrower lines, showing that the evidence for a truly broad line is weak. Statistically there is little difference between the two and three Gaussian fits, both are acceptable; however, the residuals at about 6.7 keV (~ 6.3 keV in the observed frame) are slightly improved by the three narrow Gaussians model. A longer exposure of I Zw 1 with *XMM-Newton*, in order to boost the signal-to-noise of the MOS data, would clarify the situation in this spectral region.

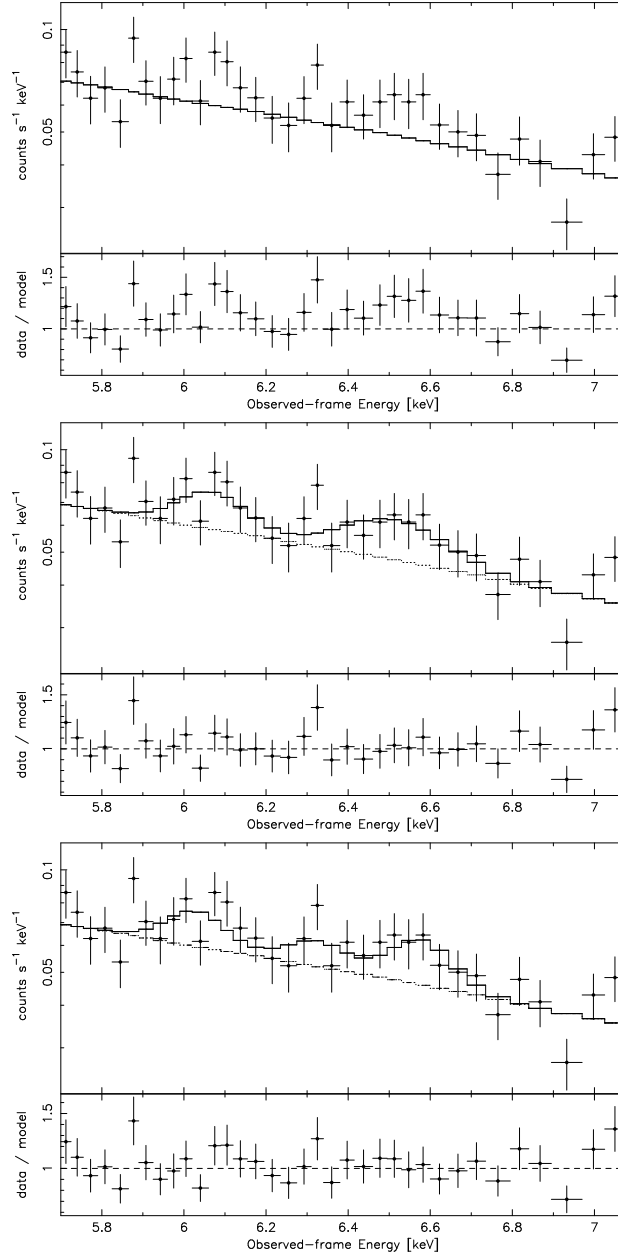


Figure 6.2: Spectral fit to the pn data between 5.7 – 7.1 keV. Upper panel: The data are fitted with the best-fit 3 – 10 keV power-law. Two separate “humps” are clearly seen in the residuals. Middle panel: Two Gaussian profiles are applied to the fit. The first line represents emission from neutral Fe $K\alpha$ ($E = 6.4$ keV), and the second line ($E \approx 6.9$ keV) is consistent with emission from a blend of H- and He-like iron. Lower panel: Three intrinsically narrow Gaussians are fitted to model possible emission from neutral ($E = 6.4$ keV), He-like ($E = 6.7$ keV), and H-like ($E = 6.97$ keV) Fe $K\alpha$.

6.4.2 The broad-band spectrum

As is illustrated by Fig. 6.1 a power-law model is a reasonable starting point for the broad-band (0.3 – 10 keV) fit. With the exception of some complexity at energies lower than ~ 1 keV, the spectrum is relatively smooth. For simplicity, we shall fit the iron complex (6 – 7 keV) with a double Gaussian model: the first Gaussian profile will be fixed at 6.4 keV to describe emission from neutral iron, and the second profile at slightly higher energies will be used to approximate emission from ionised species of iron. In addition, we have introduced a second cold absorption term. The first term is fixed to the Galactic value, while the second term will be allowed to vary and will be used to estimate the neutral absorption in I Zw 1.

With these additional parameters in place, the single power-law fit was improved at high energies, but the residuals below ~ 1 keV were not affected ($\chi^2 = 1330.7/1071$ dof). We added a second continuum component to the existing model to fit the weak soft-excess at lower energies. Neither a single blackbody ($\Delta\chi^2 = 7$ for the addition of 2 free parameters), nor a second power-law ($\Delta\chi^2 = 10$ for the addition of 2 free parameters) were entirely effective in fitting the soft-excess. A significant improvement in the overall fit is seen when the single power-law continuum is replaced with a broken power-law ($\Delta\chi^2 = 67.4$ for the addition of 2 free parameters). In this model the hard power-law ($\Gamma \approx 2.48$) dominates the spectrum at energies higher than ≈ 0.75 keV. At lower energies the spectrum is fitted with a steeper power-law with a photon index of $\Gamma \approx 2.86$. An F -test suggests that the broken power-law fit is an improvement over the single power-law at $> 99.99\%$ confidence, and that a second softer component is a required addition. An alternative model, which is thermal in nature, is a double blackbody fit ($\Delta\chi^2 = 98.3$ for the addition of 4 free parameters). In this case, the steep power-law ($\Gamma \approx 2.32$) continues to dominate much of the spectrum; however, the cooler blackbody ($kT_1 \approx 78$ eV) contributes about 20% of the total unabsorbed flux, while the hotter blackbody ($kT_2 \approx 213$ eV) contributes about 5%.

Even though both the broken power-law and double blackbody models are dramatic improvements over the single power-law fit statistically, the residuals in the low-energy band are still unsatisfactory (Fig. 6.3). In both cases, the residuals in the observed frame between 0.4–0.6 keV still exhibit the up-down trend seen in the single power-law fit, while between 0.6–0.75 keV the data remain slightly overestimated. Unfortunately, the short exposure and low signal-to-noise in the RGS does not allow us to examine productively the soft spectrum of I Zw 1. A *by-eye* inspection of the RGS spectrum does indicate a number of possible narrow absorption and emission features, but formal modelling of the spectrum does not reveal any significant results.

One successful attempt to minimise the residuals in the soft spectrum is by the addition of a Gaussian emission line. Depending on the continuum model used, the line energy is between 535 – 565 eV, with a width of $\sigma \approx 40 - 55$ eV and an equivalent width of $EW \approx 25 - 30$ eV. The addition of the soft emission feature to the broken power-law ($\Delta\chi^2 = 84$ for the addition of 3 free parameters) or double blackbody model ($\Delta\chi^2 = 65.6$ for the addition of 3 free parameters) is significant. The measured energy is consistent with emission from the He α triplet of O VII at ~ 22 Å (the resonance,

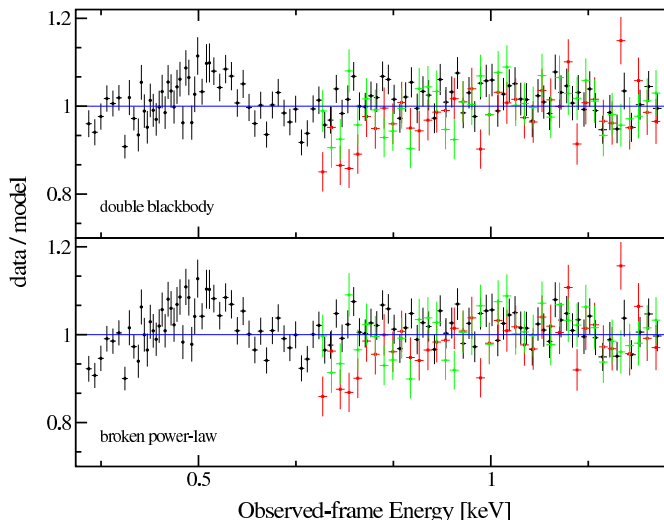


Figure 6.3: In the top panel the ratio (data/model) of the absorbed double blackbody plus power-law fit to the 0.3 – 1.3 keV EPIC data is shown. The lower panel is the absorbed broken power-law fit. Although both are an improvement over a single power-law, neither model is able to minimise the residuals (see text for details). The black circles are the pn data; the red squares and green diamonds are the MOS1 and MOS2 data, respectively. The data have been highly binned for display purposes only.

intercombination, and forbidden lines), which are known to be strong in some Seyfert galaxies (e.g. NGC 3783, Kaspi et al. 2002; Behar et al. 2003). At least two emission line-like features are suggested by the RGS spectrum at this energy, giving credence to this model. As a word of caution, we would like to make note of the calibration issues around the O-edge in the EPIC pn detector. Although the calibration is significantly improved in SAS v5.4.1 (Kirsch 2003), and we do not believe that it has any bearing in this observation, it is difficult to make strong claims about this feature without independent data.

An alternative method to minimise the residuals in the soft spectrum is to add an absorption feature (edge or line) on the blue-side of the excess. I Zw 1 does possess UV absorption (Laor et al. 1997; Crenshaw et al. 1999), so it seems perfectly reasonable that it would also possess some complex X-ray absorption.

In the first attempt we introduce an absorption line into the fit. The addition of the absorption feature results in a small statistical improvement to the broken power-law model ($\Delta\chi^2 = 18.7$ for the addition of 3 free parameters). The line energy is at $E \approx 749$ eV and it is very weak ($EW \approx -6$ eV). However, the addition of the absorption line is better received by the double blackbody model ($\Delta\chi^2 = 49.9$ for the addition of 3 free parameters). In this case, the equivalent width is about -22 eV and the line is centred at about 737 eV. The addition of the line also minimises the residuals in a satisfactory manner. Broad absorption features at these energies are

most consistent with unresolved transition array (UTA) absorption due to Fe M-shell ions ($\sim 729 - 774$ eV; Behar et al. 2001), as observed in IRAS 13349+2438 (Sako et al. 2001), NGC 3783 (Blustin et al. 2002; Kaspi et al. 2002; Behar et al. 2003), and Mrk 509 (Pounds et al. 2001).

Alternatively, the low-energy absorption line can be replaced with an absorption edge. Again, for the two continuum models we are working with, the statistics are improved: $\Delta\chi^2 = 68.4$ and 60 for the addition of 2 free parameters for the broken power-law fit and the double blackbody fit, respectively. For both models, the optical depth of the edge is $\tau \approx 0.23 - 0.26$, and the edge energy is at $E \approx 664 - 689$ eV. The best-fit edge energies do not agree with the strongest edge feature which is expected at 731 eV (O VII). However, this inconsistency in the edge energy alone does not permit us to discard this interpretation. The edge could very well be blended with other absorption features, perhaps even with some neutral iron absorption as was seen in MCG-6-30-15 (Lee et al. 2001), in which case our model is too simple.

The three best-fitting phenomenological models of the 0.3 – 10 keV spectrum of I Zw 1 are shown in Table 6.1. The continuum can be modelled by either a broken power-law or a double blackbody and power-law. There are primarily two difficulties in distinguishing between these apparently very different models. The first is that the soft spectrum is complex. We demonstrated that an absorption edge or an emission feature is a significant improvement to both continuum models, in addition to extra neutral absorption. The second fact is that the soft-excess is weak and the hard power-law component dominates much of the spectrum down to ~ 750 eV.

All of the models have the disadvantage of possibly overestimating the photoelectric absorption in I Zw 1. The models require cold absorption on the order of 10^{21} cm^{-2} in addition to the Galactic value, which is nearly a factor of 10 higher than was estimated by the *ROSAT* observations (Boller et al. 1996; Lawrence et al. 1997). Given that *ROSAT* was sensitive down to 0.1 keV, it stands to reason that its value for the intrinsic absorption is reliable. However, the high value measured with *XMM-Newton* is most likely a proxy for more complicated absorption (e.g. blended absorption lines and/or edges). Given the very complex nature of the low-energy absorption in Seyferts, fitting simple models such as these can only be illustrative of a much more complicated situation. A long exposure, to utilise the high-resolution RGS, is required to probe the soft absorption in a meaningful way.

A slight advantage is given to the double blackbody plus power-law continuum in its ability to fit the iron emission between 6 – 7 keV. The model is successful in predicting a high-energy continuum and an iron complex which is similar to that described in Section 6.4. In contrast, the broken power-law continuum requires a very broad ($\sigma \approx 1.5$ keV) neutral line. The neutral line width is certainly overestimated by the fit to compensate for a continuum which is poorly defined between 7 – 10 keV. A possible shortcoming for the double blackbody model is that the temperatures estimated for the thermal components are high ($kT_1 \approx 198$ eV and $kT_2 \approx 94$ eV) for a standard accretion disc around a $10^7 M_\odot$ black hole. However, since we do not understand the physics of the soft-excess very well we cannot automatically deem the model as unphysical. For example, bulk motions in the disc (Socrates et al. 2004) or slim-disc approximations

Table 6.1: Best-fit model parameters to the 0.3 – 10 keV EPIC data. The columns are: (1) the applied model (in addition to two Fe K α emission lines); (a) double blackbody continuum with absorption edge; (b) broken power-law continuum with absorption edge; (c) double blackbody continuum with soft X-ray emission line; (2) reduced χ^2 , (3) photoelectric absorption intrinsic to I Zw 1, (4) temperature of the first blackbody component, (5) temperature of the second blackbody component, (6) photon index of the first power-law component, (7) energy at which the photon index changes in the broken power-law fit, (8) photon index of the second power-law component, (9) edge energy, (10) edge optical depth, (11) line energy, (12) line width, and (13) best-fit equivalent width. The superscript *f* indicates that the parameter is fixed to that value, and *b* indicates only the best-fit value.

(1) Model	(2) χ^2_ν (dof)	(3) $N_{H,Zw1}$ ($\times 10^{20}$ cm $^{-2}$)	(4) kT_1 (eV)	(5) kT_2 (eV)	(6) Γ_1	(7) E_{brk} (keV)	(8) Γ_2	(9) E_{edge} (eV)	(10) τ	(11) E_{line} (keV)	(12) σ (eV)	(13) EW (eV)
(a)	1.10 (1065)	10.1 ± 0.2	198 ± 5	94 ± 2	2.35 ± 0.01	—	—	664^{+10}_{-13}	$0.26^{+0.02}_{-0.01}$	6.4^f	43^b	38
(b)	1.11 (1067)	10.0 ± 0.1	—	—	2.80 ± 0.02	$1.44^{+0.06}_{-0.05}$	2.47 ± 0.02	689^{+9}_{-13}	$0.23^{+0.02}_{-0.01}$	$6.84^{+0.09}_{-0.11}$	188^{+140}_{-90}	128
(c)	1.10 (1064)	10.8 ± 0.1	177 ± 5	67 ± 2	2.35 ± 0.01	—	—	—	—	6.4^f	1572^{+616}_{-400}	593
										$6.73^{+0.17}_{-0.18}$	227^{+177}_{-154}	92
										6.4^f	47^b	41
										$6.84^{+0.08}_{-0.11}$	187^{+114}_{-69}	135
										0.56 ± 0.01	45^b	28

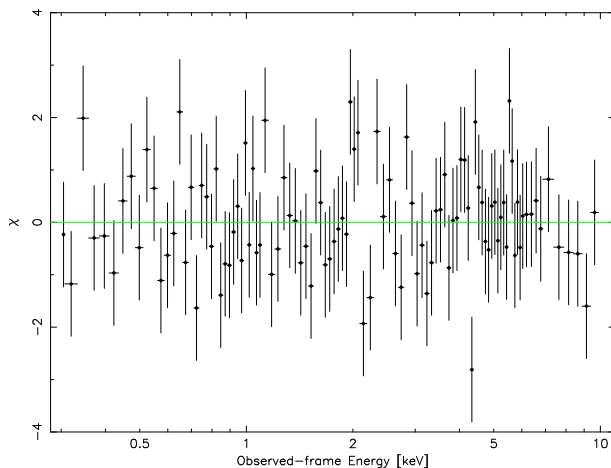


Figure 6.4: The broad-band data-to-model residuals (in terms of σ) obtained from the double blackbody phenomenological fit to the EPIC data (see text and Table 6.1 for details). For clarity, only the highly-binned pn residuals are shown.

(Abramowicz et al. 1988) can alter the shape of the soft-excess from that expected of a standard accretion disc. If we allow a soft-excess component with curvature (rather than a power-law) the systematic residuals at low energies can be made to diminish. In addition, such curvature in the soft-excess allows for better fitting of the high-energy continuum component and hence, the iron emission features. The final model residuals are shown in Fig. 6.4.

The average 0.3 – 10 keV flux, estimated from the double blackbody fit and correcting for Galactic extinction is $\sim 2.40 \times 10^{-11} \text{ erg cm}^{-2} \text{ s}^{-1}$. The corresponding luminosity is $2.03 \times 10^{44} \text{ erg s}^{-1}$, and the luminosity in the 2 – 10 keV band is $0.72 \times 10^{44} \text{ erg s}^{-1}$. In comparison, during the *ASCA* observation the 0.5 – 10 keV luminosity was $1.36 \times 10^{44} \text{ erg cm}^{-2} \text{ s}^{-1}$, and the 2 – 10 keV luminosity was $0.53 \times 10^{44} \text{ erg s}^{-1}$ (Leighly 1999a).

6.5 Timing analysis

In this Section, we will discuss the variability properties of I Zw 1. The pn and MOS light curves were both analysed and found to be entirely consistent. We will only discuss the results from the pn, given its higher signal-to-noise. The 1σ errors on the light curves were calculated using counting statistics.

6.5.1 The broad-band light curve

In Fig. 6.5 we present the 0.3 – 12 keV EPIC pn light curve of I Zw 1 in 200 s bins. The average count rate is $6.97 \pm 0.19 \text{ count s}^{-1}$. The minimum and maximum 0.3 – 12 keV count rates are 5.76 ± 0.17 and $9.80 \pm 0.22 \text{ count s}^{-1}$, respectively. The most notable feature in the light curve is obviously the flare starting at ~ 10 ks, when the count

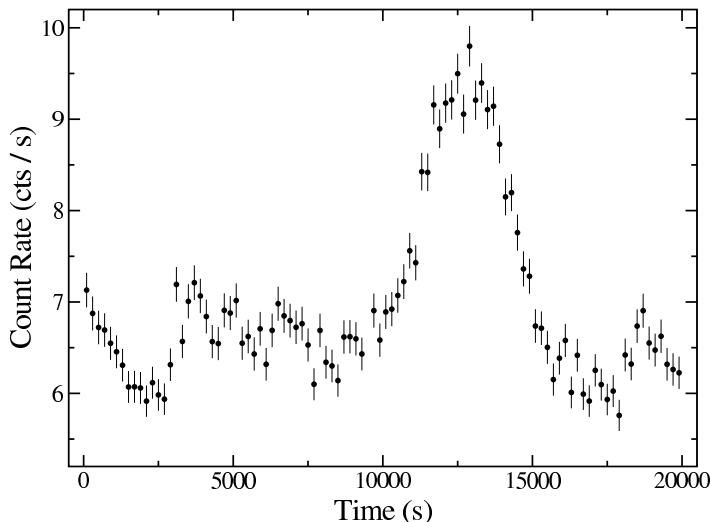


Figure 6.5: The 0.3 – 12 keV light curve of I Zw 1 in 200 s bins. Zero seconds on the time axis marks the start of the observation at 09:18:44 on 2002–06–22.

rate increases by $\sim 40\%$ in 2500 s. The flare is remarkably symmetric as the count rate returns from maximum to its pre-flare value in the same amount of time. Except for the flare, the rest of the light curve is surprisingly serene. Considering only the periods between 0–10 ks and 15–20 ks, the fluctuations about the mean are only about 10%, which is comparable to the observed variability on similar time scales during the *ASCA* observations (Leighly 1999b); but modest compared to many NLS1 X-ray light curves. However, an observation with *ROSAT* did find that the 0.1 – 2.4 keV flux dropped by about 25% in ~ 6000 s (Boller et al. 1996). It was not clear from that observation if the flux drop was subsequent to a rapid rise or part of a gradual decrease for an extended period of time. In the remainder of this Chapter we will often make reference to I Zw 1 in its high- and low-flux states. In defining the high-flux state, we have selected the entire flaring event from $\sim 10 - 15$ ks. The low-flux state includes all of the data from the remaining time intervals.

We have calculated the radiative efficiency (η), assuming photon diffusion through a spherical mass of accreting material (Fabian 1979; but see also Brandt et al. 1999 for a discussion of important caveats). The most rapid rise occurs from 10.1–12.6 ks when the luminosity increases by 7.41×10^{43} erg s $^{-1}$. The corresponding radiative efficiency is only $\eta \gtrsim 0.02$, which does not necessarily require radiative boosting or anisotropic emission during the flaring event.

As a first test for spectral variability we calculate the fractional variability amplitude (F_{var} ; Edelson et al. 2002) to examine the degree of variability in different energy bands. The fractional variability amplitude is calculated in eight energy bins between 0.3 – 12 keV using 200 s binning of the light curves (Fig. 6.6). The F_{var} spectrum of I Zw 1 is remarkably different from the typically flat spectrum seen in other NLS1

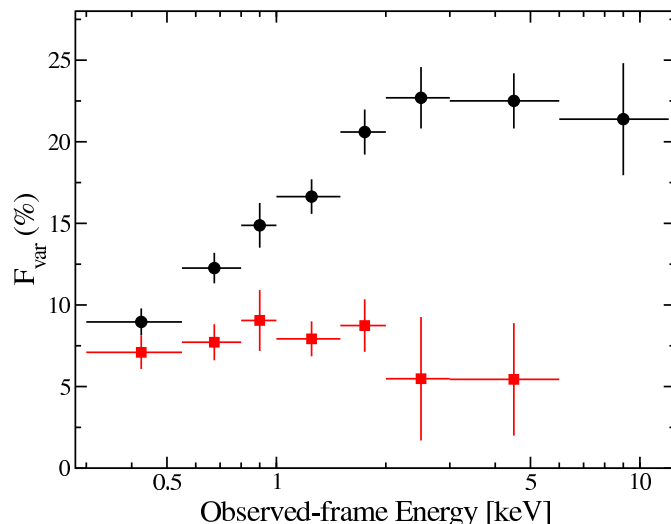


Figure 6.6: F_{var} calculated in eight energy bins between 0.3 – 12 keV using 200 s binning of the light curves. The black circles include the data from the entire 20 ks observation. The red squares are the F_{var} recalculated, neglecting the data between 10 – 15 ks (the X-ray flare). The 6 – 12 keV data point in the second data set (red squares) is omitted due to degeneracy in the calculation of F_{var} .

such as 1H 0707–495 (Boller et al. 2002) and Ton S180 (Vaughan et al. 2002). The variations intensify as the energy increases and maximise between 2 – 12 keV. The F_{var} spectrum gives the sense of a variable hard power-law which is physically distinct from the softer, less variable, emission component.

Much of the spectral variability observed in Fig. 6.6 is associated with the X-ray flare seen in the broad-band light curve. We recalculated the F_{var} , but this time only for the low-flux state. The result is shown as the red squares in Fig. 6.6. The low-flux state fractional variability in each bin is less than 10%, and consistent with a constant across the entire spectrum ($\chi^2 = 2.6/6$ dof). Fig. 6.6 demonstrates that the spectral variability is stimulated by the flux outburst in Fig. 6.5.

6.5.2 The hard X-ray flare and flux-induced spectral variability

By investigating the light curves in various energy bands we can demonstrate that the flare is concentrated at higher energies. In Fig. 6.7 we have plotted the normalised light curves in the 0.3 – 0.8 keV and the 3 – 12 keV bands. The light curves are normalised to the average count rate during the periods 0 – 8.2 ks and 17 – 20 ks. Clearly, the higher energy band is significantly more variable during the flaring event than the soft band. During the flare the hard count rate increases by $\sim 100\%$, whereas the soft band shows only about a 20% increase. This is the first time, to the best of our knowledge, that a hard X-ray flare has been detected from a NLS1.

The hardness ratio variability curve (Fig. 6.8) is calculated using the formula

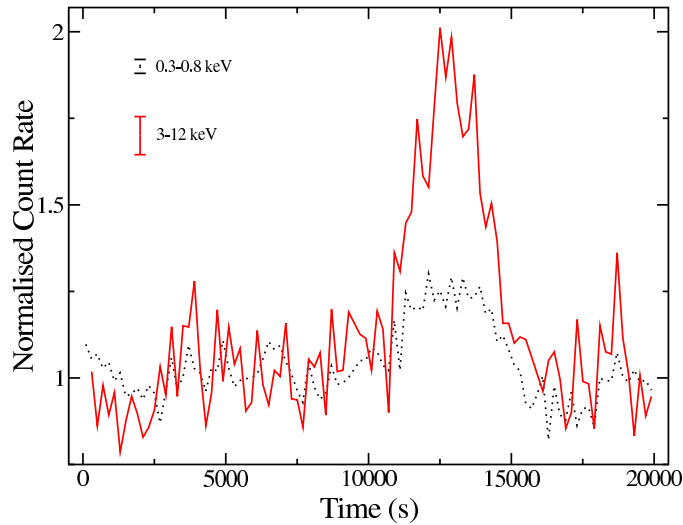


Figure 6.7: The 0.3–0.8 keV (black dotted curve) and 3–12 keV (red solid curve) normalised light curves. The vertical lines in the top left of the graph indicate the size of the average error bars. Zero seconds on the time axis marks the start of the observation at 09:18:44 on 2002–06–22.

$(H - S)/(H + S)$, where H and S are the count rates in the hard and soft bands, respectively. The hardness ratio variability curve shows similar behavior as the light curve in Fig. 6.5. The hardness ratio exhibits only small variations for most of the observation, but then the fluctuations become enhanced between 10 – 15 ks, showing spectral hardening precisely during the time of the hard X-ray flare. The significance of the relation between Fig. 6.5 and Fig. 6.8 is measured with the Spearman rank correlation coefficient to be significant at $> 5\sigma$.

The fact that the flare is stronger at high energies implies that its origin is not in the cold accretion disc. It is plausible that the flare originates in the accretion-disc corona due to magnetic reconnection (e.g. Galeev et al. 1979). The hard flare would then irradiate the disc, where the high-energy photons will be reprocessed to lower energies via Compton down-scattering. In this simple picture, we may expect to see a time lag between the low and high energy light curves if the light travel time between the corona and disc is substantial. In order to investigate this we calculate cross correlation functions using 200 s bins for a number of light curves in various energy ranges. All of the cross correlations are relatively symmetric and consistent with zero time delay. The results suggest that there are no leads or lags greater than ± 100 s between the various energy bins. Assuming the simple flare geometry discussed above, this result implies a very compact system, in which the light travel time between the disc corona and the accretion disc itself is < 100 s. All responses to the hard X-ray flare (light travel-time, reprocessing, spectral changes) appear to occur on short time scales.

Another consideration is whether the flare, which appears to induce the spectral

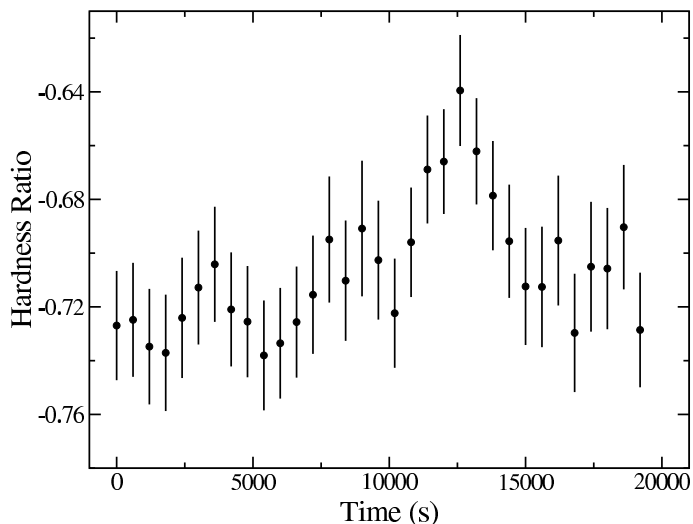


Figure 6.8: Hardness ratio variability curve for $H = 2 - 12$ keV and $S = 0.3 - 2$ keV (see text for details). Zero seconds on the time axis marks the start of the observation at 09:18:44 on 2002-06-22.

variability, has any long-term effect on the spectrum; that is, even after the flux has returned to its pre-flare value. To examine this possibility in a model-independent manner, we calculated the ratio between the pre-flare data (< 10 ks) and the post-flare data (> 15 ks). The ratio is displayed in Fig. 6.9. There appears to be little difference in the ratio across the spectrum, and a constant fit to the ratio is acceptable ($\chi^2 = 29.5/30$ dof). Even the difference in the average flux is on the order of 2%. However, on closer examination we notice that all nine data points below ~ 1.2 keV lie above the ratio average. The probability that this is a random event is $1/512$. Fig. 6.9 indicates that the soft flux prior to the flare is higher than the post-flare soft flux. The shortage of post-flare data makes it difficult to determine whether this subtle spectral difference is associated with the flare or a coincidental event.

6.5.3 The nature of the spectral variability

We have demonstrated that the flare is indeed hard, and that it induces spectral variability. The spectrum appears to become harder as the flare intensifies, and the changes brought on by the flare are immediate. Could the spectral variability be described by a component with a constant spectral slope but variable flux? Or is it more likely that the spectral variability is a result of a pivot in the X-ray spectrum at some higher energy? Taylor et al. (2003) have presented a model-independent technique to distinguish between these forms of spectral variability. However, given the limited data we have available from this short observation it is not possible to apply their technique successfully.

Fabian et al. (2002) and Fabian & Vaughan (2003) have successfully used a dif-

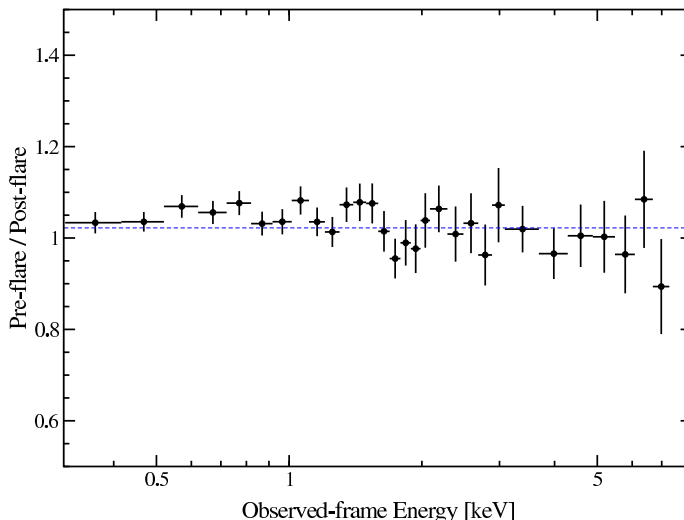


Figure 6.9: The ratio between the pre-flare and post-flare data. The dotted line represents the ratio average.

ference spectrum (high-flux minus low-flux spectrum) to investigate the nature of the spectral variability in MCG–6–30–15. If the difference spectrum can be fitted with a power-law then the spectral variability between the two flux states can be attributed to a difference in the normalisation of the intrinsic power-law without requiring a change in its spectral slope. In Fig. 6.10 we display the residuals from the difference spectrum for I Zw 1 fitted with a power-law modified by cold absorption. The fit is a reasonable approximation ($\chi^2_{\nu} = 1.05$).

We further considered the spectral differences between the two flux states by modelling the high and low-flux state pn spectra separately. To both spectra we re-fit the double blackbody model described in Section 6.4 (Table 6.1 model (a)). In both the low- and high-flux states, we found that the only significant changes in the model parameters were to the normalisation of the continuum components. Within 90% confidence the values for the temperatures of the thermal components, edge energy, and neutral absorption were consistent. Even the photon indices of the low- and high-flux state power-law components were consistent ($\Gamma_{high} = 2.31^{+0.06}_{-0.04}$ and $\Gamma_{low} = 2.35^{+0.10}_{-0.06}$). A noticeable difference occurred only in the relative fluxes ($f = F_{3-10 \text{ keV}}/F_{0.3-2.0 \text{ keV}}$) during the two flux states. During the low-flux state $f_{low} = 0.20 \pm 0.01$, whereas during the high-flux state $f_{high} = 0.26 \pm 0.02$.

A further point to note is the possibility of changes in the strength of the iron line(s) between the different flux states. The spectra during the two flux states show a very similar continuum shape across the 0.3 – 10 keV band; however, the iron lines appear stronger during the low-flux (non-flare) state while the normalisation of the lines remains consistent. The equivalent widths of the neutral and ionised iron lines during the low state are 65^{+4}_{-6} eV and 143^{+10}_{-14} eV, respectively, while during the flare

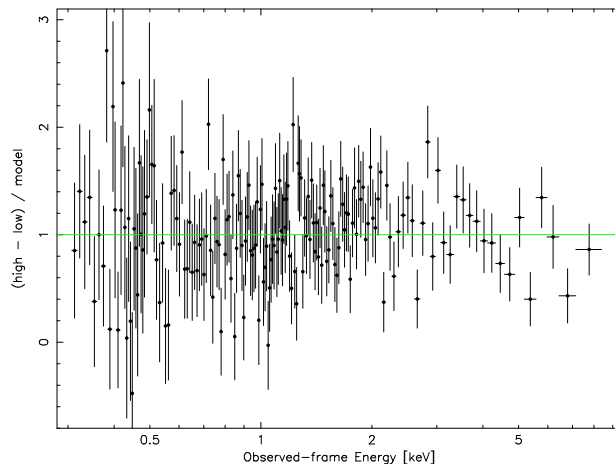


Figure 6.10: The residuals from the difference spectrum (high-flux minus low-flux spectrum) fitted with a power-law modified by neutral absorption over the 0.3–10 keV band. The data have been binned-up for display purposes.

the strengths are 46_{-4}^{+2} eV and 70_{-10}^{+4} eV. Although the line parameters are especially model dependent and our exposure is short, I Zw 1 appears to be another object in which the iron lines do not vary as significantly or in response to (in a simple manner) the continuum flux variations (Fabian et al. 2002; Lee et al. 2000, Reynolds 2000, Iwasawa et al. 1996).

6.6 Summary

We have presented a 20 ks *XMM-Newton* observation of I Zw 1, the prototypical NLS1. Our findings are summarized below.

- (1) The 0.3–10 keV continuum can be described by either a double blackbody plus a power-law or a broken power-law, modified by intrinsic cold absorption. The soft-excess is weak, but notable at energies between $\sim 0.4 - 0.7$ keV. Superimposed on this continuum are absorption and/or emission features below ~ 1.0 keV, and strong Fe $K\alpha$ emission between 6.4 – 6.8 keV.
- (2) The Fe $K\alpha$ emission can be successfully fitted with several models, and the current observation does not allow us to determine the best one. The pn data suggest that the Fe $K\alpha$ complex may be resolved into emission from a neutral line at 6.4 keV and an ionised component at ~ 6.9 keV (blend of He- and H-like Fe), weakening the case for a truly broad line.
- (3) The low-energy spectrum can be modelled with either an absorption line or edge. The current observation does not allow us to distinguish between these two models. On the other hand, a low-energy emission feature ($E \approx 0.55$ keV) can be introduced to the fit with relative success.

- (4) We find an X-ray flare which is isolated mostly in the 3 – 12 keV band. We find that the hard X-ray flare induces spectral variability in such a way that the spectrum becomes *harder* during the flare. There are no discernible lags between energy bands down to ± 100 s. Comparison of the pre-flare and post-flare spectra show that there is a subtle difference in the spectrum prior to and after the flare. It is not certain whether this spectral variability is related to the hard flare.
- (5) The flux of the iron line(s) do not appear to respond to the change in the continuum flux during the flare. The lines are strongest during the low-flux (non-flare) state.

6.6.1 The low-energy spectrum

The quality of the data from this short exposure does not allow us to distinguish between an absorption line or an edge, or an emission line in describing the features in the soft spectrum. If the absorption is interpreted as a line then the best-fit energy may be suggestive of an UTA feature due to Fe M absorption. An absorption edge is a slightly better fit than the line. The best-fit edge energy is not consistent with that of O VII, which would indicate that the edge is severely blended with other absorption features. The emission line interpretation is consistent with emission coming from a blend of O VII lines at ~ 22 Å. The most likely scenario is that we have a combination of O VII emission as well as absorption, but with the resolution of the EPIC instruments it is not possible to measure accurately the contribution from each component. In any regard, we have demonstrated that the soft spectrum of I Zw 1 is complex and warrants a deep observation to utilise the RGS.

6.6.2 The hard X-ray flare

The detection of a hard X-ray flare, and spectral hardening during the flare, is entirely consistent with theories of an accretion-disc corona which is being heated by magnetic reconnection (e.g. Galeev et al. 1979). The apparent instantaneous response of the lower-energy emission mechanisms to the hard X-ray flare suggests that the light travel-time between the emission regions is < 100 s. Deeper analysis of the spectral variability suggests that spectral changes are due to an increase in the high-energy flux relative to the low-energy flux, and not due to a change in the intrinsic shape of the continuum. The weakness of the flare at low X-ray energies may be indicating that the seed photons for the Comptonisation component are not coming from the 0.3 – 1 keV band, but probably from lower UV energies. This observation could perhaps be useful in constraining Comptonisation models.

This short exposure with *XMM-Newton* has revealed a number of fascinating traits in I Zw 1. I Zw 1 has once again proven to be an important object in allowing us to probe many interesting facets of AGN, such as: X-ray flares, warm-absorption, and complex Fe K α emission. A long exposure with *XMM-Newton* and *Chandra* would be quite rewarding for studying these traits in greater detail.

Chapter 7

An intense soft-excess and evidence for light bending in the luminous narrow-line quasar PHL 1092

7.1 Introduction

The narrow-line quasar PHL 1092 ($z = 0.396$) was observed by *XMM-Newton* as part of the Guaranteed Time Program to study Narrow-Line Seyfert 1 type objects (NLS1). The importance of PHL 1092 was realised by Bergeron & Kunth (1980) when it appeared unique among a sample of quasars due to its outstanding Fe II emission. During the *ROSAT* era PHL 1092 was recognised as a high-luminosity analogue of the NLS1 phenomenon (Forster & Halpern 1996; Lawrence et al. 1997). Remarkable variability was observed during an 18-day *ROSAT* HRI monitoring campaign (Brandt et al. 1999; hereafter BBFR), including a number of high-amplitude flaring events. The most extreme variability was an increase in the rest frame count rate by nearly a factor of four in less than 3580s, corresponding to a radiative efficiency (Fabian 1979; see also Section 7.4) of $\eta \gtrsim 0.63$. Such extreme variability had never before been observed in such a high-luminosity radio-quiet quasar.

The objectives of this study are to determine if PHL 1092 consistently exhibits such extreme behavior, and to constrain better the physical nature of its X-ray spectral energy distribution.

7.2 Observation and data reduction

PHL 1092 was observed with *XMM-Newton* (Jansen et al. 2001) on two separate occasions. The first observation occurred on 2000 July 31 during revolution 0118 and lasted for ~ 32 ks. During this time the EPIC pn (Strüder et al. 2001) and MOS (MOS1 and MOS2; Turner et al. 2001) cameras, as well as the Optical Monitor (OM; Mason et al. 2001) and the Reflection Grating Spectrometers (RGS1 and RGS2; den Herder et al. 2001) collected data. From this first observation EPIC, OM, and RGS event files were

Table 7.1: Source plus background and background pn counts collected in various energy bins. Energies are given in units of keV. The background counts have been scaled to the source cell size.

	$0.3 \leq E \leq 2$	$2 < E < 4$	$4 \leq E < 7.2$
Source + background	11888	247	203
Background	200	40	78

created and supplied by the *XMM-Newton* Science Operations Centre. On analysing the EPIC data it was found that problems with the energy calibration existed. As such, the EPIC spectra could not be exploited due to calibration uncertainties within the small energy bins utilised for spectral analyses. Fortunately, broad-band light curves are not as sensitive to calibration uncertainties as spectra; hence it was possible to construct a pn light curve from these data. RGS and OM files were not affected. Since the Observation Data Files (ODFs) could not be recovered for this observation PHL 1092 was re-observed on 2003 January 18 during AO2 (revolution 0570) for ~ 28.5 ks. During this second observation all instruments were functioning, and the ODFs were successfully produced. At both epochs, the EPIC instruments used the medium filter and were operated in full-frame mode.

The ODFs were processed to produce calibrated event lists using the *XMM-Newton* Science Analysis System (**SAS v5.4.1**). Unwanted hot, dead, or flickering pixels were removed as were events due to electronic noise. Event energies were corrected for charge-transfer losses. EPIC response matrices were generated using the **SAS** tasks **ARFGEN** and **RMFGEN**. Light curves were extracted from these event lists to search for periods of high background flaring. High-energy background flaring was found to be extensive resulting in a loss of $\sim 25\%$ of the data. The total amount of good exposure time selected was 18795 s. The source plus background photons were extracted from a circular region with a radius of $35''$, and the background was selected from an off-source region with a radius of $50''$, and appropriately scaled to the source region. Single and double events were selected for the pn detector, and single-quadruple events were selected for the MOS. The total number of counts collected by the pn instrument in the $0.3 - 10$ keV range was 12399. In Table 7.1 we give a distribution of the counts with respect to energy. The *XMM-Newton* observation provides a vast improvement in spectral quality over the 72.2 ks *ASCA* exposure (199.6 ks duration) in which ≈ 2900 count were collected (Leighly 1999a). In addition, *XMM-Newton* is sensitive at lower energies than *ASCA* was, and this is critical in analysing this very soft source. Although *ROSAT* was capable of observing even lower energies than *XMM-Newton*, only 2235 count were collected in the $0.1 - 2$ keV range during the PSPC observation (Forster & Halpern 1996; Lawrence et al. 1997).

The RGS event lists were also created from the ODFs following standard **SAS** procedures. However, it was determined that the RGS data from both epochs were background dominated and would not be useful for this analysis.

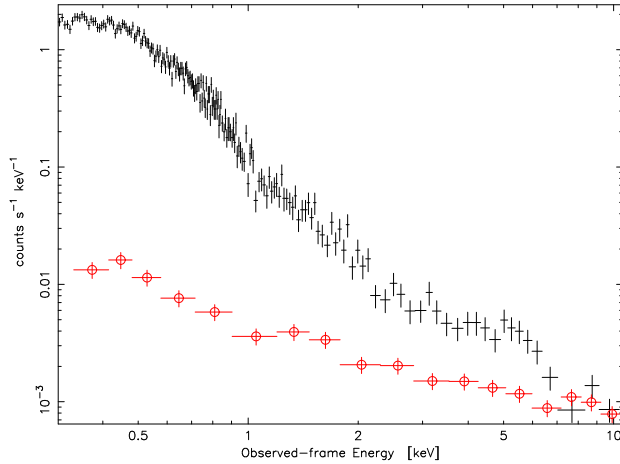


Figure 7.1: The pn source and background spectra. The upper curve (black crosses) is the source plus background spectrum. The lower curve (red, open circles) is the background spectrum. The data above 7.2 keV are ignored as the source spectrum becomes background dominated.

The Optical Monitor collected data through the *UVW2* filter (1800 – 2250 Å) for about the first 12 ks of each observation, and then it was switched to UV grism mode for the remaining time. In total, five photometric images were taken at each epoch. The exposure times during the 2000 June observation were 2300 s, and during the 2003 January observation they were 2640 s.

7.3 X-ray spectral analysis

Each of the EPIC spectra was compared to the respective background spectrum to determine in which energy range the source could be reasonably detected above the background. The data were determined to be source dominated up to energies of ~ 7.2 keV (~ 10 keV in the rest frame; Fig. 7.1). In addition, the MOS data were ignored below 0.7 keV due to the uncertainties in the low-energy redistribution characteristics of the cameras (Kirsch 2003). When fitted with a power-law, the MOS1 data above 2.5 keV displayed a steeper slope compared to the equivalent pn and MOS2 slopes ($\Delta\Gamma \sim 0.20 - 0.25$). This inconsistency in the MOS1 data was previously realised in observations of 3C 273 by Molendi & Sembay (2003). Molendi & Sembay noted a difference in the MOS1 photon index compared to the other EPIC photon indices of $\Delta\Gamma \sim 0.1$. We note that since the PHL 1092 high-energy spectra are dominated by the pn data, and that the high-energy photon statistics are generally poor compared to the low-energy statistics, the inconsistency in the MOS1 photon index has little adverse effect on the results. All of the MOS data above 0.7 keV, and pn data above 0.3 keV were utilised during the spectral fitting, but the residuals from each instrument were examined separately to judge any inconsistency.

The source spectra were grouped such that each bin contained at least 20 counts.

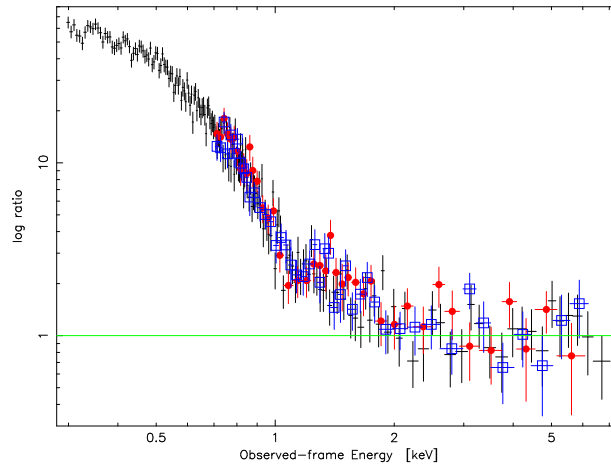


Figure 7.2: The ratio (data/model) resulting from fitting an absorbed power-law ($\Gamma = 1.42_{-0.50}^{+0.63}$) to the 3 – 7.2 keV EPIC data and extrapolating to lower energies. The black crosses, red dots, and blue squares correspond to the pn, MOS1, and MOS2 residuals, respectively. Note that the ratio axis is logarithmic.

Spectral fitting was performed using *XSPEC* v11.2.0 (Arnaud 1996). Fit parameters are reported in the rest frame of the object, although most of the figures remain in the observed frame. The quoted errors on the model parameters correspond to a 90% confidence level for one interesting parameter (i.e. a $\Delta\chi^2 = 2.7$ criterion). Luminosities are derived assuming isotropic emission. The Galactic column density toward PHL 1092 is $N_{\text{H}} = (3.6 \pm 0.2) \times 10^{20} \text{ cm}^{-2}$ (Murphy et al. 1996).

A value for the Hubble constant of $H_0 = 70 \text{ km s}^{-1} \text{ Mpc}^{-1}$ and a standard cosmology with $\Omega_M = 0.3$ and $\Omega_\Lambda = 0.7$ has been adopted.

7.3.1 The broad-band spectrum

A single absorbed power-law is a poor fit to the 0.3 – 7.2 keV data ($\chi^2 = 870.5/266$ dof). The high statistics below ~ 2 keV dominate the fit resulting in large residuals at higher energies which demonstrates the need for multiple continuum components. For illustrative purposes, a single power-law ($\Gamma = 1.42_{-0.50}^{+0.63}$) modified by Galactic absorption was fitted to the 3 – 7.2 keV EPIC data and extrapolated to lower energies. The fit reveals the impressive strength of the soft-excess below ~ 2 keV (Fig. 7.2).

Thermal disc models were implemented to fit the soft-excess. Either a single blackbody or a multi-colour disc blackbody (MCD; Mitsuda et al. 1984; Makishima et al. 1986) would be a valuable supplement to the initial power-law fit ($\chi^2 = 289.6/264$ dof and $\chi^2 = 290.1/263$ dof, respectively). The intrinsic column density was treated as a free parameter and determined to be insignificant in both models ($< 10^{19} \text{ cm}^{-2}$). A double power-law fit and a broken power-law fit were also attempted to assess whether the soft-excess could be attributed to Comptonisation. Neither the double power-law nor the broken power-law models were statistically acceptable ($\chi^2 = 480.0/263$ dof and $464.3/263$ dof, respectively). In addition, both Comptonisation models required

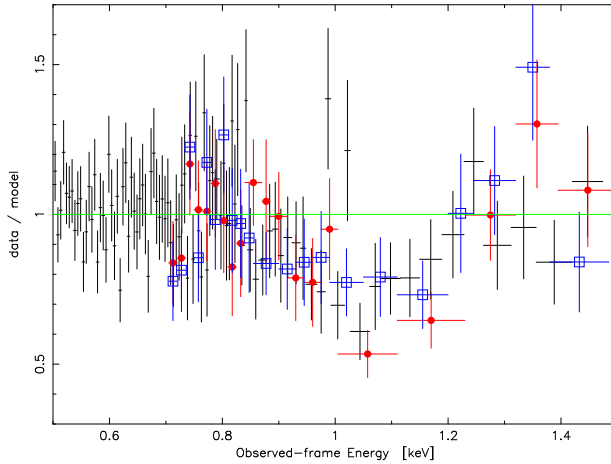


Figure 7.3: An absorption-like feature detected in all three EPIC instruments at ~ 1 keV (~ 1.4 keV in the rest frame). The continuum is represented by the best-fit model described in Section 7.3 and Fig. 7.5. See also model (a) in Table 7.2. The black crosses, red dots, and blue squares correspond to the pn, MOS1, and MOS2 residuals, respectively. The data have been re-binned for display purposes.

a high intrinsic column density, on the order of 10^{21} cm $^{-2}$. Such a large amount of intrinsic cold absorption above the Galactic value is inconsistent with the previous findings with *ROSAT* (Forster & Halpern 1996; Lawrence et al. 1997; BBFR). The high column density derived with the power-law models is undoubtedly manifested to accommodate a soft-excess with intrinsic curvature.

Regardless of the preferred continuum model, a depression remained in the residuals at approximately 1 keV (1.4 keV in the rest frame; Fig. 7.3). A Gaussian profile was added to the fits to model a potential absorption line. The supplementary component was an improvement to both the blackbody plus power-law fit ($\Delta\chi^2 = 16.1$ for the addition of 3 free parameters) and the MCD plus power-law fit ($\Delta\chi^2 = 31.1$ for the addition of 3 free parameters). The best-fit energy ($E = 1.43 \pm 0.04$) and equivalent width ($EW = -82_{-22}^{+19}$) are consistent with similar features observed in other NLS1 (e.g. Leighly 1999b; Vaughan et al. 1999). The addition of a Gaussian profile was also a significant improvement to the Comptonisation models; however, it did not alleviate the requirement of a high column density in these models. Replacing the absorption line with an edge also improved the fit, but not as well as the line model ($\Delta\chi^2 = 17.5$ for the addition of 2 free parameters to the MCD plus power-law model). The edge energy is $E \approx 1.33$ keV, inconsistent with the strong edges arising in a warm absorber (e.g. O VII or O VIII). The residuals between about 1 – 1.2 keV in Fig. 7.2 show a slight rise. We examined the possibility that the residuals in the 1 – 2 keV range could be due to an emission feature rather than absorption. Indeed an emission feature was an improvement to the MCD plus power-law fit ($\Delta\chi^2 = 25.3$ for the addition of 3 free parameters), but not quite as good as an absorption line. In addition, the energy and strength of the feature ($E \approx 1.97$ keV and $EW \approx 350$ eV) are difficult to reconcile with the current understanding of warm emission. Furthermore, residuals

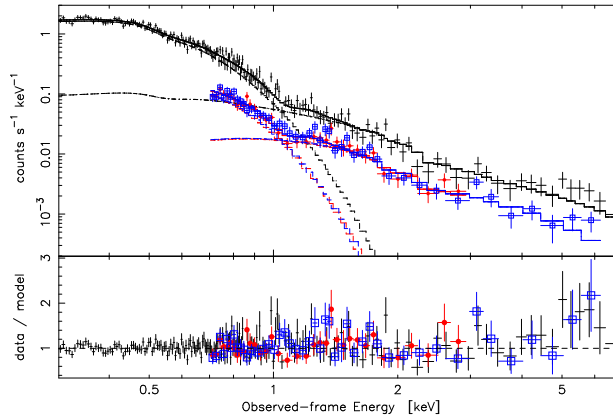


Figure 7.4: The MCD plus power-law and an absorption line model fitted to the EPIC 0.3 – 7.2 keV data (see text for details). In the lower panel the residuals (data/model) are shown. While the fit is statistically acceptable, it is rather poor above ~ 2 keV. The black crosses, red dots, and blue squares correspond to the pn, MOS1, and MOS2 points, respectively. For clarity the MOS1 data and residuals above 3 keV are not included in the figure (see text for detail).

still remained at ~ 1 keV, and when these residuals were modelled the parameters of the emission feature were no longer constrained.

7.3.2 Evidence for a reflection component

In a statistical sense the MCD and power-law model with an absorption line at ~ 1.4 keV is a very good fit ($\chi^2 = 259.0/260$ dof). However, when the fit is examined in detail, the residuals indicated some curvature in the spectra above 2 keV (Fig. 7.4).

Clearly, the degree of curvature observed at high energies will depend on how the soft continuum emission is modelled. Replacing the low-energy thermal component with a power-law did not eliminate the high-energy curvature. In addition, the quality of the fits were worse ($\chi^2_{\nu} > 1.1$), and the models still required a high level of cold absorption.

Gradual flattening of the power-law toward higher energies has been observed in some other NLS1, and can be a quality attributed to a dominant reflection component (e.g. Fabian & Vaughan 2003) or partial-covering (Holt et al. 1980). While partial-covering has been relatively successful in describing the X-ray spectra of 1H 0707–495 (Boller et al. 2002) and IRAS 13224–3809 (Boller et al. 2003), the situation is more ambiguous in PHL 1092 due to the more modest statistics and the absence of a characteristic sharp spectral drop at energies above 7.1 keV (depending on the ionisation state of iron). We considered an absorption model by fitting the spectrum with a power-law plus edge. While the fit to the high-energy spectrum was good, the overall fit, including the soft X-ray components, was unacceptable ($\chi^2_{\nu} = 1.22$).

A reflection dominated spectrum has also been suggested for 1H 0707–495 (Fabian et al. 2002) and IRAS 13224–3809 (Boller et al. 2003), as well as other NLS1 (Ballan-

tyne et al. 2001). To test the reflection spectrum hypothesis a Gaussian profile was added to the fit to emulate an iron emission line. The improvement to the overall fit was significant ($\Delta\chi^2 = 14$ for the addition of 3 free parameters). The observed spectra can be described by a MCD plus power-law continuum, with warm absorption as well as a strong reflection component, all of which is modified by an amount of neutral absorption which is consistent with the Galactic column ($\chi^2 = 245.0/257$ dof; Fig. 7.5; model (a) in Table 7.2). The temperature at the inner disc radius is 114 ± 4 eV. The power-law has a photon index of 2.55 ± 0.11 . The absorption line is defined by $E = 1.43 \pm 0.04$ keV, $\sigma = 133_{-37}^{+42}$ eV, and $EW = -82_{-22}^{+19}$ eV. The reflection component is modelled by a Gaussian profile with $E \approx 6.9$ keV, $\sigma \approx 2$ keV, and $EW \approx 5$ keV. Other models for the reflection component (e.g. `diskline`, `laor`, `pexrav`) were also effective in handling the high-energy curvature. In these cases the lines were slightly weaker ($EW = 2.5 - 4$ keV); however, the quality of the data did not justify the use of these more complicated reflection models. The very strong iron line suggested for this PHL 1092 observation seems unphysical, and we will address this issue in Section 7.5.

The average $0.3 - 7.2$ keV unabsorbed flux is 1.91×10^{-12} erg cm $^{-2}$ s $^{-1}$ (1.78×10^{-12} erg cm $^{-2}$ s $^{-1}$ in the $0.3 - 2$ keV band), corresponding to an observed luminosity of 8.8×10^{44} erg s $^{-1}$. During the 18-day *ROSAT* HRI monitoring campaign of PHL 1092, BBFR measured a $0.2 - 2$ keV luminosity between $0.5 - 7.5 \times 10^{45}$ erg s $^{-1}$. Extrapolating our best-fit model from 0.3 keV to 0.2 keV, we estimate an average $0.2 - 2$ keV luminosity of 1.1×10^{45} erg s $^{-1}$.

In comparison with the *ASCA* luminosities reported by Vaughan et al. (1999; after correcting for the different cosmology which was assumed), we note that the intrinsic $0.6 - 10$ keV luminosity is about 12% higher during the *XMM-Newton* observation. However, in the $0.6 - 2$ keV band the *XMM-Newton* observation is $\approx 67\%$ brighter, whereas the $2 - 10$ keV luminosity is about 60% dimmer. The relative change in the various X-ray bands suggests long-term spectral variability in PHL 1092; however, the significance of this result cannot be tested without knowledge of the flux uncertainties in the *ASCA* data.

The broad-band continuum could be modelled equally well with a MCD plus a broken power-law above ~ 2 keV ($\Gamma_1 \approx 2.7$, $\Gamma_2 \approx 1.4$, $E \approx 3.1$ keV), and a ~ 1.4 keV absorption line ($\chi^2 = 245.4/258$ dof). However, it is difficult to understand the physical significance of the high-energy break. Fit parameters for three of the best-fit models are shown in Table 7.2 for comparison. It is apparent from Table 7.2 that the low-energy spectrum is better fit with a blackbody component rather than a power-law.

7.3.3 The true soft-excess and the need for high-energy curvature

When fitting the $3 - 7.2$ keV ($4.2 - 10$ keV rest frame) spectrum and extrapolating downward in energy, as was done for Fig. 7.2, there is evidence for an incredibly extreme soft-excess component, but no support for high-energy curvature. However, the need for high-energy curvature is seen when the broad-band spectrum is modelled in full. The simple power-law plus blackbody fit is significantly improved when a third

Table 7.2: Spectral fits to the 0.3 – 7.2 keV (0.4 – 10 keV rest frame) EPIC data. The two best-fits are models (a) MCD plus power-law continuum plus listed features, and (b) MCD plus broken power-law and listed features. Model (c) is the best-fit Comptonisation continuum model shown for comparison. Columns (4) to (7) are related to the continuum model: kT is the thermal temperature at the innermost disc radius; Γ_1 and Γ_2 are the photon indices of the power-law components (two photon indices are required in the case of a broken power-law); E_{brk} is the energy at which the photon index changes between Γ_1 and Γ_2 in the broken power-law model. Columns (8) to (10) are the absorption line components: line energy, width, and equivalent width (E , σ , EW , respectively), and columns (11) to (13) are the emission line components (best-fit values): line energy, width, and equivalent width (E , σ , EW , respectively). All models have been modified by line-of-sight Galactic absorption ($3.6 \times 10^{20} \text{ cm}^{-2}$).

(1) Model	(2) χ^2 (dof)	(3) N_{H} (10^{20} cm^{-2})	(4) kT (eV)	(5) Γ_1	(6) Γ_2	(7) E_{brk} (keV)	(8) E (keV)	(9) σ (eV)	(10) EW (eV)	(11) E (keV)	(12) σ (keV)	(13) EW (keV)
(a)	0.95 (257)	< 0.03	114 ± 4	2.55 ± 0.11	–	–	1.43 ± 0.04	133^{+42}_{-37}	-82^{+19}_{-22}	6.9	2	5
(b)	0.95 (258)	< 0.03	112^{+2}_{-5}	$2.74^{+0.15}_{-0.11}$	$1.49^{+0.28}_{-0.32}$	$2.25^{+0.40}_{-0.31}$	1.43 ± 0.04	144^{+41}_{-37}	-91^{+21}_{-22}	–	–	–
(c)	1.07 (257)	6.6 ± 0.2	–	4.64 ± 0.12	1.80 ± 0.26	1.88 ± 0.11	1.28 ± 0.06	300^{+33}_{-28}	-197^{+7}_{-5}	7.2	0.71	0.52

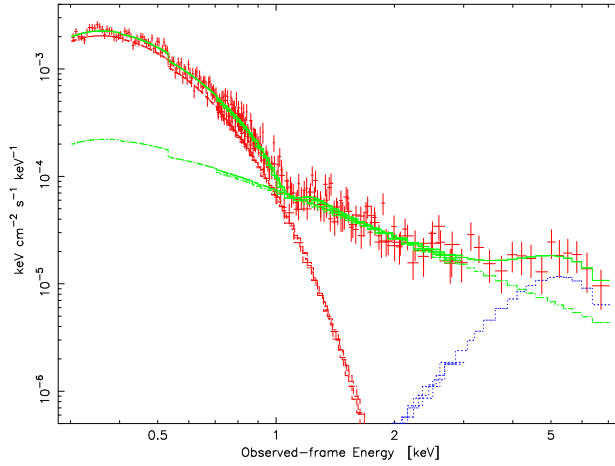


Figure 7.5: The unfolded model applied to the EPIC pn data. The strong, broad emission line dominates the high-energy spectrum leading to the hypothesis that the spectrum is reflection dominated.

component is introduced. Success is obtained when the simple continuum model is modified with either a strong, broad ~ 2 keV Gaussian profile, or a high-energy break in the power-law, or a strong, broad iron fluorescence line. We attempt to demonstrate the curvature in the high-energy spectrum on a more basic level.

The 2.5 – 4 keV rest frame data were fitted with a single absorbed power-law ($\Gamma \approx 2.6$). While the photon index is steep compared to what is normally measured in AGN it is not atypical of NLS1-type objects (e.g. Brandt et al. 1997; Porquet et al. 2004). The 2.5 – 4 keV region was selected because it was the region most unlikely to have a significant contribution from the soft-excess or possible line emission, based on the general knowledge of AGN X-ray spectra. The fit was then extrapolated to lower and higher energies as seen in Fig. 7.6 (note the *rest frame* energy axis). The extrapolation to higher energies is clearly poor indicating that there is a change in the spectral slope somewhere between 2.5 – 10 keV (rest frame). The extrapolation to lower energies is quite reasonable down to 1.5 keV (rest frame), at which point there is a rather dramatic upturn in the residual, likely marking the *true* onset of the soft-excess. Pounds & Reeves (2002) examine the soft-excess in a small sample of Seyfert 1 galaxies. One of their conclusions is that the onset of the soft-excess is related to the 2 – 10 keV luminosity, such that in more luminous objects the soft-excess originates at higher energies. Comparing PHL 1092 to their sample (correcting for the different cosmology), we determined that a soft-excess starting at 1.5 keV (rest frame) in PHL 1092 is precisely where the onset is expected.

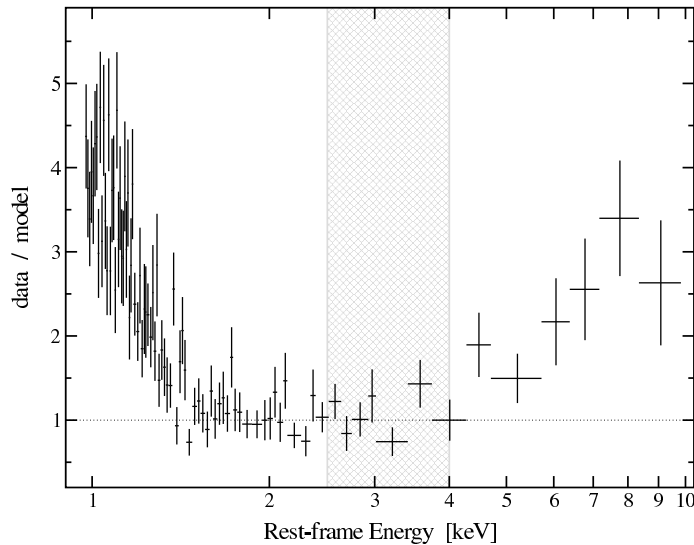


Figure 7.6: The residuals resulting from fitting the rest frame 2.5 – 4keV pn data (shaded region) with an absorbed power-law, and extrapolating to higher and lower energies. The data have been binned up for display purposes only. Note that the energy axis is given in the rest frame.

7.4 Variability properties

7.4.1 Extreme X-ray variability

Light curves from the two *XMM-Newton* observations of PHL 1092 are displayed in Fig. 7.7; July 2000 on the left side, and January 2003 on the right (hereafter GT and AO2, respectively). The 0.3 – 1.4 keV (0.4 – 2 keV rest frame) light curve during the GT observation shows periods of rapid flux drops and periods of relative quiescence. Overall, the X-ray intensity diminishes by nearly 70% during the 26 ks observation. During the AO2 observation the average count rate is about twice as high as during the GT observation. The 0.3 – 1.4 keV light curve¹ again exhibits a diminishing intensity from the start of the observation to the end. However, during the second observation, the flux drop is more gradual. The peak intensity falls by about 50% over the first 23 ks.

The most rapid event during the AO2 observation occurs during the final 5 ks. After reaching a minimum intensity at about 23 ks, the flux suddenly rises by $\sim 30\%$, and remains there to the end of the exposure. Averaging over two low and two high data points in this event (1200 s on each side), the change in the rest frame count rate is $0.12 \text{ count s}^{-1}$ in 860 s. Adopting the average luminosity discussed in the previous section to determine a conversion factor between count rate and flux, we find that the event corresponds to a luminosity change of $\Delta L = 2.0 \times 10^{44} \text{ erg s}^{-1}$. The luminosity

¹Including data above 1.4 keV does not contribute significantly to the total count rate; however background flaring becomes a factor resulting in gaps in the light curves

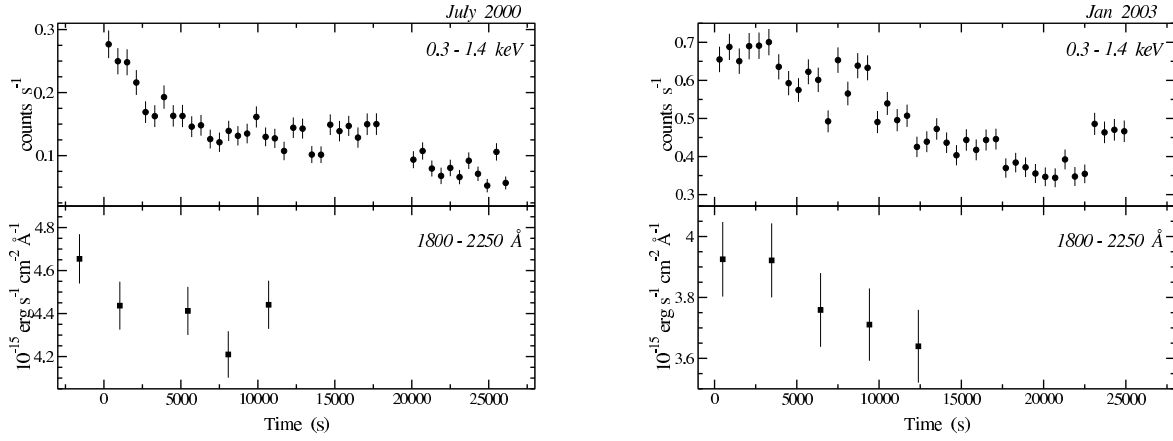


Figure 7.7: On the left side are the light curves corresponding to the July 2000 (GT) observation of PHL 1092. On the right side are the January 2003 (AO2) light curves. In the upper panels on both sides are displayed the variability in the 0.3 – 1.4 keV range ($\sim 0.4 - 2$ keV in the rest frame; 600 s bins). In the lower panels on both sides are the UVW2 light curves from each observation (1800 – 2250 Å observed frame; $\sim 1290 - 1600$ Å rest frame; 2300 s exposures during GT, and 2640 s exposures during AO2).

rate of change is $\Delta L/\Delta t \approx 2.3 \times 10^{41} \text{ erg s}^{-2}$. Quantifying this rate of luminosity change in terms of a radiative efficiency, $\eta \gtrsim 4.8 \times 10^{-43} \Delta L/\Delta t$, (Fabian 1979), we calculate $\eta \gtrsim 0.11$. The measured value of η is consistent with that expected from a Kerr black hole, but it exceeds the efficiency limit for a Schwarzschild black hole. While this is the most rapid event measured during this observation, BBFR found that, along with giant-amplitude flares, smaller amplitude flaring events were also rather common in PHL 1092 during periods of relative low flux (see Figure 1 of BBFR).

7.4.2 Simultaneous UV variability

An interesting discovery from this analysis is the simultaneous UV fluctuations of PHL 1092 which may be apparent at both epochs (Fig. 7.7 lower panels). Fitting a constant to both UV light curves results in $\chi^2_{\nu} = 2.01$ and 1.12 for the GT and AO2 observations, respectively; indicating variability at the $> 90\%$ and $\sim 66\%$ confidence levels. While not statistically significant, the UV light curves are short (~ 3 hours), not well-sampled, and of modest signal-to-noise (uncertainties on the level of 5%). Despite these observational constraints, variability trends are seen which appear consistent with the variability detected in the X-rays (more so during AO2). In addition, these short UV light curves are in contrast to what has been observed in the OM light curves of other NLS1 which normally show quite constant UV variability curves (e.g. Chapters 3, 6, 8). Unfortunately, relative photometry, to test the reliability of the UV light curves in Fig. 7.7, is not possible due to the method in which the OM observation was carried out. As described by Mason et al. (2002), in the default OM imaging mode there are five exposures made up of two image windows each. While one

Table 7.3: Long-term differences in the UV fluxes of identified OM sources. UVW2 flux densities are given in units of $\times 10^{-15}$ erg cm $^{-2}$ s $^{-1}$ Å $^{-1}$.

Object	Classification	GT Flux	AO2 Flux	Change
HD 10214	G5 star	307 ± 1	325 ± 1	+6%
UGC 00649	Sab galaxy	30.7 ± 0.3	33.2 ± 0.3	+8%
PHL 1092	AGN	4.43 ± 0.05	3.79 ± 0.05	-14%

window remains fixed on the central X-ray source during all five exposures (PHL 1092 in our case), the second window is moved across the CCD in order to maximize the field-of-view coverage. As a result, there is minimum overlap in the different windows, and no potential standard star is observed more than once.

Focusing on the AO2 observation, it may appear that the UV and X-rays are undergoing a gradual decline in flux during the first 13 ks. During this time the X-ray count rate drops by about 40%, whereas the UV flux drops by an average of 7% with an upper limit of 13% (not making any corrections for host galaxy and emission-line contamination). Without a longer base line on both light curves (and a higher signal-to-noise UV light curve) it is impossible to discuss how significant this result is, or if the two processes are physically connected (e.g. reprocessing, pivoting power-law, partial-covering).

There also appears to be long-term variability in the UV to X-ray spectral slope between the two epochs. In a rough approximation, utilising the values from the light curves, we see that the fraction of the mean X-ray count rate over the mean UV flux ($\div 10^{-15}$) has changed from 0.030 ± 0.001 during the GT observation, to 0.133 ± 0.002 during AO2. We examined whether the change in the UV flux is due to instrumental effects by making note of the UV fluxes of two other objects which were observed at both epochs (Table 7.3). One of these objects is a G5 star (HD 10214); hence its brightness should be rather stable over the ~ 2 -year period. As we see from Table 7.3 the UV flux in these comparison objects does change, and this could be associated with changes in the intrinsic luminosity of the sources or instrumental effects. However, the UV flux change in PHL 1092 is larger and opposite to that observed in the other two objects; hence the variability appears to be intrinsic to PHL 1092. A typical α_{ox} derivation is difficult to accomplish without making some assumptions about the UV spectral slope; hence it will not be calculated here.

In general, the variability is impressive for an object with an X-ray luminosity of $\sim 10^{45}$ erg s $^{-1}$. Moreover, the rapid variability seems to extend to lower energies.

7.4.3 Spectral variability

Comparing the *ASCA* and *XMM-Newton* observations there appears to be long-term X-ray spectral variability. Considering the OM and EPIC fluxes from the two *XMM-Newton* observations there also appears to be significant variability in the UV/X-ray spectral slope. However, examining short-term spectral variability within a single

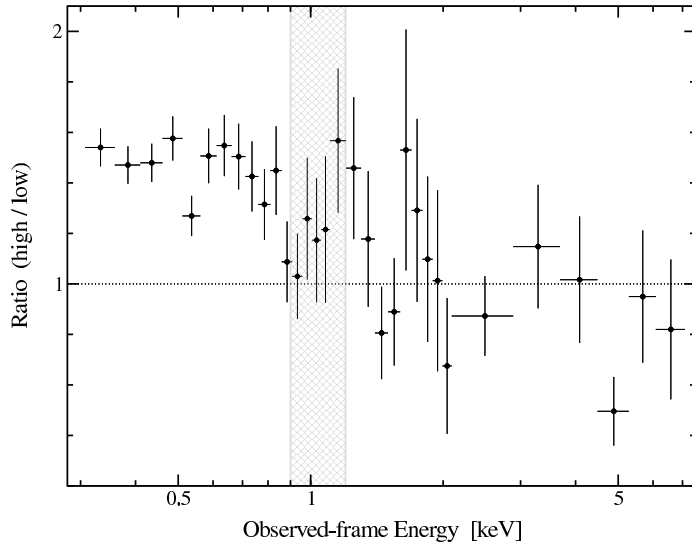


Figure 7.8: The EPIC pn background-subtracted ratio spectrum (high/low). To compare the spectrum to a constant a dotted-line is drawn in at high/low = 1. While the flux difference in the soft emission is remarkable, the variability above 2 keV is insignificant. The shaded region marks the approximate position of the ~ 1.4 keV absorption feature based on Fig. 7.3.

observation is difficult given the degree of high-energy background flaring during AO2. We search for flux related spectral variability, by constructing and comparing a high-flux spectrum and a low-flux spectrum. The high-flux state corresponded to all events with a count rate greater than 0.5 count s^{-1} in Fig. 7.7 (right panel). This was roughly equivalent to selecting all events prior to ~ 12 ks. The low-flux state was made up of all remaining events. In Fig. 7.8 we have plotted the ratio between the high-flux and low-flux background-subtracted spectra. Note that the ratio spectrum only goes to ~ 6.5 keV, as the low-flux spectrum is background dominated above this energy.

For comparison to a constant, a line is drawn at a value of high/low = 1. The variability is obvious. At low-energies, < 1 keV (1.4 keV rest frame), the variability is remarkable, on the order of 50%. However, at energies above ~ 1.4 keV (2 keV in the rest frame), Fig. 7.8 shows no indication of significant variability. Despite the extreme soft X-ray variability seen in Fig. 7.7, it would seem that the hard X-rays are not particularly variable.

The shaded region in Fig. 7.8 marks the approximate position of the ~ 1.4 keV absorption feature based on Fig. 7.3. Within the uncertainties, the variability in this region is weak, and most likely related to the underlying continuum rather than the absorption line itself.

7.5 Discussion

7.5.1 General findings

The main results of this study are listed below.

- (1) The soft-excess can be best-fit with a MCD (or blackbody) modified by Galactic absorption. An absorption feature was detected at $E \approx 1.4$ keV ($EW \approx -82$ eV). The emission gradually flattens as the energy increases, introducing curvature to the high-energy (> 2 keV) spectrum. This curvature can be modelled empirically with a Gaussian profile ($E \approx 6.9$ keV, $EW \approx 5$ keV) or a broken power-law ($\Gamma_1 \approx 2.7$, $\Gamma_2 \approx 1.4$, $E \approx 3.1$ keV in the rest frame).
- (2) Comparing the high-flux and low-flux spectra suggests significant short-term spectral variability. While the soft component is remarkably variable, the hard component shows no considerable variability. Long-term X-ray spectral variability is also suggested by a simple comparison between the *ASCA* and *XMM-Newton* luminosities in different energy bands. In addition, long-term fluctuations in the X-ray/UV spectral slope are indicated by comparing the simultaneous UV and X-ray fluxes for each *XMM-Newton* observation.
- (3) The UV and soft X-ray light curves from the two separate *XMM-Newton* observations show extraordinary short-term variability for such a luminous quasar ($\sim 10^{45}$ erg s $^{-1}$). Radiative efficiency calculations during the AO2 observation exceed the limit for accretion onto a Schwarzschild black hole.

7.5.2 The ~ 1.4 keV absorption feature

An absorption line at ~ 1.4 keV has been detected in a number of NLS1 (e.g. Leighly 1999b; Vaughan et al. 1999; Boller et al. 2003). Leighly et al. (1997) examined the possibility that such features were O VII-O VIII edges, significantly blueshifted due to relativistic outflows. On the other hand, Nicastro et al. (1999) explain this type of absorption feature as a blend of resonant absorption lines, mainly due to Fe L, in a highly ionized warm absorber. A strong, steep, soft-excess is a requisite for the Nicastro et al. interpretation, which appears relevant in PHL 1092. To the best of our knowledge, PHL 1092 is the most luminous, NLS1 type object, in which possible Fe L absorption has been detected.

The absorption feature in PHL 1092 was not detected during the *ASCA* observations. We simulated *ASCA* SIS data by using the *XMM-Newton* model with the same number of counts that were obtained during the real *ASCA* observation. In this case, the absorption line could have been detected, although it was not clearly seen in the residuals ($\Delta\chi^2 \approx 16$ for 3 additional free parameters). This could be indicative of long-term variability in the absorption feature, but we cannot dismiss the possibility of normalisation and/or profile changes in the low-energy continuum which will alter the apparent strength of any constant line features. However, since the ionising X-ray

luminosity in PHL 1092 is so highly variable it is possible to consider that the strength of the ~ 1.4 keV feature is also time variable.

As mentioned, during the *ASCA* observations the total intrinsic 0.6 – 10 keV luminosity was about 10% lower than during the AO2 observation. Variability on this scale is typical for PHL 1092 in the course of hours. What may be more relevant here is the strength of the soft-excess component. During the *ASCA* observations the soft-to-total intrinsic luminosity ratio ($l = L_{0.6-2 \text{ keV}}/L_{0.6-10 \text{ keV}}$) was $l_{ASCA} \approx 0.56$, whereas during AO2 the ratio was $l_{AO2} = 0.84 \pm 0.04$ (uncertainties were not published for the *ASCA* observation). The strength of the soft-excess could be an important consideration if the ~ 1.4 keV feature is indeed variable in PHL 1092.

7.5.3 The rapid flux variability

The large-amplitude and rapid X-ray variability is impressive for a quasar of this luminosity, but more extreme behavior has been observed in this object before. It was during the *ROSAT* HRI monitoring campaign that BBFR critically examined the underlying assumptions in the derivation of the radiative efficiency limit. The standard derivation assumes a uniform, spherical emission region with the release of radiation localized at its centre. It assumes that relativistic Doppler boosting and light bending are unimportant. Therefore, it is more than likely that the high and sometimes extreme values of the radiative efficiency measured in PHL 1092 are due to one or more of these standard assumptions being violated. The spectral properties discussed in Section 7.3, in particular the large equivalent width of the iron line, may suggest that light bending effects are considerable in this object (see next section).

A new development, however, is the apparent simultaneous UV variability, and *lack of* hard X-ray variability. Without a high quality UV spectrum of PHL 1092, it is difficult to determine what could be the driving component responsible for the UV variability. Assuming that the UV spectrum of PHL 1092 is similar to that of I Zw 1 (Laor et al. 1997), another strong iron emitting NLS1, we can hypothesize that the source of the variability is continuum since line-emission is rather modest in this spectral region (1290 – 1600 Å intrinsic). Therefore, it is unlikely that the continuum variations are much stronger than those seen in Fig. 7.7 (i.e. the continuum variability is probably not suppressed by line emission). Any models to be considered must, therefore allow for rapid, large-amplitude X-ray variability and weak UV variability. Currently, such models cannot be meaningfully discussed without a longer base line and higher quality light curves.

7.5.4 Light bending model

A number of empirical models can be used to fit the high-energy curvature successfully, for example: a reflection-dominated spectrum, a high-energy broken power-law, or a broad 2 keV emission line in addition to the continuum. The problem with the latter two models is that they lack a clear physical interpretation. Recently, it was demonstrated how a spectrum could be reflection dominated via light bending ef-

fects (Martocchia, Karas & Matt 2000; Fabian & Vaughan 2003; Miniutti et al. 2003; Miniutti & Fabian 2004). Uttley et al. (2003) consider a strong reflection component enhanced by light bending effects in describing the spectrum of the NLS1 NGC 4051 in its extended low-flux state.

The very strong iron line ($EW \approx 2.5 - 5$ keV depending on the adopted model) suggested for this PHL 1092 observation seems highly unphysical, and in contrast to the general belief that the overall strength of the line diminishes with luminosity (e.g. Reeves & Turner 2000; but also see Porquet & Reeves 2003). However, the large equivalent width can be understood through light bending. Theoretical modelling by Dabrowski & Lasenby (2001) demonstrate that in a maximally rotating black hole, with the primary source located off the rotation axis, and the observer at an inclination of 60° , fluorescence line equivalent widths as high as ~ 5.5 keV could be realised. Interestingly, Miniutti & Fabian (2004) show that the power-law component could be significantly more variable than the reflection component which could help explain the apparently constant high-energy X-ray emission in the presences of the highly variably low-energy X-ray emission. In addition, the high values that have been measured for the radiative efficiency in PHL 1092 on numerous occasions can also be understood if gravitational light bending effects are accounted for.

7.5.5 Alternatives to light bending

We have already discussed that high-energy curvature could be an indication for partial covering. In addition, much of the long-term spectral variability could be explained in terms of partial-covering. However, a basic partial covering model is simply not a good fit to the current spectral data and the data quality do not warrant the use of more advanced models.

With respect to the amazing variability it is natural to consider relativistic beaming due to jet emission. PHL 1092 is radio-quiet, and to the best of our knowledge, only detected in the sensitive NRAO VLA Sky Survey (NVSS; Condon et al. 1998) at 1.4 GHz at the 1 mJy level. Furthermore, the spectra at higher energies are not consistent with jet emission.

There are, of course, other possibilities that could produce some of the features observed in PHL 1092 (e.g. steep spectrum, extreme η , short-lived flares). For example, an intervening medium, such as: ions (e.g. Di Matteo et al. 1997), magnetic fields (e.g. Merloni & Fabian 2001), bulk motion of flaring material (Reynolds & Fabian 1997; Beloborodov 1999), or a combination could explain a number of the effects seen in PHL 1092 over the years.

7.6 Conclusions

PHL 1092 has been long known for its extreme variability and large luminosity. This most detailed X-ray observation to date revealed interesting spectral features which certainly warrant a deeper look. The complicated mixture of spectral and timing properties can be explained *simultaneously* if we consider light bending effects. In

addition, the possibly correlated soft X-ray/UV variability demonstrates the potential for fruitful variability and reverberation mapping studies of PHL 1092.

Chapter 8

The narrow-line quasar NAB 0205+024 observed with *XMM-Newton*

8.1 Introduction

Narrow-line Seyfert 1 galaxies (NLS1) offer an extreme view of the Seyfert 1 phenomenon. For example, these objects show:

- The narrowest permitted optical lines, strongest optical Fe II emission, and weakest [O III] emission (e.g. Osterbrock & Pogge 1985; Boroson & Green 1992; Grupe 2004).
- Strong soft X-ray excesses (e.g. Boller, Brandt & Fink 1996; Leighly 1999a; Vaughan et al. 1999) above a relatively steep hard power-law (e.g. Brandt, Mathur & Elvis 1999);
- Large-amplitude X-ray variations on hourly time scales (e.g. Boller, Brandt & Fink 1996; Leighly 1999b).
- Weak or negligible optical variability (e.g. Klimek, Gaskell & Hedrick 2004).

Many of the properties can be explained in terms of a high accretion rate and relatively low-mass black hole (e.g. Sulentic et al. 2000; Boroson 2002; Grupe 2004). These characteristics are not exclusive to lower-luminosity AGN (i.e. Seyfert 1s), but are also seen in some quasar-type objects. The most famous of these *narrow-line quasars* is the prototype I Zw 1, but the class also includes members such as PHL 1092, E 1346+266, IRAS 13349+2438, and the *Neta A. Bahcall* object NAB 0205+024 (Bahcall, Bahcall & Schmidt 1973).

NAB 0205+024 (Mrk 586; $z = 0.155$) has been the focus of previous X-ray studies with *ASCA* (e.g. Fiore et al. 1998), and *ROSAT* (Fiore et al. 1994). The strong soft-excess and rapid variability (by factors of two on time scales of hours) have made it an important object to study the nature of NLS1 behaviour in luminous narrow-line quasars.

In this Chapter we discuss the X-ray analysis of NAB 0205+024 as observed with *XMM-Newton*. The X-ray brightness of NAB 0205+024 (compared to other similar objects) affords us the opportunity to study the NLS1 phenomenon in a quasar with relatively high signal-to-noise.

8.2 Observations and data reduction

NAB 0205+024 was observed with *XMM-Newton* (Jansen et al. 2001) for 50 ks on 2002 July 23 (revolution 0480). During this time the EPIC pn (Strüder et al. 2001) and MOS (MOS1 and MOS2; Turner et al. 2001) cameras, as well as the Optical Monitor (OM; Mason et al. 2001) and the Reflection Grating Spectrometers (RGS1 and RGS2; den Herder et al. 2001) collected data. The EPIC pn and MOS2 cameras were operated in full-frame mode and utilised the thin filter. The MOS1 camera was operated in timing mode, and the data will not be included in the current analysis.

The Observation Data Files (ODFs) were processed to produce calibrated event lists using the *XMM-Newton* Science Analysis System (SAS v6.0.0). Unwanted hot, dead, or flickering pixels were removed as were events due to electronic noise. Event energies were corrected for charge-transfer losses, and EPIC response matrices were generated using the SAS tasks ARFGEN and RMFGEN. Light curves were extracted from these event lists to search for periods of high background flaring. High-energy background flaring was substantial. The total good exposure times selected for the pn and MOS2 were 20388 s and 31545 s, respectively. The source plus background photons were extracted from a circular region with a radius of 35", and the background was selected from an off-source region with a radius of 50" and appropriately scaled to the source region. Single and double events were selected for the pn detector, and single-quadruple events were selected for the MOS2. Pile-up effects were determined to be negligible in the time-averaged data. However, there was mild pile-up during a ~ 4 ks period when the source flux increased by 50% (Section 8.4.1). As a consistency check the inner 5" of the source extraction region was removed, thus correcting the pile-up effect during the flare. The step proved to be unnecessary, as it had little effect on the spectral variability results (Section 8.4.2). The total numbers of source plus background counts collected in the 0.3 – 10 keV range by the pn and MOS2 instruments were 68372 and 29354, respectively. The total numbers of counts collected from the scaled background region were 1187 for the pn, and 1132 for the MOS2. The *XMM-Newton* observation provides a substantial improvement in spectral quality over the 51.8 ks ASCASIS exposure (118.6 ks duration) in which ≈ 18130 counts were collected (Leighly 1999b).

The RGS were operated in standard Spectro+Q mode. The first-order RGS spectra were extracted using the SAS task RGSPROC, and the response matrices were generated using RGSRMFGEN. The total exposure times utilised for the analysis were 46078 s and 44717 s for the RGS1 and RGS2, respectively. The total number of source counts in the 0.35 – 1.5 keV range were approximately 4915 (RGS1) and 4708 (RGS2).

The OM was operated in imaging mode for the entire observation. In total, thirty-one 1000 s images were taken in three filters: 21 in U (3000 – 3900 Å), and 5 in both

B (3900 – 4900 Å) and $UVW2$ (1800 – 2250 Å). The average apparent magnitude in each filter was $U = 14.614 \pm 0.002$, $B = 15.701 \pm 0.004$, and $UVW2 = 14.126 \pm 0.011$.

8.3 Spectral analysis

Each of the EPIC spectra was compared to the respective background spectrum to determine the energy range in which the source was reasonably detected above the background. The source was detected above the background up to an observed energy of ~ 10 keV, and ~ 7 keV in the pn and MOS2 data, respectively. The MOS data were ignored below 0.5 keV due to the uncertainties in the low-energy redistribution characteristics of the cameras (Kirsch 2003). Therefore, the pn data between 0.3 – 10 keV and the MOS2 data between 0.5 – 7 keV were utilised during the spectral fitting, but the residuals from each instrument were examined separately to judge any inconsistency. In addition the RGS data between 0.35 – 1.5 keV were also examined.

The source spectra were grouped such that each bin contained at least 20 counts. Spectral fitting was performed using *XSPEC* v11.3.0 (Arnaud 1996). Fit parameters are reported in the rest frame of the object, although the figures remain in the observed frame. The quoted errors on the model parameters correspond to a 90% confidence level for one interesting parameter (i.e. a $\Delta\chi^2 = 2.7$ criterion). Luminosities were derived assuming isotropic emission. The Galactic column density toward NAB 0205+024 is $N_{\text{H}} = 3.51 \times 10^{20} \text{ cm}^{-2}$ (Dickey & Lockman 1990). A value for the Hubble constant of $H_0 = 70 \text{ km s}^{-1} \text{ Mpc}^{-1}$ and a standard cosmology with $\Omega_M = 0.3$ and $\Omega_\Lambda = 0.7$ was adopted.

8.3.1 The broad-band X-ray continuum

A single power-law with Galactic absorption was a poor fit to the EPIC data between 0.3 – 10 keV ($\chi^2 = 1937.7/738$ dof). The higher statistics in the low-energy range dominate the fit resulting in large residuals at higher energies which demonstrates the need for multiple continuum components. Fitting only the EPIC data above 2 keV with an absorbed power-law resulted in a good fit ($\chi^2 = 272.4/302$ dof) and demonstrated agreement in the photon indices measured by each instrument ($\Gamma_{\text{pn}} = 2.26 \pm 0.07$ and $\Gamma_{\text{MOS2}} = 2.20 \pm 0.10$). Extrapolating this model to lower energies revealed a strong soft-excess above the power-law continuum (Fig. 8.1).

To investigate the nature of the continuum emission additional components were included in the basic power-law fit to model the soft-excess. The data from each instrument were modelled separately in order to compare the results. In the case of the RGS, the high-energy model component (i.e. the power-law) was kept fixed to the pn values.

To fit the broad-band continuum a number of models were used including (i) a blackbody plus power-law, (ii) a double power-law and, (iii) a broken power-law. The addition of a second continuum component was a substantial improvement to the initial power-law fit; the best fit was obtained with model (i) (Fig. 8.2). In this case the blackbody temperature was $kT \approx 120 \text{ eV}$, and the intrinsic absorption was

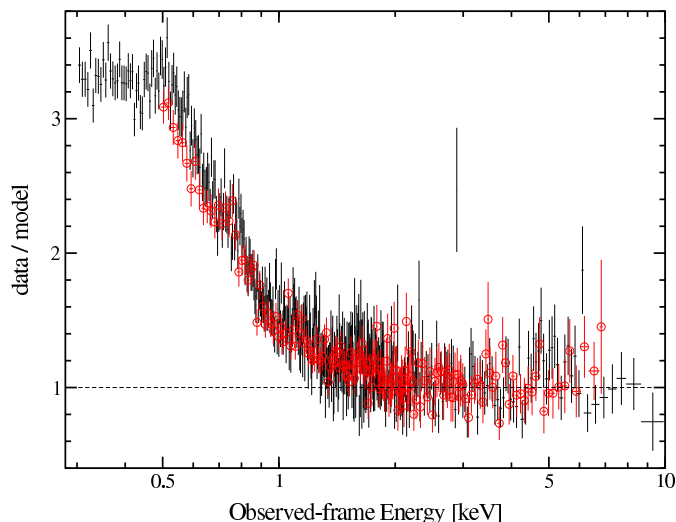


Figure 8.1: The ratio (data/model) resulting from fitting an absorbed power-law ($\Gamma_{pn} = 2.26 \pm 0.07$ and $\Gamma_{MOS2} = 2.20 \pm 0.10$) to the 2 – 10 keV EPIC data and extrapolating to lower energies. The black crosses and red open circles are the pn and MOS2 residuals, respectively. The apparently “wild” single data point at $E \approx 3$ keV is less than 3σ above the ratio, and probably is just a statistical fluctuation. The data have been binned for display purposes.

negligible. The 0.3 – 10 keV flux and luminosity, corrected for Galactic absorption, were $8.6 \times 10^{-12} \text{ erg cm}^{-2} \text{ s}^{-1}$ and $6.2 \times 10^{44} \text{ erg s}^{-1}$, respectively. The 2 – 10 keV luminosity was $1.1 \times 10^{44} \text{ erg s}^{-1}$. In Table 8.1 the model parameters for each fit are given.

8.3.2 The RGS data

The RGS data were examined with finer energy bins to search for narrow absorption and emission features which may be expected from a warm medium in an AGN. The blackbody plus power-law continuum [model (i) in Table 8.1] was adopted. Within the uncertainties no strong narrow features were revealed. The most significant feature was a dip below the continuum at about 1 keV (see the lower panel of Fig. 8.2). Adding a Gaussian absorption profile to model this feature was an improvement to the RGS continuum model ($\Delta\chi^2 = 10.4$ for 3 additional free parameters). The line had an intrinsic energy, width, and equivalent width of $E = 1.19 \pm 0.03 \text{ keV}$, $\sigma = 30_{-15}^{+30} \text{ eV}$, $EW = -22.3_{-0.9}^{+0.7} \text{ eV}$, respectively. The measured energy is consistent with Fe L resonant absorption (e.g. Nicastro, Fiore & Matt 1999), but the strength of the feature is about five times weaker than predicted for an IRAS 13224–3809 type absorber (see Nicastro et al. for details). The reliability of the detection is questionable given that the absorption feature was not detected in either of the EPIC spectra. In addition, only the RGS2 is operational between $\sim 0.9 - 1.2 \text{ keV}$, due to a malfunctioning CCD

Table 8.1: X-ray continuum models. The data from each EPIC instrument were modelled separately, but the RGS1 and RGS2 data were fitted together. The superscript f marks the RGS parameters which are fixed to the best-fit pn values. The three continuum models, shown in column (1), are: (i) blackbody plus power-law, (ii) double power-law, and (iii) broken power-law. In column (2) we indicate the instrument used to collect the data, and in column (3) the fit quality (χ^2_ν) is given. Column (4) gives the measured intrinsic cold absorption. Column (5) is the temperature of the blackbody component. Columns (6) and (7) are the photon indices of the power-law components (two power-laws are required for models (ii) and (iii)). Column (8) is the energy at which the photon index changes between Γ_1 and Γ_2 in model (iii). All models have been modified by line-of-sight Galactic absorption ($3.51 \times 10^{20} \text{ cm}^{-2}$).

(1) Continuum Model	(2) Instrument	(3) χ^2_ν (dof)	(4) N_{H} (10^{20} cm^{-2})	(5) kT (eV)	(6) Γ_1	(7) Γ_2	(8) E_{brk} (keV)
(i)	pn	1.04 (523)	< 0.3	121 ± 2	2.41 ± 0.04		
	MOS2	0.88 (209)	< 1.4	118^{+5}_{-6}	$2.37^{+0.06}_{-0.05}$		
	RGS	1.19 (313)	< 0.6	127 ± 4	2.41^f		
(ii)	pn	1.76 (523)	$5.85^{+0.08}_{-0.06}$		3.81 ± 0.16	1.54 ± 0.13	
	MOS2	0.88 (209)	15.9^{+9}_{-13}		$5.74^{+0.52}_{-1.45}$	$2.25^{+0.06}_{-0.21}$	
	RGS	1.41 (313)	< 1.9		3.16^{+17}_{-7}	1.54^f	
(iii)	pn	1.54 (523)	$6.65^{+1.44}_{-1.18}$		$3.74^{+0.12}_{-0.10}$	2.42 ± 0.05	1.38 ± 0.04
	MOS2	0.92 (209)	< 2.5		3.34 ± 0.06	2.39 ± 0.06	1.22 ± 0.08
	RGS	1.36 (313)	< 2.1		3.05^{+17}_{-7}	2.42^f	1.38^f

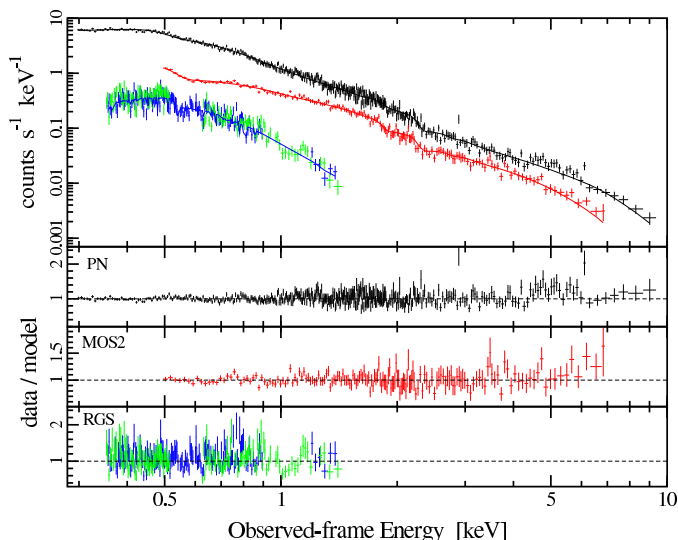


Figure 8.2: The best-fit continuum model (blackbody plus power-law) fitted to the XMM-Newton data. In the top panel the fit and data are shown for the pn (upper curve; black), MOS2 (middle curve; red), and RGS (lower curve; blue and green). In the remaining panels the fit residuals (data/model) are shown for each instrument.

in the RGS1 at this energy range. The feature could also be a calibration effect as the flux calibration in the RGS is known to be uncertain by about 5% across the RGS band (Pollock 2003).

8.3.3 A high-energy feature

Clearly visible in the pn spectrum at ~ 5 keV (top two panels of Fig. 8.2) is an excess in the residuals which could indicate the presence of an emission line. Indeed the addition of a Gaussian profile was a significant improvement to the pn 0.3 – 10 keV fit (i) from Table 8.1 ($\Delta\chi^2 = 20.3$ for 3 additional free parameters); however, the best-fit line energy of $E = 5.87^{+0.29}_{-0.27}$ keV was inconsistent with iron emission, and no other elements in this spectral range are expected to produce such a wide and strong line ($\sigma = 623^{+300}_{-237}$ eV; $EW = 515 \pm 6$ eV).

Since the excess is strongly concentrated to the red side of 6.4 keV (Fig. 8.3), relativistic effects were considered. The possibility that the emission feature arises from a disc around a Schwarzschild black hole (Fabian et al. 1989) was examined. The fit using the disc-line was comparable to the Gaussian profile ($\Delta\chi^2 = 20.3$ for 3 additional free parameters). The best-fit line energy was $E = 5.69^{+0.15}_{-0.10}$ keV with an equivalent width of $EW = 455 \pm 5$ eV. The shift of the line to energies lower than 6.4 keV suggests that gravitational redshift effects may be dominating the emission. Given that the best-fit line energy did not correspond to iron emission, we fixed the energy to 6.4 keV and refit the disc-line model by allowing the inner and outer disc

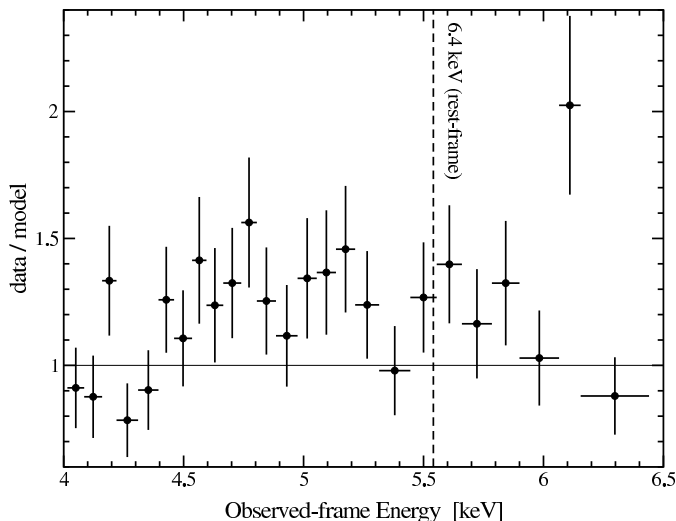


Figure 8.3: The *pn* residuals (*data/model*) in the intrinsic 4.6 – 7.5 keV range (a blow-up of the second top panel in Fig. 8.2). The dashed vertical line is the 6.4 keV rest energy.

radii to be free parameters. This fit was also acceptable ($\chi^2 = 525.8/519$ dof), and indicated that the disc-line was emitted from a small annulus between about $18-24 r_g$. An annular emission region could be realised if a specific region of the disc is being illuminated for some period of time (e.g. Iwasawa et al. 1999). Iron emission from an accretion disc around a Kerr black hole (Laor 1991) was also acceptable ($\Delta\chi^2 = 16.1$ for 3 additional free parameters). The line energy and inner radius were fixed at $E = 6.4$ keV and $R_{in} = 1.235 r_g$ (the innermost stable orbit around a Kerr black hole). In this case only a lower-limit for the outer radius was measured ($R_{out} > 14 r_g$). The best-fit line parameters are given in Table 8.2.

Recent observations of some Seyferts have revealed narrow emission lines at peculiar energies redward of 6.4 keV (Turner et al. 2002; Guainazzi 2003; Yaqoob et al. 2003; Turner et al. 2004). Dovčiak et al. (2004) explain these features as iron lines produced in a small range of radii by localised flares. The feature in NAB 0205+024 could also be fitted with a series of three emission lines with energies of $E \approx 5.45, 5.95, 6.59$ keV and unconstrained widths ($\Delta\chi^2 = 28.6$ for 9 additional free parameters). The lines were much stronger ($EW \approx 97-240$ eV) than the narrow lines discussed by the above authors which have typical equivalent widths of a few tens of eV. In addition, splitting the broad feature into three components was not required on a statistical basis.

A broad Gaussian emission profile was not statistically required by the MOS2 data; however the MOS2 data were consistent with the *pn* model. The broad feature was not detected by *ASCA*. Simulations of the *ASCA* observation using the *pn* model show that this was a signal-to-noise issue.

Table 8.2: The best-fit line model parameters to the broad-band pn spectrum. For each model the parameters given (as required) are: the power-law photon index (Γ); line energy (E); line width (σ); disc inclination (i); inner (R_{in}) and outer (R_{out}) disc radius in units of gravitational radii ($r_g = Gm/c^2$); power-law dependency on the disc emissivity (q); equivalent width (EW); flux (F) in units of $\times 10^{-14}$ erg cm $^{-2}$ s $^{-1}$. Parameters marked with the superscript f are fixed as leaving them free did not improve the fits.

Gaussian	$\chi^2_{\nu} = 1.01(520)$ $\Gamma = 2.47 \pm 0.02$ $E = 5.87^{+0.29}_{-0.27}$ keV $\sigma = 623^{+300}_{-237}$ eV $EW = 515 \pm 6$ eV; $F = 8.46$
Disc-line	$\chi^2_{\nu} = 1.01(519)$ $\Gamma = 2.45 \pm 0.03$ $E^f = 6.4$ keV $q^f = -2$; $R_{in} = 18^{+7}_{-12} r_g$; $R_{out} = 24^{+17}_{-6} r_g$ $i = 31^{+5}_{-11}$ degr $EW = 490 \pm 11$ eV; $F = 6.10$
Laor line	$\chi^2_{\nu} = 1.01(520)$ $\Gamma = 2.47 \pm 0.02$ $E^f = 6.4$ keV $q^f = 3$; $R_{in}^f = 1.235 r_g$; $R_{out} > 14 r_g$ $i = 37^{+9}_{-14}$ degr $EW = 868 \pm 10$ eV; $F = 9.13$

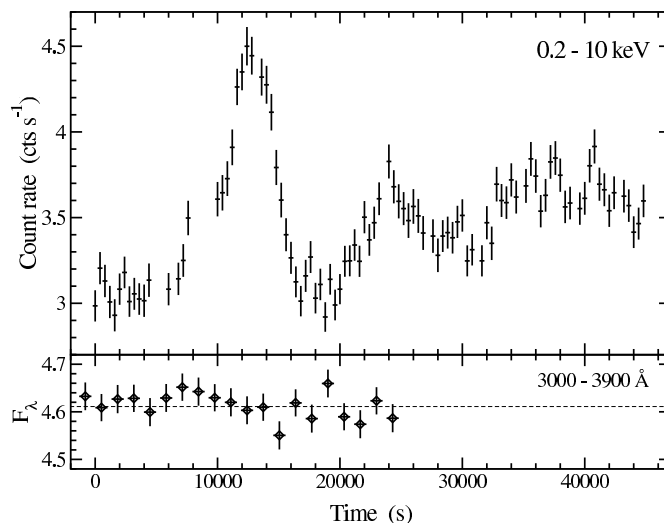


Figure 8.4: Top panel: The 0.2 – 10 keV light curve over the duration of the observation using 400 s bins. The time axis is defined from the start of the pn observation at 07:37:55 on 2002-07-23 UT. Bottom panel: The U-filter light curve obtained with the OM during the first ~ 25 ks of the observation. Flux-density units are $\times 10^{-15}$ erg cm $^{-2}$ s $^{-1}$ Å $^{-1}$. A dashed line is drawn at the average flux density.

8.4 Timing Analysis

8.4.1 X-ray and optical light curves

The 0.2–10 keV light curve of NAB 0205+024 is displayed in the top panel of Figure 8.4 (with 1σ error bars). Since the broad-band light curve is less sensitive to calibration uncertainties the data between 0.2–0.3 keV have been included. In addition, the light curve from the entire observation is shown since the source is sufficiently brighter than the background (by about a factor of ten), even during the background flaring. The average count rate is 3.49 ± 0.10 count s $^{-1}$. The most striking feature is a flaring event about 10 ks into the observation in which the broad-band count rate increases by $\sim 50\%$ in a few thousand seconds. Averaging over three data points during flare maximum at ~ 12.4 ks and the three lowest data points when the flare achieves minimum intensity at ~ 16.8 ks results in a count-rate change of 1.33 count s $^{-1}$ in 3800 s (rest frame). Model (i) from Table 8.1 is extrapolated down to 0.2 keV to estimate a 0.2 – 10 keV intrinsic luminosity of 7.74×10^{44} erg s $^{-1}$. Thus the calculated change in count rate corresponds to a luminosity change of $\Delta L = 2.96 \times 10^{44}$ erg s $^{-1}$. The luminosity rate of change is $\Delta L/\Delta t \approx 7.8 \times 10^{40}$ erg s $^{-2}$. Quantifying this rate of luminosity change in terms of a radiative efficiency, $\eta \gtrsim 4.8 \times 10^{-43} \Delta L/\Delta t$ (Fabian 1979), we calculate $\eta \gtrsim 0.037$. This is consistent with the efficiency of a Schwarzschild black hole.

A U-filter (3000–3900 Å) light curve was constructed from the OM data during the first ~ 25 ks of the observation (lower panel of Figure 8.4). In general, and in particular

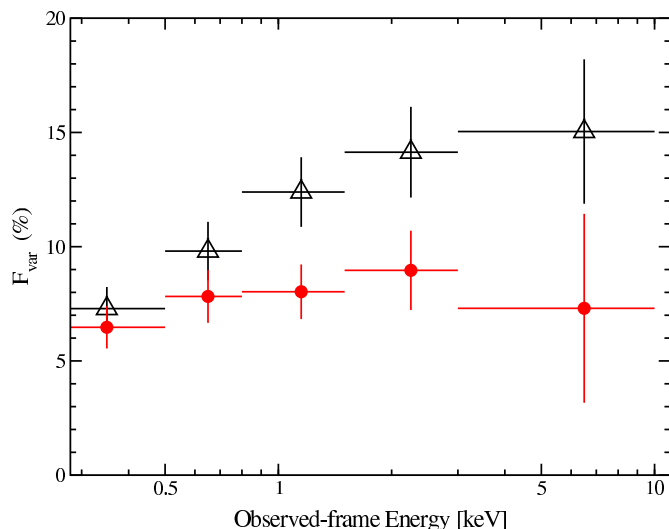


Figure 8.5: The rms spectra of NAB 0205+024 over the entire observation (open, black triangles) and excluding the flaring event between $\sim 10 - 15$ ks (red dots). F_{var} is calculated using light curves in 1000 s bins.

during the X-ray flare, the optical light curve shows no evidence of variability. A constant model fitted to the light curve was acceptable ($\chi^2_{\nu} = 0.9$). In addition, two shorter light curves covering ~ 5 ks each were obtained with the *B* (3900 – 4900 Å) and *UVW2* (1800 – 2250 Å) filters. Neither of these curves showed any variability ($\chi^2_{\nu} < 0.6$ for 4 dof in each filter).

8.4.2 Spectral variability

The fractional variability amplitude (F_{var} ; Edelson et al. 2002) was calculated twice (Fig. 8.5). Firstly, utilising data over the entire observation, and again while ignoring the data during the apparent flare ($\sim 10 - 15$ ks). As can be seen from Fig. 8.5 the non-flare rms spectrum is consistent with a constant ($\chi^2_{\nu} = 0.6$). On the other hand the flare data set shows clear spectral variability, with a gradual increase in the amplitude of the fluctuations with increasing energy. A constant fit is unacceptable ($\chi^2_{\nu} = 6.8$).

Of interest is the notable similarity in the appearance and behaviour of the rms spectra with that of another narrow-line quasar, I Zw 1 (Chapter 6). A flare was also observed in I Zw 1, of similar magnitude and duration to that seen in Fig. 8.4. In addition, it was discovered that the flare in I Zw 1 was concentrated in the hard energy band (i.e. 2–10 keV), and that it induced spectral variability as suggested by Fig. 8.5.

In Fig. 8.6 we present normalised light curves in the 0.2 – 0.5 keV and 2 – 10 keV bands. The light curves were normalised to the average count rate during the non-flare periods (i.e. excluding the data between $\sim 10 - 15$ ks). As in I Zw 1, the flare appears to be concentrated in the harder energy band (though much less significant than for

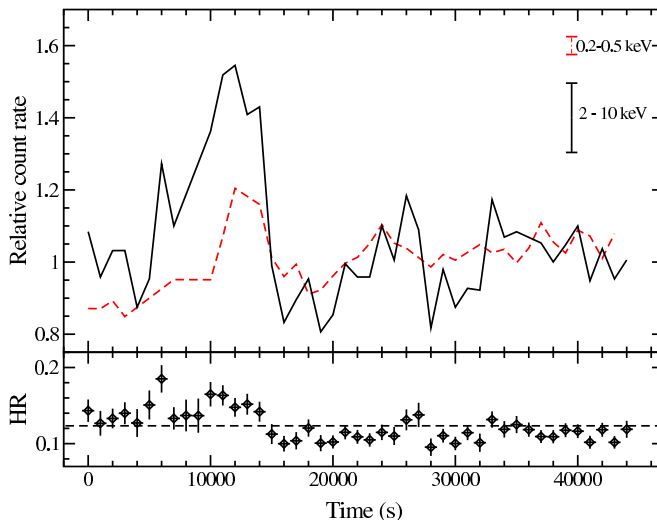


Figure 8.6: Top panel: Normalised light curves in the 0.2 – 0.5 keV (red, dashed curve) and 2 – 10 keV (black, solid curve) bands. The light curves were normalised to the average count rate during the non-flare periods (i.e. excluding the data between $\sim 10 - 15$ ks), to demonstrate the different flare amplitude in each band. The average size of the uncertainties for each curve are shown in the upper right of the panel. Bottom panel: The hardness ratio ($HR = \text{hard}/\text{soft}$) of the two light curves in the top panel as a function of time. Bin sizes are 1000 s. A constant fit is drawn in as a dashed line.

I Zw 1). The hardness ratio between the two light curves is also presented in Fig. 8.6, and shows a difference in the hardness ratio before and after the flare.

Examining a “flaring” spectrum in detail is difficult due to the small number of good events in the first half of the observation. The mean spectrum is essentially dominated by the data in the post-flare regime (after ~ 20 ks).

8.5 Discussion and Conclusions

8.5.1 General Findings

The main results of this analysis are the following:

- (1) The X-ray continuum of NAB 0205+024 was well fitted with a power-law plus blackbody with $\Gamma \approx 2.45$ and $kT \approx 120$ eV. Additional absorption above the Galactic column density was not required.
- (2) A strong, broad feature was detected in the pn spectrum between 5 – 6 keV. A considerable amount of the emission, including the peak of the emission, is redward of 6.4 keV (rest frame), and extends as far down as 5 keV in the rest frame. The feature could be fitted as a neutral iron line emitted from a narrow annulus of a disc around a Schwarzschild black hole.

-
- (3) A flare was detected in the light curve in which the broad-band count rate increased by about 50% in a few thousand seconds. The flare was determined to be concentrated at higher energies (2 – 10 keV) and appeared to induce spectral variability.
 - (4) No optical variability was detected from NAB 0205+024 even during the X-ray flare.

8.5.2 The nature of the high-energy emission line

Given the energy of the broad feature in NAB 0205+024 we considered the possibility that the broad line could be the composition of several narrower lines. Means to produce narrow emission lines in the 5–6 keV range have been suggested (e.g. Skibo 1997; Dovčiak et al. 2004); however the hypothetical narrow features in NAB 0205+024 do not satisfy these models physically (e.g. lines are too strong, or absence of accompanying features, or inconsistent relative abundances). Moreover, there was no statistical necessity to split the broad feature into multiple components.

The excess emission at ~ 5 keV can be fitted as neutral iron emitted from an accretion disc around a Schwarzschild or Kerr black hole. The fits cannot distinguish between the different line origins. In the case of a Schwarzschild black hole the line would originate from a thin annulus ($18 - 24 r_g$) close to the black hole. The feature could be fitted equally well with a simple Gaussian profile, but the best-fit energy and width do not correspond with the characteristics of any elements in the region.

8.5.3 A comparison to MCG–6-30-15 and I Zw 1

There are three significant differences in the *XMM-Newton* observation of NAB 0205+024 since it was last observed with *ASCA* (Fiore et al. 1998; Leighly 1999a,b; Vaughan et al. 1999; Reeves & Turner 2000). Firstly, the power-law slope is notably softer in this observation ($\Gamma \approx 2.45$) compared to the *ASCA* spectrum ($\Gamma \approx 2.09 - 2.22$). Secondly, there was no detection of a broad emission feature in the earlier observations, though at low significance there did appear to be spectral hardening with increasing energy (Fiore et al. 1998). Finally, a (hard) X-ray flare was detected with *XMM-Newton*.

There was also weak evidence for a temperature change in the blackbody component. The temperature measured by *ASCA* was between 160 – 220 eV, whereas the temperature was much lower in the *XMM-Newton* data ($kT \approx 120$ eV). The reliability of the measured change is questionable given that *ASCA* was not sensitive below ~ 0.6 keV, and due to the large range of temperatures measured in three different analyses of the same data. The average 0.6 – 10 keV *XMM-Newton* flux was about 15% lower compared to the *ASCA* flux; however variations on this order are typical on hourly time scales.

The three new features are reminiscent of the second *ASCA* observation of MCG–6-30-15 during which part of the time the broad line was found redshifted below 6 keV with no component detected at 6.4 keV, and the continuum appeared unusually soft (Iwasawa et al. 1999). Those authors interpreted the strange line emission as arising

from an extraordinarily large gravitational redshift resulting from a flare occurring within $5 r_g$ of the black hole.

There is ample evidence for spectral softening in AGN during periods of increased 2 – 10 keV intensity (e.g. Done, Madejski & Zycki 2000; Vaughan & Edelson 2001). Merloni & Fabian (2001) have described this in terms of a ‘thundercloud’ model where a heating event in a compact region of the corona, likely due to magnetic reconnection (e.g. Galeev, Rosner & Vaiana 1979), results in an avalanche of smaller events. As the hard X-ray emission is reprocessed in the disc softer spectra are produced and the luminosity of the iron line is enhanced. The scenario appears applicable here, though it is difficult to examine in detail given the limited amount of data. The softer average spectrum (dominated by the post-flare data), the hard X-ray flare, and the iron line possibly emitted from an annular region are all consistent with the thundercloud model.

In this sense the flare observed in I Zw 1 (Chapter 6) is different in that no variability in the power-law slope, or enhancement of the iron line emission were detected. This can still be understood in terms of the thundercloud model if the I Zw 1 flare originated closer to the disc, but farther from the black hole. Thus, the flare illuminated a smaller portion of the disc, and spectral changes were smeared out in the mean spectrum. Support in favour of this scenario was the non-detection of a lag between energy bands in the I Zw 1 flare.

8.6 Conclusions

In this most recent and sensitive X-ray observation of NAB 0205+024, this narrow-line quasar has exhibited many differences since last observed with *ASCA*. The thundercloud model (Merloni & Fabian 2001) can be invoked to explain the hard X-ray flare, soft 2 – 10 keV power-law, and broad iron emission. Whether we examine narrow-line quasars or NLS1, it is becoming quite clear that these objects are important to understand the relativistic effects close to the black hole.

Chapter 9

Open issues, prospects, and concluding remarks

The X-ray properties of five Narrow-line Seyfert 1 galaxies (NLS1) are analysed and presented in this dissertation. The data were collected with *XMM-Newton*, and to date, are of the highest quality ever obtained. Themes which have evolved and appear fundamental in understanding NLS1 are: near- or super-Eddington accretion by a “small” supermassive black hole, partial covering, and reflection. Most of the objects presented in this dissertation can adopt these principles.

9.1 General findings

- Two observations of 1H 0707–495 and one observation of IRAS 13224–3809 show sharp, spectral drops above ~ 7 keV (Chapters 2 and 4). The sharpness of the features, and absence of iron fluorescent emission and $K\beta$ UTA absorption, challenge the possibility that the drops originate from photonionisation. If partial covering from a neutral absorber is adopted then outflows on the order of $0.05 - 0.15 c$ are required. On the other hand, if the sharp drops are associated with the blue wings of relativistically broadened Fe $K\alpha$ lines (Chapters 2 and 5) then the interpretation requires light bending close to the black hole to explain the large equivalent widths and variability properties. Both interpretations require an iron overabundance ($\sim 3 - 10$ times solar), suggesting that supersolar metallicities may simply be characteristic of NLS1, probably due to strong starburst activity close to the nucleus.
- The general variability properties of NLS1 remain elusive, but advances have been made. All of the Seyferts and quasars discussed here showed rapid and extreme variability at some point during the observations. IRAS 13224–3809 exhibited some of the most remarkable variability (Chapter 3). Lags between the hard and soft energy bands were detected, suggesting that fluctuations at low energies instigated variability at higher energies. However, closer inspection revealed that the lags alternate: sometimes the hard band follows, while at

other times it leads. Spectral variability was determined to be correlated with flux variation, but more interestingly was the finding that the spectral variability also lagged flux variations, resulting in flux-induced spectral variability.

- For over ~ 120 ks (spread over two observations), 1H 0707–495 persistently displayed flux variations by at least a factor of four. During the first observation, when 1H 0707–495 was in its lowest flux state ever recorded, there was no significant spectral variability. The second observation, when the source was in a higher flux state, revealed strong spectral variability. Flux and spectral fluctuation were never found to be significantly correlated (Chapter 4).
- The quasar, PHL 1092, exhibited some of the most striking variability considering its high luminosity (Chapter 7). Indeed, an estimate of its radiative efficiency was in excess of that expected from a Schwarzschild black hole. Interestingly, the variability appeared to be entirely concentrated in the soft-excess, with the power-law component appearing quiescent.
- The closest example of *class behaviour* seen in the variability of the group was displayed by the two quasars I Zw 1 and NAB 0205+024 (Chapters 6 and 8, respectively). Both objects exhibited a hard X-ray flare which was concentrated at energies higher than ~ 2 keV and accompanied by spectral variability. A scenario in which the hard X-ray flare originates in the accretion disc corona, and then irradiates the disc itself seem most applicable here.
- I Zw 1 has been defined as the prototype NLS1 based on its optical properties. In the X-rays it appears anything but prototypical. Significant low-energy intrinsic absorption, a weak soft-excess, and evidence for multiple iron emission lines suggest that other processes are at work (Chapter 6).
- PHL 1092 exhibited deviations from a power-law fit in the 2 – 10 keV band (Chapter 7). The difference could be interpreted as an emission line enhanced by light bending close to a Kerr black hole. The complex variability could also be understood in terms of light bending; however, partial covering could not be definitively dismissed due to the modest-quality data.
- NAB 0205+024 portrayed a broad emission feature at ~ 5.8 keV which was inconsistent with expected emission from elements in that spectral region. The feature could be described as neutral iron emitted from a narrow annulus on the disc (Chapter 8). The presence of the hard X-ray flare, steep power-law slope, and redshifted iron line provide circumstantial support for the “thundercloud model” proposed by Merloni & Fabian (2001).

9.2 Partial covering and reflection: open issues

A number of NLS1 have been discovered which can be described by either partial covering or a reflection dominated spectrum. 1H 0707–495 and IRAS 13224–3809 are

perhaps the best-studied cases. The key properties are: (1) sharp, spectral drops above ~ 7 keV, (2) no significant detection of a narrow Fe $K\alpha$ line, Fe $K\beta$ UTA feature, or Fe L-edge, (3) insignificant low-energy intrinsic absorption. For a particular object, one theory may be *favoured* over another; however, neither one is ever conclusively superior.

A number of outstanding issues require attention.

The nature of the soft X-ray emission

Perhaps, the most significant difference in the two models is how the nature of the soft-excess is interpreted. In the partial covering scenario, the soft-excess arises from thermal disc emission (e.g. Chapters 2 and 4); whereas in the reflection model the excess is due to relativistically blurred emission lines and continuum from the disc (Chapter 5).

Two factors challenge the thermal disc emission interpretation. The first is that the temperatures associated with the discs are many times the values expected from a standard accretion disc. As discussed throughout this dissertation, the high temperatures can be recovered by considering some sort of radiative-inefficient flow, such as a slim-disc (Abramowicz et al. 1988). The second, arguably more fundamental concern, is the rather uniform shape of the soft-excess. When considering a large number of type-1 Seyferts and fitting their soft-excess emission with a blackbody, a characteristic temperature of about 120 eV emerges (see Section 9.3). The spread in the temperatures is small; however the luminosities in the sample span three orders of magnitude. It is not simple to understand in terms of any existing accretion disc theories, exactly how this can arise. Perhaps invoking some kind of “saturation” temperature can remedy the situation, though there does not appear to be any physical justification for this.

Ross & Fabian (in preparation) suggest that the soft-excess can be explained as blurred emission lines and bremsstrahlung from the hot disc surface arising from reflection off an ionised disc. They further claim that when their model is folded through the *XMM-Newton* response matrix, the simulated data can be well fitted ($< 10\%$ residuals) with a blackbody temperature of 150 eV. An added benefit of the reflection model is that the bumps in the spectrum of 1H 0707–495 at ~ 1 keV, which were modelled in Chapter 4 with Gaussian profiles, can be naturally attributed to the reflection component as a complex of iron-L lines.

Although appealing, there are drawbacks with this simplified picture. It would stand to reason that when the reflection component dominates the spectrum (as it supposedly did during the first observations of 1H 0707–495; Fabian et al. 2002) the ~ 1 keV bumps would be most prominent, and then diminish as the power-law component emerges (i.e. as luminosity increases). However, the ~ 1 keV features were not at all visible during the first observation of 1H 0707–495. According to Fabian et al. (2002) the spectrum during that observation was a contrived mixture of three separate reflectors, which would result in “blending out” any distinct features. Moreover, in this reflection scenario, the high-flux state *Chandra* observation of 1H 0707–495 (Leighly et

al. 2002) is realised by the emergence of the power-law component and minimisation of the reflection component. However, even during this observation the soft-excess was still dominated over the power-law, and the ~ 1 keV bumps were still present. Both features should have been significantly suppressed (and statistically insignificant given the smaller collecting area of *Chandra*).

Energy of the feature

The first detection of a sharp spectral drop was in 1H 0707–495 (Boller et al. 2002; Chapter 4) at an energy of 7.0 ± 0.1 keV. The energy was, perhaps coincidentally, entirely consistent with the neutral iron absorption edge (7.11 keV). However, it was the last time that an edge was detected at this energy, and even in 1H 0707–495 a second observation found the edge at 7.5 keV (Chapter 4). It is unlikely that the edges are ionised since there are no traces in the spectra of increased photonisation (e.g. broadened edge, iron $K\beta$ UTA). As such, in terms of partial covering the edge energies are attributed to outflows. In some cases this requires either a prodigious mass and energy loss rate in the outflow, or a very clumpy absorber. It is also uncertain, exactly how a high-velocity outflow will alter the appearance of the edge. Is it realistic that, as in the case of 1H 0707–495 the material is accelerated from 0% to 5% the speed of light yet the spectral feature remains sharp?

The edge energy is also difficult to explain in terms of reflection. In the case of IRAS 13224–3809 the edge was found at $E > 8$ keV. Even in the most extreme light bending scenarios, it is difficult to achieve such a sharp feature at such a high energy.

Sharpness of the feature

The sharpness of the edge may be the most fundamental discriminator between the two models. The edge will be intrinsically sharp in the case of neutral absorption, whereas depending on the degree of ionisation, it will be broader in the line interpretation.

The first observation of 1H 0707–495 and IRAS 13224–3809 revealed an upper-limit on the edge sharpness of $\lesssim 300$ eV. The improved statistics during the second observation of 1H 0707–495 resulted in a measurement of $\lesssim 150$ eV, which is the resolution limit of the EPIC pn detector. This measurement can rule out high photoionisation, but it is not sufficient to exclude either partial covering or reflection, though it becomes a concern for reflection.

Spectral variability

No significant spectral variability was discovered in the first observation of 1H 0707–495. This explanation is rather straightforward for both the partial covering and reflection models. In both cases, the source is intrinsically constant. In partial covering the flux and (lack of) spectral variability can be recovered if an absorber, which moves in and out of the line-of-sight, *equally* covers the soft and hard continuum components (Tanaka et al. 2004; Chapter 4). On the other hand, a reflection dominated spectrum

(only one spectral component) can also explain the lack of spectral variability (Fabian et al. 2004; Chapter 5).

The situation appears more complicated in the second observation of 1H 0707–495 and IRAS 13224–3809. Both showed significant spectral variability, with the variability being much more significant in the intermediate ($\sim 1–5$ keV) energy band (see Fig. 4.4 and 3.7). Fabian et al. (2004) showed that the spectral variability could be explained by a variable power-law, which dominates the spectrum between $\sim 1–5$ keV, and a less variable reflection component which dominates that spectrum at $E \lesssim 1$ keV and $E \gtrsim 5$ keV (compare Fig. 4.4 and Fig. 5.2). The situation appeared more detrimental for partial covering, but it was demonstrated in Chapter 4 (see Fig. 4.4) that under conditions of *double* partial covering (see Equation 1.9) the situation could be resolved. So, at least to first order, both partial covering and reflection do explain the spectral variability.

Another point of concern may be the amplitude of the variations. As the light bending model assumes that the power-law component is more variable than the reflection component, then during the reflection dominated phase the variability should be suppressed. However, this is not the case. In 1H 0707–495 the amplitude of the variations are actually greater during the reflection dominated phase (notice the vertical axes in Fig. 4.4).

The detection of lags, and especially alternating lags, between various energy bands in IRAS 13224–3809 (Chapter 3) is a serious challenge for both models.

Established NLS1 behaviour

It appears that either partial covering or reflection may be ubiquitous to NLS1. Therefore, it is necessary that the derived model conforms with other characteristics of NLS1, such as radio quietness and primary eigenvector 1. For example, the steeper $0.1–2.4$ keV continuum slopes seen in NLS1 (e.g Boller et al. 1996), may be more difficult to understand if the soft-excess is a reflection component rather than a thermal one. In addition, both reflection and partial covering flatten the spectrum above 2 keV, but NLS1 tend to show steeper hard X-ray slopes (e.g Brandt et al. 1997).

9.3 Current investigations

Large number studies

Currently, work is being done to understand the X-ray spectral and timing properties of type-1 AGN. Emphasis will be on determining: (1) which properties (e.g. Γ , kT , F_{var}) are correlated, and how; (2) how NLS1 like IRAS 13224–3809 and 1H 0707–495 are unique from other objects. Currently, the *XMM-Newton* observations of sixty objects (~ 20 NLS1 and 40 BLS1) have been obtained from the archive, and all the data have been processed in a uniform manner with the most recent version of the *XMM-Newton* Science Analysis System (SAS v6.0.0). Preliminary results include: (1) confirmation of steeper $2–10$ keV photon indices in NLS1 (Brandt et al. 1997),

and (2) indications that the soft-excesses in NLS1 show a rather tight distribution in temperatures when fitted with a blackbody ($kT \approx 100 - 150$ eV), even though luminosities span three orders of magnitude.

Radio-loud NLS1

As discussed in Chapter 1, a handful of NLS1 have been found to be radio-loud. This is in contrast to the principle component analysis of Boroson & Green (1992) which found that strong Fe II emitters (e.g. NLS1) were weak radio sources. As an attempt to investigate the nature of a radio-loud NLS1, we organised a large scale, multiwavelength, observing campaign of the radio-loudest ($R \approx 1700 - 6300$) NLS1, PKS 2004–447 (PI: Gallo). PKS 2004–447 is the only radio loud NLS1, which is also identified as a Compact Steep-Spectrum source (CSS; Fanti et al. 1995). Similar to NLS1, CSS are believed to be young AGN in the process of formation. Therefore, an examination of this source may actually reveal an evolutionary link between NLS1 and CSS.

We have obtained simultaneous observations of PKS 2004–447 at X-rays and near-UV (*XMM-Newton*), optical photometry (Mt Canopus 1-m telescope), near-infrared spectroscopy (Siding Springs 2.4-m telescope), radio (Australian Telescope Compact Array and Ceduna Observatory 30-m antenna). The radio data includes significant spectral coverage between 1.4–17.8 GHz and long-term (several weeks) monitoring at 6.7 GHz. The objective is to determine the broad-band spectral energy distribution of this unique source, as well as to study multiwavelength variability. Work is in the very early stages. A quick look at the X-ray data shows low-amplitude variability and a power-law continuum across the *XMM-Newton* band. The optical and radio data indicate variability on all time scales from hours to weeks.

Extended X-ray emission

The supposition that NLS1 are young AGN implies that their host galaxies are also young (or rejuvenated), and perhaps under current episodes of star formation. Indeed, the X-ray observations of I Zw 1 (Chapter 6) suggest that starburst activity could be responsible for some of the observed properties (e.g. low-energy absorption; multiple, narrow iron lines). As part of the *Chandra* Guaranteed Time allocated to MPE, we have proposed to observe the nearby ($z = 0.029$), X-ray bright NLS1, Mrk 705 (PI: Boller). The high-resolution of *Chandra* will enable us to search for extended low-energy emission within 1 kpc of the central AGN in Mrk 705, which, if present, would indicate a nuclear starburst component. The observation has been completed, but no analysis of the data has been done.

9.4 Prospective

The key to distinguishing between the processes of reflection and partial covering is the sharpness of the high-energy drops. Currently, we are working at the resolution

limits of *XMM-Newton* which is still not sufficient.

In February 2005, the Japanese X-ray satellite *Astro-E2* will be launched. The prime instrument aboard is the new generation of X-Ray Spectrometers, XRS. The detectors used in XRS have a spectral resolution of about 10 eV at ~ 7 keV, compared to ~ 150 eV resolution for *XMM-Newton*. In principle, this would be the perfect instrument if not for the relatively small collecting area ($\sim \frac{1}{5}$ that of *XMM-Newton*). Simulations show that we require at least a 200 ks observation, just to obtain compatibility with the *XMM-Newton* data quality.

The X-Ray Evolving Universe Spectrometer (*XEUS*) is the European Space Agency's proposed follow-up mission to *XMM-Newton*. It will be about 200 times more sensitive than *XMM-Newton*, with spectral resolution between 1 – 10 eV. The planned launch date is ~ 2015 . In Fig. 9.1, simulated *XEUS* observations of 1H 0707–495 are presented. A modest exposure can discriminate between the partial covering and reflection models with very high significance.

Of course there are alternatives to waiting for 10 years.

- The partial covering and reflection models will lead to very different spectra when the source is bright. High-quality *XMM-Newton* observations of the sources in various flux states should distinguish between the models (Fig. 9.2).
- Numerous studies (e.g. Yuan, Siebert & Brinkmann 1998; Brandt et al. 2000; Vignali et al. 2003) have established well-defined average values for the optical to X-ray spectral index, α_{ox} (Equation 3.1). For optically bright sources, it is now possible (since the release of **SAS v6.0.0**), to obtain simultaneous UV and X-ray spectra with *XMM-Newton* and measure α_{ox} . The intrinsic X-ray spectrum is highly absorbed in the partial covering case; therefore, extreme measurements of α_{ox} could be an indicator of partial covering.
- A consequence of both models is that sources like IRAS 13224–3809 and 1H 0707–495 are not unique, but extreme. As such, there should be many more similar objects. Application of the models to a large sample of objects could reveal unknown characteristics of one model or the other. This would help to predict behaviour for future observations.
- A rigorous theoretical investigation of partial covering must be pursued. While some pieces of the puzzle are in place, it is still not possible to predict the outcome of observations based on a self-consistent model of partial covering.

The *XMM-Newton* observations of NLS1 have revealed some of the most extreme behaviour ever observed in AGN. As such, NLS1 may be the best sources to probe the inner-most AGN environment. The work presented in this dissertation should further stimulate a combined theoretical and observational effort to improve our understanding of the physics responsible in these enigmatic objects.

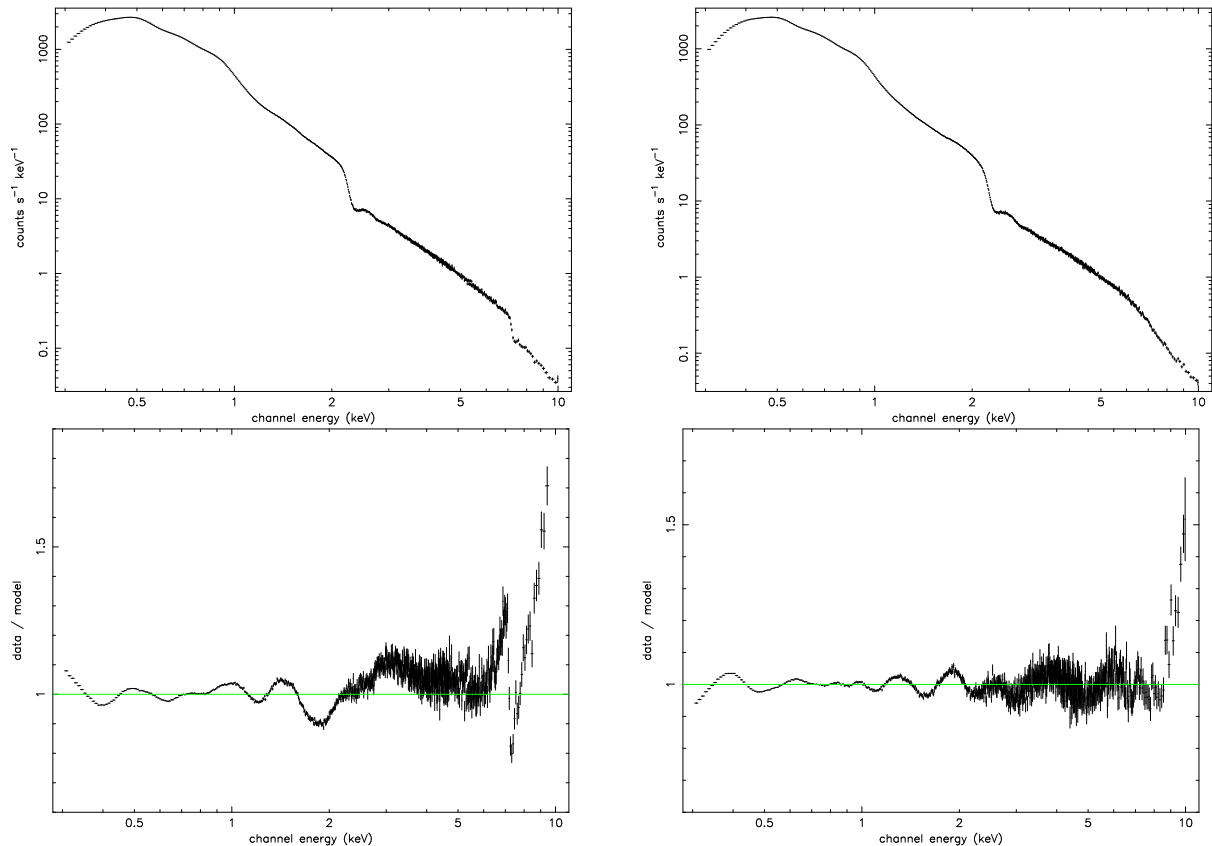


Figure 9.1: Simulated *XEUS* observations of 1H 0707–495 in the 0.3 – 10 keV range. The exposure time is 75 ks which is similar to the AO2 observation. Upper left panel: A simulation of the best-fit partial covering model of the AO2 data (see Fig. 4.2). Upper right panel: A simulation of the best-fit reflection model of the AO2 data (see Fig. 5.3). Notice that the edge feature is not truly sharp compared to the simulated partial covering data (upper left panel). Lower left panel: The residuals remaining from fitting a reflection model to the partial covering data. Lower right panel: The residuals remaining from fitting a partial covering model to the reflection data. When conducting the simulated fits, no a priori knowledge of the true model is assumed. All model parameters are left free to vary. With the much greater sensitivity and resolution of *XEUS*, the partial covering and reflection models can easily be discriminated.

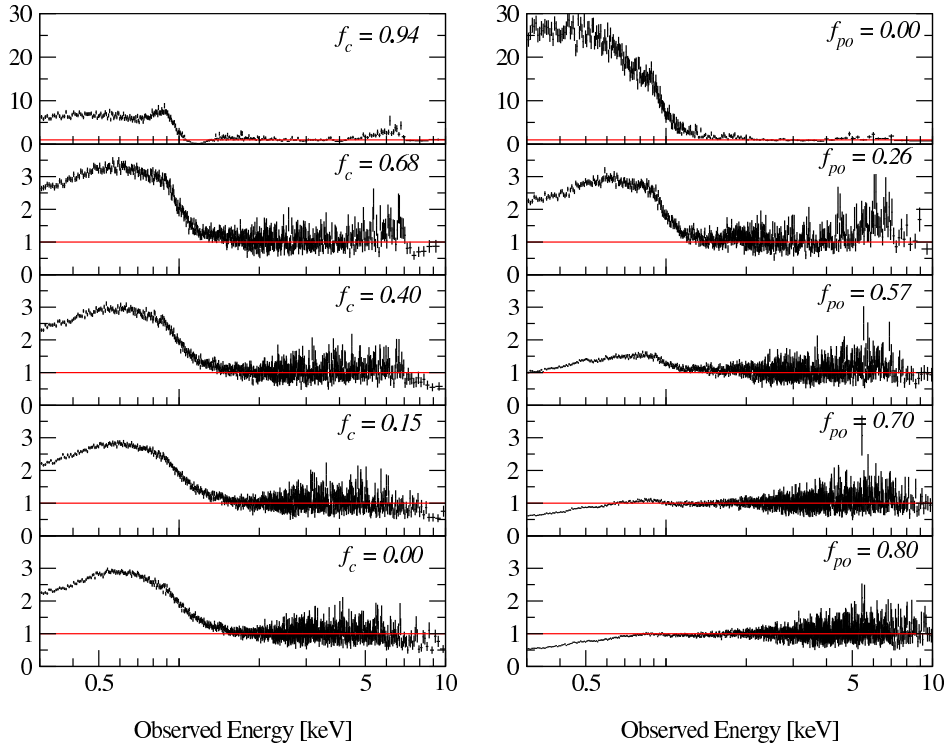


Figure 9.2: Forty kilosecond (40 ks) XMM-Newton simulations of the 0.3 – 10 keV spectrum of 1H 0707–495 in various flux states are constructed. The ratio (data/model) resulting from fitting a power-law (modified by Galactic absorption) to the 2 – 5 keV range are shown. The fluxes increase from top-down ($\sim 0.2, 1.1, 2.1, 3.1, 3.5 \times 10^{-11} \text{ erg cm}^{-2} \text{ s}^{-1}$). The flux in each adjacent panel is identical. Left panel: The partial-covering model derived in Chapter 4 (Fig. 4.2) is adopted. The intrinsic model and luminosity is identical, only the covering fraction (f_c) is variable (as marked in the top right of each panel), resulting in the flux-dependent spectral variability. Right panel: The reflection model used in Chapter 5 (Fig. 5.3) is simulated. As with the partial-covering simulations, the intrinsic spectrum remains unchanged. The flux and spectral variations result from changing the relative normalisation of the power-law component. In the top right of each panel the fraction of the total flux attributed to the power-law component (f_{po}) is given.

Bibliography

- [1] Abramowicz M. A., Czerny B., Lasota J. P., Szuszkiewicz E., 1988, *ApJ*, 332, 646
- [2] Abrassart A., Czerny B., 2000, *A&A*, 356, 475
- [3] Anders E., Grevesse N., 1989, *GeCoA*, 53, 197
- [4] Antonucci R., 1993, *ARA&A*, 31, 473
- [5] Antonucci R., Miller J. S., 1985, *ApJ*, 297, 621
- [6] Arnaud K. A., 1996, in Jacoby G., Barnes J., eds, *Astronomical Data Analysis Software and Systems V*, ASP Conf. Series, 101, 17
- [7] Arnaud K. A. et al., 1985, *MNRAS*, 217, 105
- [8] Arnaud K. A., Dorman B., 2002, *XSPEC User's Guide for v.11.2.x*
- [9] Awaki H., Koyama K., 1993, *AdSpR*, 13, 221
- [10] Bahcall N. A., Bahcall J. N., Schmidt M., 1973, *ApJ*, 183, 777
- [11] Baldwin J. A., Phillips M. M., Terlevich R., 1981, *ApJ*, 183, 777
- [12] Ballantyne D. R., Iwasawa K., Fabian A. C., 2001, *MNRAS*, 323, 506
- [13] Ballantyne D. R., Ross R. R., Fabian A. C., 2001, *MNRAS*, 327, 10
- [14] Balucinska-Church M., McCammon D., 1992, *ApJ*, 400, 699
- [15] Bambynek W, Crasemann B., Fink R., Freund H., Mark H., Swift C., Price R., Rao V., 1972, *Rev. Mod. Phys.*, 44, 716
- [16] Bardeen J. M., 1973, in DeWitt C., DeWitt B., eds, *Black holes*, Gordon & Breach, 215
- [17] Bardeen J. M., Press W. H., Teukolsky S. A., 1972, *ApJ*, 178, 347
- [18] Behar E., Rasmussen A. P., Blustin A. J., Sako M., Kahn S. M., Kaastra J. S., Branduardi-Raymont G., Steenbrugge K. C., 2003, *ApJ*, 598, 232
- [19] Behar E., Sako M., Kahn S. M., 2001, *ApJ*, 563, 497

-
- [20] Beloborodov A. M., 1999, *ApJ*, 510, 123
- [21] Bennert N., Falcke H., Schulz H., Wilson A. S., Wills B. J., 2002, *ApJ*, 574, 105
- [22] Bergeron J., Kunth, D., 1980, *A&A*, 85, L11
- [23] Bergeron J., Kunth D., 1984, *MNRAS*, 207, 263
- [24] Blustin A. J., Branduardi-Raymont G., Behar E., Kaastra J. S., Kahn S. M., Page M. J., Sako M., Steenbrugge K. C., 2002, *A&A*, 392, 453
- [25] Boller Th., 2003, in Collin S., Combes F., Shlosman I., eds, *Active Galactic Nuclei: From Central Engine to Host Galaxy*, ASP Conf. Series, 290, 69
- [26] Boller Th., Brandt W. N., Fabian A. C., Fink H., 1997, *MNRAS*, 289, 393
- [27] Boller Th., Brandt W. N., Fink H., 1996, *A&A*, 305, 53
- [28] Boller Th., Brandt W. N., Leighly K. M., Ward M. J., 2000, eds, *Observational and Theoretical Progress in the Study of Narrow-Line Seyfert 1 Galaxies*, *New Astronomy Reviews*, v. 44, iss. 7-9
- [29] Boller Th., Fabian A. C., Sunyaev R., Trümper J., Vaughan S., Ballantyne D. R., Brandt W. N., Keil R., Iwasawa, K., 2002, *MNRAS*, 329, 1 (B02)
- [30] Boller Th., Tanaka Y., Fabian A., Brandt W. N., Gallo L., Anabuki N., Haba Y., Vaughan S., 2003, *MNRAS*, 343, 89
- [31] Boller Th., Trümper J., Molendi S., Fink H., Schaeidt S., Caulet A., Dennefeld M., 1993, *A&A*, 279, 53
- [32] Boroson T. A., 2002, *ApJ*, 565, 78
- [33] Boroson T. A., Green R. F., 1992, *ApJS*, 80, 109
- [34] Brandt W. N., 1996, PhD thesis, Univ. Cambridge
- [35] Brandt W.N., Boller Th., 1998, *AN*, 319, 163
- [36] Brandt W. N., Boller Th., Fabian A. C., Ruszkowski M., 1999, *MNRAS*, 303, L58 (BBFR)
- [37] Brandt W. N., Fabian A. C., Dotani T., Nagase F., Inoue H., Kotani T., Segawa Y., 1996, *MNRAS*, 283, 1071
- [38] Brandt W.N., Gallagher S.C., 2000, *New Astronomy Reviews* 44, 461
- [39] Brandt W. N., Laor A., Wills B., 2000, *ApJ*, 528, 637
- [40] Brandt W. N., Mathur S., Elvis M., 1997, *MNRAS*, 285, 25

-
- [41] Canalizo G., Stockton A., 2001, *ApJ*, 555, 719
- [42] Celotti A., Fabian A. C., Rees M. J., 1992, *MNRAS* 255, 419
- [43] Chartas G., Brandt W. N., Gallagher S. C., Garmire G. P., 2002, *ApJ* 579, 169
- [44] Chiang J., Reynolds C. S., Blaes O. M., Nowak M. A., Murray N., Madejski G., Marshall H. L., Magdziarz P., 2000, *ApJ*, 528, 292
- [45] Collin S., Joly M., 2000, *NewAR*, 44, 531
- [46] Condon J. J. et al., 1998, *AJ*, 115, 1693
- [47] Constantin A., Shields J. C., 2003, *PASP*, 115, 592
- [48] Crenshaw D. M., Kraemer S. B., Boggess A., Maran S. P., Mushotzky R. F., Wu C., 1999, *AJ*, 516, 750
- [49] Crenshaw D. M., Kraemer S. B., Gabel J. R., 2003, *AJ*, 126, 1690
- [50] Dabrowski Y., Lasenby A. N., 2001, *MNRAS*, 321, 605
- [51] Davidson K., Kinman T. D., 1978, *ApJ*, 225, 776
- [52] den Herder J. W. et al., 2001, *A&A*, 365, 7
- [53] Dickey J. M., Lockman F. J., 1990, *ARA&A*, 28, 215
- [54] Di Matteo T., Celotti A., Fabian A. C., 1997, *MNRAS*, 291, 805
- [55] Done C., Madejski G. M., Życki P. T., 2000, *ApJ*, 536, 213
- [56] Dopita M. A., Groves B. A., Sutherland R. S., Binette L., Cecil G., 2002, *ApJ*, 572, 753
- [57] Dower R. G., Bradt H. V., Morgan E. H., 1982, *ApJ*, 261, 228
- [58] Dovčiak M., Bianchi S., Guainazzi M., Karas V., Matt G., 2004, *MNRAS*, 350, 745
- [59] Ebisawa K., 1991, Ph.D. thesis, Univ. Tokyo
- [60] Eckart A., Schinnerer E., Tacconi L., 2000, *NewAR*, 44, 523
- [61] Edelson R., Turner T. J., Pounds K., Vaughan S., Markowitz A., Marshall H., Dobbie P., Warwick R., 2002, *ApJ*, 568, 610
- [62] Ehle M. et al., 2004, *XMM-Newton Users' Handbook*, v2.2
- [63] Elvis M., Lockman F. J., Wilkes B. J., 1989, *AJ*, 97, 777
- [64] Fabian A. C., 1979, *Proc. R. Soc. London, Ser. A*, 366, 449

-
- [65] Fabian A. C. et al., 2002, MNRAS, 335, 1
- [66] Fabian A. C., Ballantyne D. R., Merloni A., Vaughan S., Iwasawa K., Boller Th., 2002b, MNRAS, 331, 35
- [67] Fabian A. C., Iwasawa K., Reynolds C. S.; Young A. J., 2000, PASP, 112, 1145
- [68] Fabian A. C., Miniutti G., Gallo L., Boller Th., Tanaka Y., Vaughan S., Ross R. R., 2004, MNRAS, 353, 1071
- [69] Fabian A. C., Rees M. J., Stella L., White N. E., 1989, MNRAS, 238, 729
- [70] Fabian A. C., Vaughan S., 2003, MNRAS, 340, 28
- [71] Ferland G. J., Peterson B. M., Horne K., Welsh W. F., Nahar S. N., 1992, ApJ, 387, 95
- [72] Ferrarese L., Ford H. C., Jaffe W., 1996, ApJ, 470, 444
- [73] Ferrarese L., Merritt D., 2000, ApJ, 539, 9
- [74] Ferrarese L., Pogge R., Peterson B., Merritt D., Wandel A., Joseph C., 2001, ApJ, 555, 79
- [75] Fiore F. et al., 1998, MNRAS, 298, 103
- [76] Fiore F., Elvis M., McDowell J. C., Siemiginowska A., Wilkes B. J., 1994, ApJ, 431, 515
- [77] Forster K., Halpern J. P., 1996, ApJ., 468, 565
- [78] Frank J., King A., Raine D., 1992, *Accretion Power in Astrophysics*, 2nd Edition, Cambridge Univ. Press
- [79] Freyberg M. J. et al., 2004, in Flanagan K., Siegmund O., eds, *X-Ray and Gamma-Ray Instrumentation for Astronomy XIII*, Proceedings of the SPIE, 5165, 112
- [80] Friedli D., Benz W., 1993, A&A, 268, 65
- [81] Galeev A. A., Rosner R., Vaiana G. S., 1979, ApJ, 229, 318
- [82] Gallo L. C. et al., 2004, in Richards G. T., Hall P. B., eds, *AGN Physics with the Sloan Digital Sky Survey*, ASP Conf. Series, 311, 273
- [83] Gallo L. C., Boller Th., Brandt W. N., Fabian A. C., Grupe D., 2004, MNRAS, 352, 744 (Chapter 7)
- [84] Gallo L. C., Boller Th., Brandt W. N., Fabian A. C., Vaughan S., 2004, A&A, 417, 29 (Chapter 6)

- [85] Gallo L. C., Boller Th., Brandt W. N., Fabian A. C., Vaughan S., 2004, MNRAS, 355, 330 (Chapter 8)
- [86] Gallo L. C., Boller Th., Tanaka Y., Fabian A., Brandt W. N., Welsh W. F., Anabuki N., Haba Y., 2004, MNRAS, 347, 269 (Chapter 3)
- [87] Gallo L. C., Tanaka Y., Boller T., Fabian A. C., Vaughan S., Brandt W. N., 2004, MNRAS, 353, 1064 (Chapter 4)
- [88] Gebhardt K. et al., 2000, ApJ, 543, 5
- [89] Gebhardt K. et al., 2000a, ApJ, 539, 13
- [90] Genzel R., Eckart A., Ott T., Eisenhauer F., 1997, MNRAS, 291, 219
- [91] George I. M., Fabian A. C., 1991, MNRAS, 249, 352
- [92] Ghez A. M., Klein B. L., Morris M., Becklin E. E., 1998, ApJ, 509, 678
- [93] Ghisellini G., Haardt F., Matt G., 2004, A&A, 413, 535
- [94] Giannuzzo E. M., Stirpe G. M., 1996, A&A, 314, 419
- [95] Gierlinski M., Done C., 2004, MNRAS, 349, 7
- [96] Gliozzi M., Brinkmann W., O'Brien P. T., Reeves J. N., Pounds K. A., Trifoglio M., Gianotti F., 2001, A&A, 365, 128
- [97] Goodrich R. W., 1989, ApJ 342, 234
- [98] Groves B. A., Dopita M. A., Sutherland R. S., 2004, ApJS, 153, 75
- [99] Grupe D., 1996, PhD thesis, Univ. Göttingen
- [100] Grupe D., 2004, AJ, 127, 1799
- [101] Grupe D., Beuermann K., Mannheim K., Thomas H.-C., 1999, A&A, 350, 31
- [102] Grupe D., Beuermann K., Thomas H.-C., Mannheim K., Fink H. H., 1998, A&A, 330, 25
- [103] Grupe D., Leighly K. M., Thomas H.-C., Laurent-Muehleisen S., 2000, A&A, 356, 11
- [104] Grupe D., Mathur S., 2004, ApJ, 606, 41
- [105] Grupe D., Mathur S., Komossa S., 2004, AJ, 127, 3161
- [106] Guainazzi M., 2003, A&A, 401, 903
- [107] Halpern J. P., 1984, ApJ, 281, 90

-
- [108] Harms R. J. et al., 1994, *ApJ*, 435, 35
- [109] Holt S. S., Mushotzky R. F., Boldt E. A., Serlemitsos P. J., Becker R. H., Szymkowiak A. E., White, N. E., 1980, *ApJ*, 241, 13
- [110] Ikegami T., 1986, PhD thesis, Univ. Tokyo
- [111] Inoue H., 1990, in Hunt J., Battrick B., eds, 23rd ESLAB Symposium on Two Topics in X-Ray Astronomy, 248, 783
- [112] Iwasawa K. et al., 1996, *MNRAS*, 282, 1038
- [113] Iwasawa K., Fabian A. C., Young A. J., Inoue H., Matsumoto C., 1999, *MNRAS*, 306, L19
- [114] Jansen F. et al., 2001, *A&A*, 365, 1
- [115] Joly M., 1987, *A&A*, 184, 33
- [116] Kaspi S. et al., 2002, *ApJ*, 574, 643
- [117] Kaspi S., Smith P. S., Netzer H., Maoz, D., Jannuzi B. T., Giveon U., 2000, *ApJ*, 533, 631
- [118] Kato S., Fukue J., Mineshige S., 1998, *Black Hole Accretion Disks*, Kyoto Univ. Press
- [119] Katz J. I., 1976, *ApJ*, 206, 910
- [120] Kawaguchi T., Mineshige S., Umemura M., Turner E. L., 1998, *ApJ*. 504, 671
- [121] Kellermann K. I., Sramek R., Schmidt M., Shaffer D. B., Green R., 1989, *AJ*, 98, 1195
- [122] Khachikian E. Y., Weedman D. W., 1974, *ApJ*, 192, 581
- [123] King A. R., Pounds K. A., 2003, *MNRAS*, 345, 657
- [124] Kirsch M., 2003, *XMM-Newton Calibration Presentations (CAL-TN-0018-2-1)*
- [125] Klimek E. S., Gaskell C. M., Hedrick C. H., 2004, *ApJ*, 609, 69
- [126] Kollatschny W., 2003, *A&A*, 407, 461
- [127] Kormendy J., Richstone D. O., 1995, *ARA&A*, 33, 581
- [128] Koski A. T., 1978, *ApJ*, 223, 56
- [129] Krolik J. H., 1999, *Active Galactic Nuclei: From the Central Black Hole to the Galactic Environment*, Princeton Univ. Press

- [130] Krolik J. H., Kallman T. R., 1987, ApJ, 320, 5
- [131] Krolik J. H., Kallman T. R., Fabian A. C., Rees M. J., 1985, ApJ 295, 104
- [132] Krolik J. H., Kriss G. A., 1995, ApJ, 447, 512
- [133] Laor A., 1991, ApJ 376, 90
- [134] Laor A., Fiore F., Elvis M., Wilkes B., McDowell J., 1997, ApJ, 477, 93
- [135] Laor A., Jannuzi B. T., Green R. F., Boroson T. A., 1997, ApJ, 489, 656
- [136] Lawrence A., Elvis M., Wilkes B. J., McHardy I., Brandt N., MNRAS, 1997, 285, 879
- [137] Lee J. C. et al., 2001, ApJ, 554, 13
- [138] Lee J. C., Fabian A. C., Reynolds C. S., Brandt W. N., 2000, MNRAS, 318, 857
- [139] Leighly K., 1999a, ApJS, 125, 317
- [140] Leighly K., 1999b, ApJS, 125, 297
- [141] Leighly K. M., 2004a, ApJ, 611, 125
- [142] Leighly K. M., 2004b, PThPS, 155, 223
- [143] Leighly K. M., Moore J. R., 2004, ApJ, 611, 107
- [144] Leighly K. M., Mushotzky R. F., Nandra K., Forster K., 1997, ApJ, 489, L25
- [145] Leighly K., Zdziarski A., Kawaguchi T., Matsumoto, C., 2002, in Boller Th., Komossa S., Kahn S., Kunieda H., Gallo L., eds, X-ray Spectroscopy of AGN with *Chandra* and *XMM-Newton*, MPE Report 279, p. 259 (L02)
- [146] Lightman A. P., White T. R., 1988, ApJ, 335, 57
- [147] Macchetto F., Capetti A., Sparks W. B., Axon D. J., Boksenberg A., 1994, ApJ, 435, 15
- [148] Macchetto F., Marconi A., Axon D. J., Capetti A., Sparks W. B., Crane P., 1997, ApJ, 489, 579
- [149] Magorrian J. et al., 1998, AJ, 115, 2285
- [150] Makishima K. et al., 1986, ApJ, 308, 635
- [151] Malzac J., Jourdain E., Petrucci P. O., Henri G., 1998, A&A, 336, 807
- [152] Markoff S., Falcke H., Fender R., 2001, A&A, 372, 25
- [153] Martocchia A., Karas V., Matt G., 2000, MNRAS, 312, 817

-
- [154] Martocchia A., Matt G., 1996, MNRAS, 282, L53
- [155] Martocchia A., Matt G., Karas V., 2002, A&A 383, 23
- [156] Mas-Hesse J. M., Rodríguez-Pascual P. M., Sanz Fernández de Córdoba L., Boller Th., 1994, A&A, 283, L9
- [157] Mason K. O. et al., 2001, A&A, 365, 36
- [158] Matt G., Perola G. C., Piro L., 1991, A&A, 247, 25
- [159] Mathur S., 2000, MNRAS, 314, 17
- [160] Mathur S., Grupe D., 2004, A&A in press (astro-ph/0407512)
- [161] Merloni A., Fabian, A. C., 2001, MNRAS, 321, 549
- [162] Merloni A., Fabian A. C., 2001, MNRAS, 328, 958
- [163] Miller H. R., Ferrara E. C., McFarland J. P., Wilson J. W., Daya A. B., Fried R. E., 2000, NewAR, 44, 539
- [164] Miller K. A., Stone J. M., 2000, ApJ, 534, 398
- [165] Mineshige S., Toshihiro K., Takeuchi M., Hayashida K., 2000, PASJ, 52, 499
- [166] Minezaki T. et al, 2004, ApJ, 600, 35
- [167] Miniutti G., Fabian A. C., 2004, MNRAS, 349, 1435
- [168] Miniutti G., Fabian A. C., Goyder R., Lasenby A. N., 2003, MNRAS, 344, L22
- [169] Miniutti G., Fabian A. C., Miller J. M., 2004, MNRAS, 351, 466
- [170] Misner C. W., Thorne K. S., Wheeler J. A., 1973, Gravitation, Freeman Press
- [171] Mitsuda K. et al., 1984, PASJ, 36, 741
- [172] Miyoshi M., Moran J., Herrnstein J., Greenhill L., Nakai N., Diamond P., Inoue M. 1995, Nature, 373, 127
- [173] Molendi S., Sembay S., 2003, *XMM-Newton* Calibration Presentations (CAL-TN-0036-1-0)
- [174] Murphy E. M., Lockman R. J., Laor A., Elvis M., 1996, ApJS, 105, 369
- [175] Murray N., Chiang J., 1997, ApJ, 474, 91
- [176] Mushotzky R. F., 1984, AdSpR, 3, 157
- [177] Mushotzky R. F., Marshall F. E., Boldt E. A., Holt S. S., Serlemitsos P. J., 1980, ApJ, 235, 377

- [178] Nandra K. et al., 2000, *ApJ*, 544, 734
- [179] Nandra K., George I. M., Mushotzky R. F., Turner T. J., Yaqoob T., 1997, *ApJ*, 477, 602
- [180] Nayakshin S., Kazanas D., Kallman T.R., 2000, *ApJ*, 537, 833
- [181] Netzer H., 1990, in Blandford R., Netzer H., Woltjer L., eds, *Active Galactic Nuclei*, Springer-Verlag
- [182] Netzer H., 1993, *ApJ*, 411, 594
- [183] Netzer H., Shemmer O., Maiolino R., Oliva E., Croom S., Corbett E., di Fabrizio L., 2004, *ApJ*, 614, 558
- [184] Nicastro F., Fiore F., Matt G., 1999, *ApJ*, 517, 108
- [185] Norman C. et al., 2002, *ApJ*, 571, 218
- [186] Novikov I. D., Thorne K. S., 1973, in DeWitt C., DeWitt B., eds, *Black holes*, Gordon & Breach, 343
- [187] Ogle P. M., Mason K. O., Page M. J., Salvi N. J., Cordova F. A., McHardy I. M., Priedhorskyi W. C., 2004, *ApJ*, 606, 151
- [188] Oknyanskij V. L., Lyuty V. M., Taranova O. G., Shenavrin V. I., 1999, *AstL*, 25, 483
- [189] Oknyanskij V. L., Lyuty V. M., Taranova O. G., Shenavrin V. I., 2004 (astro-ph/0410100)
- [190] Oosterbroek T., van der Klis M., Kuulkers E., van Paradijs J., Lewin W. H. G., 1995, *A&A*, 297, 141
- [191] Osterbrock D. E., Pogge R. W., 1985, *ApJ* 297, 166
- [192] Otani C., Kii T., Miya K., 1996, MPE Report 263, 491
- [193] Palmeri P., Mendoza C., Kallman T. R., Bautista M. A., 2002, *ApJ*, 577, 119
- [194] Perola G. C. et al., 2002, *A&A*, 389, 802
- [195] Peterson B. M., 1997, *An Introduction to Active Galactic Nuclei*, Cambridge Univ. Press
- [196] Peterson B. M. et al., 2000, *ApJ*, 542, 161
- [197] Peterson B. M. et al., 2004, *ApJ*, 613, 682
- [198] Peterson B. M., Horne K., 2004, in Livio M., ed, *Planets to Cosmology: Essential Science in Hubble's Final Years*, Cambridge Univ. Press, in press (astro-ph/0407538)

-
- [199] Peterson B. M., Wanders I., Bertram R., Hunley J. F., Pogge R. W., Wagner R. M., 1998, *ApJ*, 501, 82
- [200] Phillips M. M., 1978, *ApJS*, 38, 187
- [201] Piro L., Matt G., Ricci R., 1997, *A&AS*, 126, 525
- [202] Polletta M., Courvoisier T., 1999, *A&A*, 350, 765
- [203] Pollock A. M. T., 2003, *XMM-Newton Calibration Presentations (CAL-TN-0030-2-1)*
- [204] Porquet D., Reeves J. N., O'Brien P., Brinkmann W., 2004, *A&A*, 422, 85
- [205] Porquet D., Reeves J. N., 2003, *A&A*, 408, 119
- [206] Pounds K. A., Done C., Osborne J. P., 1995, *MNRAS*, 277, 5
- [207] Pounds K. A., Nandra K., Stewart G. C., George I. M., Fabian A. C., 1990, *Nature*, 344, 132
- [208] Pounds K. A., Reeves J. N., 2002, ([astro-ph/0201436](https://arxiv.org/abs/astro-ph/0201436))
- [209] Pounds K. A., Reeves J. N., King A. R., Page K. L., 2004, *MNRAS*, 350, 10
- [210] Pounds K., Reeves J., O'Brien P., Page K., Turner M., Nayakshin S., 2001, *ApJ*, 559, 181
- [211] Pozdniakov L. A., Sobol I. M., Sunyaev R. A., 1979, *A&A*, 75, 214
- [212] Press W. H., Teukolsky S. A., Vetterling W. T., Flannery B. P., 1992, *Numerical Recipes*, Cambridge Univ. Press
- [213] Proga D., Stone J. M., Kallman T. R., 2000, *ApJ*, 543, 686
- [214] Puchnarewicz E. M. et al., 1992, *MNRAS*, 256, 589
- [215] Rees M., 1984, *ARA&A*, 22, 471
- [216] Rees M., 1987, *MNRAS*, 228, 47
- [217] Reeves J. N., Turner M. J. L., 2000, *MNRAS*, 316, 234
- [218] Remillard R., Bradt H., Buckley D., Roberts W., Schwartz D., Tuohy I., Wood K., 1986, *ApJ*, 301, 742
- [219] Remillard R., Grossan B., Bradt H. V., Ohashi T., Hayashida K., 1991, *Nature*, 350, 589
- [220] Reynolds C. S., 1996, PhD thesis, Univ. Cambridge

- [221] Reynolds C. S., 1997, MNRAS, 286, 513
- [222] Reynolds C. S., 2000, ApJ, 533, 811
- [223] Reynolds C., Fabian A., 1997, MNRAS, 290, 1
- [224] Reynolds C. S., Nowak M. A., 2003, PhR, 377, 389
- [225] Reynolds C. S., Wilms J., Begelman M. C., Staubert R., Kendziorra E., 2004, MNRAS, 349, 1153
- [226] Reynolds C. S., Young A., Begelman M., Fabian A., 1999, ApJ, 514, 164
- [227] Robinson-Saba J. L., PhD thesis, Univ. Maryland
- [228] Rodríguez-Ardila A., Viegas S. M., Pastoriza M. G., Prato L., 2002, ApJ, 565, 140
- [229] Rodríguez-Pascual P. M., Mas-Hesse J. M., Santos-Lleó M., 1997, A&A, 327, 72
- [230] Ross R. R., Fabian A. C., 1993, MNRAS, 261, 74
- [231] Ross R. R., Fabian A. C., Ballantyne D. R., 2002, MNRAS, 336, 315
- [232] Ross R. R., Fabian A. C., Mineshige S., 1992, MNRAS, 258, 189
- [233] Ross R. R., Fabian A. C., Young A. J., 1999, MNRAS, 306, 461
- [234] Rozanska A., Dumont A.-M., Czerny B., Collin S., 2002, MNRAS, 332, 799
- [235] Rybicki G. B., Lightman A. P., 1979, Radiative Processes in Astrophysics, John Wiley & Sons
- [236] Sako M. et al., 2001, A&A, 365, 168
- [237] Salpeter E. E., 1964, ApJ, 140, 796
- [238] Scharwächter J., Eckart A., Pfalzner S., Moulata J., Straubmeier C., Stagnun J., 2003, A&A, 405, 959
- [239] Schmidt M., Green R. F., 1983, ApJ, 269, 352
- [240] Shakura N. I., Sunyaev R. A., 1973, A&A, 24, 337
- [241] Shapiro S. L., Lightman A. P., Eardley D. M., 1976, ApJ, 204, 187
- [242] Shields G. A., 1978, Nature, 272, 706
- [243] Shuder J. M., Osterbrock D. E., 1981, ApJ, 250, 55
- [244] Siebert J., Leighly K. M., Laurent-Muehleisen, S. A., Brinkmann, W., Boller Th., Matsuoka M., 1999, A&A, 348, 678

-
- [245] Skibo J. G., 1997, *ApJ*, 478, 522
- [246] Socrates A., Davis S. W., Blaes O., 2004, *ApJ*, 601, 405
- [247] Strüder L. et al., 2001, *A&A*, 365, 18
- [248] Szokoly G. P. et al., 2004, *ApJS*, 155, 271
- [249] Sulentic J. W., Zwitter T., Marziani P., Dultzin-Hacyan D., 2000, *ApJ*, 536, 5
- [250] Tanaka Y. et al., 1995, *Nature*, 375, 659
- [251] Tanaka Y., Boller Th., Gallo L., Keil R., Ueda Y., 2004, *PASJ*, 56, 9 (T04)
- [252] Tanaka Y., Shibazaki N., 1996, *ARA&A*, 34, 607
- [253] Tanaka Y., Ueda Y., Boller Th., 2003, *MNRAS*, 338, 1
- [254] Taylor R. D., Uttley P., McHardy I. M., 2003, *MNRAS*, 342, 31
- [255] Tennant A. F., 1988, *MNRAS*, 230, 403
- [256] Thorne K. S., 1974, *ApJ*, 191, 507
- [257] Turner M. J. L. et al., 1990, *MNRAS*, 244, 310
- [258] Turner M. J. L. et al., 2001, *A&A*, 365, 27
- [259] Turner T. J., 1987, *MNRAS*, 226, 9
- [260] Turner T. J. et al., 2002, *ApJ*, 574, L123
- [261] Turner T. J., Kraemer S. B., Reeves J. N., 2004, *ApJ*, 603, 62
- [262] Turner T. J., Nandra K., George I. M., Fabian A. C., Pounds K. A., 1993, *ApJ*, 419, 127
- [263] Turner T. J., Pounds K. A., 1989, *MNRAS*, 240, 833
- [264] Ueda Y., Inoue H., Tanaka Y., Ebisawa K., Nagase F., Kotani T., Gehrels N., 1998, *ApJ*, 500, 1069
- [265] Ulvestad J. S., Antonucci R. R. J., Goodrich R. W., 1995, *AJ*, 109, 81
- [266] Uttley P., Fruscione A., McHardy I., Lamer G., 2003, *ApJ*, 595, 656
- [267] Vaughan S., Boller Th., Fabian A. C., Ballantyne D. R., Brandt W. N., Trümper J., 2002, *MNRAS*, 337, 247
- [268] Vaughan S., Fabian A. C., 2004, *MNRAS*, 348, 1415
- [269] Vaughan S., Edelson R., 2001, *ApJ*, 548, 694

- [270] Vaughan S., Reeves J., Warwick R., Edelson R., 1999, MNRAS, 309, 113
- [271] Veilleux S., Osterbrock D., 1987, ApJS, 63, 295
- [272] Vestergaard M., Wilkes B. J., 2001, ApJS, 134, 1
- [273] Vignali C. et al., 2003, AJ, 125, 2876
- [274] Wall J. V., 1996, QJRAS, 37, 519
- [275] Walter R., Fink H. H., 1993, A&A, 274, 105
- [276] Wampler E. J., Oke J. B., 1967, ApJ, 148, 695
- [277] Wandel A., Peterson B. M., Malkan M. A., 1999, ApJ, 526, 579
- [278] Watarai K., Mizuno T., Mineshige S., 2001, ApJ, 549, 77
- [279] Watson W. D., Wallin B. K., 1994, ApJ, 432, L35
- [280] Webb W., Malkan M., 2000, ApJ, 540, 652
- [281] Weymann R. J., Morris S. L., Foltz C. B., Hewett P. C., 1991, ApJ, 373, 23
- [282] Williams R. J., Pogge R. W., Mathur S., 2002, AJ, 124, 3042
- [283] Wills B. J., Laor A., Brotherton M. S., Wills D., Wilkes B. J., Ferland G. J., Shang Z., 1999, ApJ, 515, 53
- [284] Wilms J., Reynolds C. S., Begelman M. C., Reeves J., Molendi S., Staubert R., Kendziorra E., 2001, MNRAS, 328, L27
- [285] Yaqoob T., George I. M., Kallman T. R., Padmanabhan U., Weaver K. A., Turner T. J., 2003, ApJ, 596, 85
- [286] Yaqoob T., McKernan B., Ptak A., Nandra K., Serlemitsos P. J., 1997, ApJ, 490, 25
- [287] Yaqoob T., Padmanabhan U., Dotani T., Nandra K., 2002, ApJ, 569, 487
- [288] Young A. J., Crawford C. S., Fabian A. C., Brandt W. N., O'Brien P. T., 1999, MNRAS, 304, 46
- [289] Yuan W., Siebert J., Brinkmann W., 1998, A&A, 334, 498
- [290] Zdziarski A. A., Johnson W. N., Done C., Smith D., McNaron-Brown K., 1995, ApJ, 438, 63
- [291] Zdziarski A., Leighly K., Matsuoka M., Cappi M., Mihara T., 2002, ApJ, 573, 505
- [292] Życki P. T., Krolik J. H., Zdziarski A. A., Kallman T. R., 1994, ApJ, 437, 597

CURRICULUM VITAE

Personal data

Name: Luigi C. Gallo
Date of birth: 26 April 1973
Place of birth: Calgary, Canada
Nationality: Canadian
Current address: Max-Planck-Institut für extraterrestrische Physik
Postfach 1312
D-85741, Garching
Germany
E-mail: lgallo@mpe.mpg.de

Education

2001 – 2004 International Max-Planck Research School on Astrophysics at
Max-Planck-Institut für extraterrestrische Physik (Germany)
Ph.D. in Physics
Thesis Project: X-ray Properties of Narrow-line Seyfert 1
Galaxies
Thesis Advisors: Dr. Thomas Boller,
Prof. Dr. Joachim Trümper

1999 – 2001 San Diego State University (USA)
Master of Science in Astronomy
Thesis Title: HET Observations of the NLS1 Akn 564
Thesis Advisor: Dr. William F. Welsh

1993 – 1997 University of Calgary (Canada)
Bachelor of Science in Astrophysics

